Title
An inclusive search for supersymmetry in 13 TeV proton-proton collision data

Author
Bradmiller-Feld, John W.

Publication Date
2017

Peer reviewed|Thesis/dissertation

UNIVERSITY OF CALIFORNIA
Santa Barbara

An inclusive search for supersymmetry in 13 TeV proton-proton collision data

A Dissertation submitted in partial satisfaction
of the requirements for the degree of

Doctor of Philosophy

in

Physics

by

John William Bradmiller-Feld

Committee in Charge:

Professor Jeffrey Richman, Chair

Professor David Stuart

Professor Nathaniel Craig

June 2017

The Dissertation of
John William Bradmiller-Feld is approved:

Professor David Stuart

Professor Nathaniel Craig

Professor Jeffrey Richman, Committee Chairperson

May 2017

An inclusive search for supersymmetry in 13 TeV proton-proton collision data

by

John William Bradmiller-Feld

Dedicated to any Ph.D. student struggling to see the light at the end of the tunnel. If I can make it, so can you.

Acknowledgements

This is actually the last part of this thesis I'll write because it's the hardest for me to start. I think if I took the time to fully thank everyone who made this degree possible, I'd end up with a document as long as my thesis, but I'll give it a try...

I'd be foolish not to acknowledge the work of everyone who contributed countless hours to this analysis or who gave me a chance to contribute myself. This group includes, but is not limited to, Bill Ford, Kevin Stenson, Troy Mulholland, Frank Jensen, Jim Hirschauer, Andrew Whitbeck, and Bibhu Mahakud for the $Z \rightarrow \nu\bar{\nu}$ background estimation; Kenichi Hatakeyama, Ahmad Borzou, Seema Sharma, and Aditee Rane for the τ_h background estimation; Owen Long, Pawandeep Jandir, and Amin Ghiasi (low-$\Delta\phi$ extrapolation), as well as Sam Bein, Marek Niedziela, and Jory Sonnenveld (rebalance-and-smear) for the QCD background estimationl Arne-Rasmus Dräeger and Simon Kurz for the lost lepton background estimation; Rishi Patel and Nhan Tran for leading the integration and interpretation team with me; Manuel Franco Sevilla for trigger development and efficiency measurements; Ana Ovcharova for sacrificing her sleep so we could have Monte Carlo simulations; and, of course, Bill Gary and Keith Ulmer for their exemplary leadership and organization. You have all set an incredibly high standard for how a collaboration should work.

To the entire UCSB High Energy Physics group, but especially my advisor Jeff Richman, deputy advisor David Stuart, postdoctoral muses Manuel Franco Sevilla, Ana Ovcharova, Frank Golf, Indara Suáurez Silva, Chris West, and Jae Hyeok Yoo, and my student brothers-in-arms Adam Dishaw, Ryan Heller, and Rohan Bhandari, thank you for teaching me what it means to be a great scientist. I'll carry the lessons I learned from you everywhere I go.

To Brig Williams and Jamie Saxon at the University of Pennsylvania, thank you for lighting that initial fire in me and for staying invested in my work and wellbeing long after I graduated. To Khilesh Mistry, Bijan Haney, Christian Herwig, and the rest of the Penn students, thank you for making CERN fun.

Coming of age as a physicist and researcher in the early years of the LHC has been one of the greatest privileges of my life. It almost seems unfair, though–thousands of people spent decades building the LHC and its detectors, and I showed up (along with many other students) just when things were getting exciting and got to reap the benefits of their work. Many criminally understated thanks go to them.

And now from the bottom of my heart, to my royal ~~room~~ soul-mates in King Daniel, particularly Shankari Rajagopal, Adam Dishaw (yes, you again), Alex Walter, and Dave Sutherland, thank you for celebrating with me through good times, lifting my spirits during hard times, and sitting by my side on that old couch night after night.

To my honorary parents in Santa Barbara (Zev Nathan & Neal Mazer) and Pays de Gex (Martine Goldschmidt-Clermont & Alain Mélo), thank you for making me feel so close to home while so far away.

And the most important thanks must go to my mothers and sister, for supporting me in every way throughout my education, even when I decided to move far away. I am so glad that I got to see so much of you during this time, despite the distance. For all the joy I've gotten out of California, Philly is still home.

Curriculum Vitæ

John William Bradmiller-Feld

Education

University of California, Santa Barbara June 2017
Ph.D. in Physics
University of California, Santa Barbara April 2015
M.A. in Physics
University of Pennsylvania May 2012
B.A. in Physics

Selected Publications

Search for supersymmetry in multijet events with missing transverse momentum in proton-proton collisions at 13 TeV
Submitted to *Physical Review D* (April 2017)
Authors: CMS Collaboration
Search for supersymmetry in the multijet and missing transverse momentum final state in pp collisions at 13 TeV
Physics Letters B (May 2016)
Authors: CMS Collaboration
Searches for electroweak neutralino and chargino production in channels with Higgs, Z, and W bosons in pp collisions at 8 TeV
Physical Review D (September 2014)
Authors: CMS Collaboration
Search for diphoton events with large missing transverse momentum in 7 TeV proton–proton collision data with the ATLAS detector
Physics Letters B (December 2012)
Authors: ATLAS Collaboration

Abstract

An inclusive search for supersymmetry in 13 TeV proton-proton collision data

John William Bradmiller-Feld

The second run of *pp* collisions at the Large Hadron Collider (LHC) at CERN marks one of the most anticipated eras in the field of particle physics. Already the largest and most powerful science experiment of its kind, the LHC has outdone itself, running at a record center of mass energy of $\sqrt{s} = 13$ TeV and colliding protons at rates of over 600 million collisions per second. The incredible performance of the machine allows for unprecedented exploration of the TeV scale. No elementary particles have ever been observed at these energies, yet many are hypothesized as extensions to the standard model (SM), the most complete and widely accepted model of elementary particles and their interactions. Among the most sought-after hypothetical particles are those proposed by the theory of supersymmetry (SUSY).

In this thesis, results are presented from a generic search for strongly produced supersymmetric particles in *pp* collisions in the multijet + missing transverse momentum final state. The largest analyzed data sample corresponds to 35.9 fb^{-1} recorded by the CMS experiment at $\sqrt{s} = 13$ TeV in 2016. This search is motivated by SUSY models that avoid fine-tuning of the Higgs mass. In such models, strongly produced SUSY particles, including the gluino and top squark, are predicted to have masses on the order of a TeV. These particles also have some of the highest production cross sections in SUSY and give rise to final states with distinct, high jet multiplicity event signatures. To make the analysis sensitive to a wide range of such final states, events are classified by the number of jets, the scalar sum of the transverse momenta of the jets, the vector sum of the transverse momenta of the jets, and the number of b-tagged jets.

All SM backgrounds are measured using dedicated control samples in data. No significant excess is observed beyond the measured SM expectation. The results are interpreted as limits on simplified SUSY models. In these models, gluinos with masses as high as 1970 GeV and squarks with masses as high as 1450 GeV are excluded at 95% CL for scenarios with low $\tilde{\chi}_1^0$ mass, far exceeding the limits set in Run I.

Contents

List of Figures

Chapter 1

Introduction

The first run of the Large Hadron Collider (LHC) at CERN provided no shortage of excitement. The field of particle physics captured the world's attention on multiple occasions. The collider itself was a marvel, decades in the making and requiring record-breaking technological advances (and a bit of patience) before its first successful collisions in 2010. Many particle physicists and particle physics enthusiasts would cite the Nobel Prize-winning discovery of the higgs boson in 2012 as the highlight of this first run, and rightfully so. The experimental collaborations at the LHC accomplished what no other experiments could do, discovering the missing piece of the standard model.

I was fortunate enough to enter the world of particle searches around this time and witnessed the final steps of this discovery, specifically the analysis of 7 and 8

TeV data. While I have no intention of trivializing the analyses that made this discovery [1, 2], I cannot help but marvel at their simplicity. If you neglect all the work you have to do to design the experiments and develop the computing and statistical tools needed to carry out such an analysis (author's note: do not neglect these), it sounds like fun. You have to reconstruct some of the most familiar standard model particles, e.g., photons, electrons, or muons, add their four-momenta together, and *voila* (I had to include at least one French word in this thesis), you have a discovery! You do not need a Ph.D., or even a decent pair of glasses to see that something interesting is going on in the top two plots of Figure 1.1. Just look at those bumps!

The plot below, however, is another story. Where are the bumps? Why do the histograms have so many bins? Why are there so many (beautiful) colors? I think this plot is somewhat emblematic of the challenges facing particle hunters in the post-higgs era. While the previous generation of students may have asked, "when do you think we will see the higgs?" at the start of their Ph.D.s, I found myself asking, "what are we even looking for?" Not that I am complaining–these challenges have made for a great research experience.

My goal for this thesis is to convince you of the necessity for an analysis complicated enough to produce that plot. In Chapter 2, I will begin by summarizing the state of the standard model at the end of LHC Run I and motivating an "in-

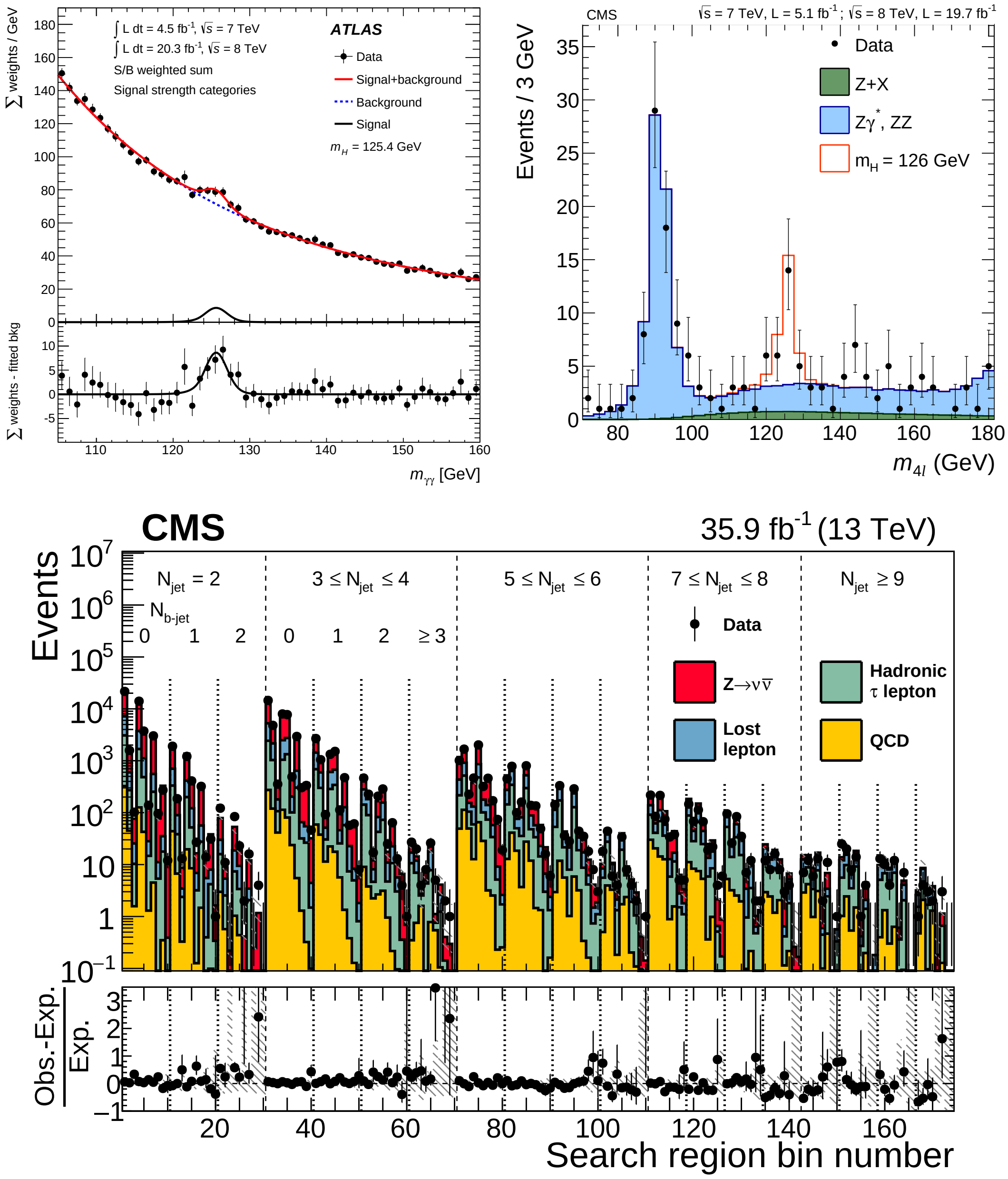

Figure 1.1: Top-left: distribution of the di-photon reconstructed mass from ATLAS's search for the higgs boson in the $h \to \gamma\gamma$ decay channel [3]. Top-right: distribution of the four-lepton reconstructed mass from CMS's search for the higgs boson in the $h \to ZZ^* \to 4\ell$ decay channel [4]. Bottom: this plot, from Ref. [5], is left as an exercise for the reader.

clusive" and "generic" search for supersymmetry (SUSY). In Chapters 3–5, I will highlight some of the key features of the experimental apparati needed to perform such a search, as well as the techniques used to reconstruct particles in these experiments. Chapters 6–8 are dedicated to a specific analysis of LHC data, the "Search for supersymmetry in multijet events with missing transverse momentum in proton-proton collisions at 13 TeV" (arXiv:1704.07781 [hep-ex]). Finally, in Chapters 9–10, I will summarize the results of the analysis and propose a few new directions the next generation of particle-hunting students.

Chapters 2–5 are meant to set the stage for the analysis; they do not provide comprehensive introductions to their respective topics but highlight the most important concepts most relevant to Chapters 8–10.

Part 1

Theory, context, and motivation

Chapter 2

Theoretical background and experimental context

2.1 Standard model of particle physics

The standard model (SM) of particle physics is one of the greatest achievements of modern science. It describes seventeen fundamental particles (not counting antiparticles) that interact under the strong, weak, and electromagnetic forces. These particles, shown in Figure 2.1 include twelve fermions, i.e., six quarks, three charged leptons, and three neutrinos, as well as four gauge bosons and a scalar higgs boson. The existence of all seventeen has been confirmed by experiments. Several other physical quantities predicted by the SM, including the electron's magnetic moment, have been measured and shown to agree with their theoretical values to very high precision [6]. The SM appears to be valid at all energy scales thoroughly probed by experiments prior to the Large Hadron Collider (LHC) [7, 8, 9, 10].

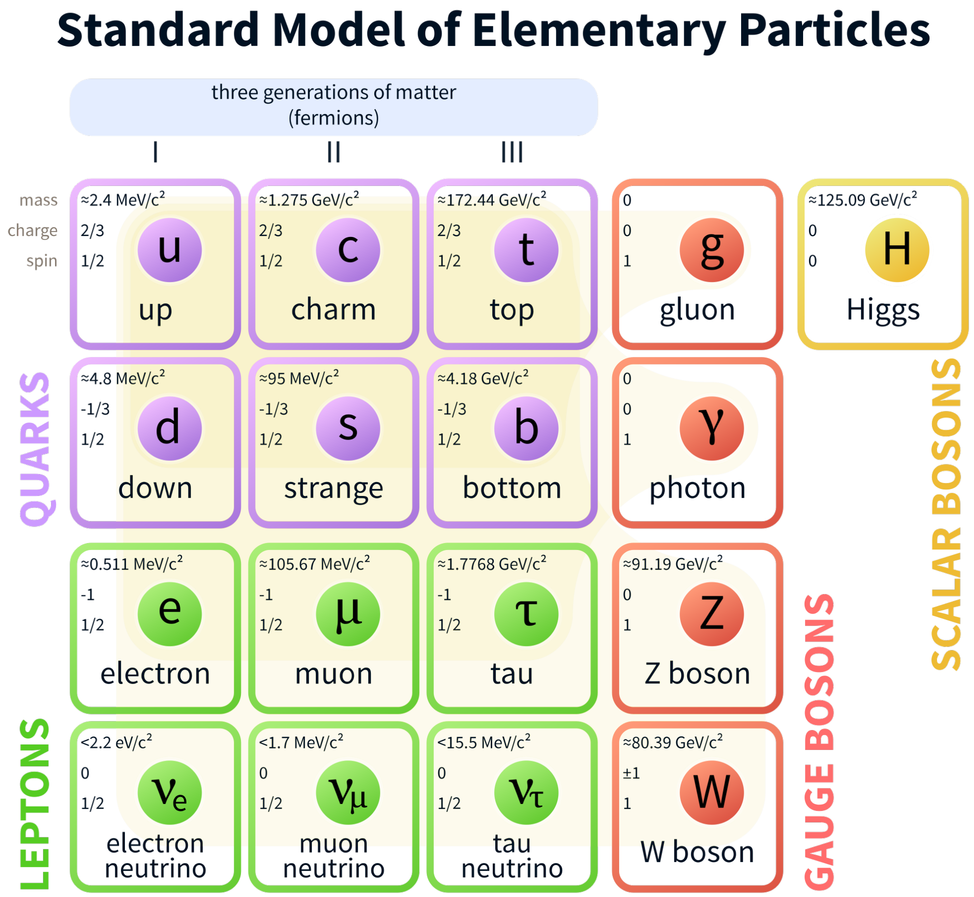

Figure 2.1: The standard model of elementary particle physics, from Ref. [11].

2.1.1 Tension with astrophysical data and neutrino mass measurements

A number of experimental measurements have cast the SM as an incomplete theory of the universe. The SM provides no explanation for:

- the existence of **dark matter**, which comprises 26.8% of all mass-energy in the universe [12], which is suggested by cosmological surveys [13];
- the values of the non-zero **neutrino masses**, suggested by neutrino oscillation measurements [14];
- or **matter-antimatter asymmetry** [15, 16];

nor does it offer a full theory of quantum gravity.

2.1.2 Hierarchy problem

In the SM, the higgs mechanism is responsible for the spontaneous breaking of the $SU(2)_L \otimes U(1)_Y$ gauge symmetry associated with electroweak interactions. This spontaneous symmetry breaking (SSB) is responsible for the separation of the electromagnetic and weak forces, i.e., for a massless photon (γ) mediating electromagnetic interactions with long range $1/r$ potential and the massive $W^\pm$ and Z bosons mediating weak interactions with a short range Yukawa potential.

The higgs potential that induces this SSB must be $SU(2) \times U(1)$ invariant but must have a ground state that transforms non-trivially under $SU(2) \times U(1)$. The simplest form of such a potential is

$$V(\phi) = -\mu^2|\phi^\dagger\phi| + \lambda|\phi^\dagger\phi|^2, \tag{2.1}$$

where ϕ is a complex scalar field and μ and λ are positive constants. A possible ground state is

$$<\phi>= \frac{1}{\sqrt{2}} \begin{pmatrix} 0 \\ v \end{pmatrix} , \tag{2.2}$$

where

$$v = \frac{\mu}{\sqrt{\lambda}} = \frac{2m_W}{g} = 246 \text{ GeV} \tag{2.3}$$

is known as the higgs vacuum expectation value (vev) The vev directly dictates the mass scale of the weak interaction. The question of why this scale is so far in energy from the next known scale, i.e. that of quantum gravity ($\sim 10^{19}$ GeV), is called the hierarchy problem [17, 18].

2.1.3 Fine-tuning and the naturalness problem

In the context of the SM Lagrangian, the vev gives rise to the higgs mass,

$$m_h = \sqrt{2}\mu , \tag{2.4}$$

which must be determined experimentally.

With the discovery of the higgs boson in 2012 by the ATLAS and CMS collaborations, this elusive parameter of the SM was finally measured [19]:

$$m_h = 125.09 \pm 0.21\ (\text{stat.}) \pm 0.11\ (\text{syst.})\ \text{GeV} \tag{2.5}$$

Scalar field theory dictates that we can express this physical (measurable) higgs mass, as the sum of a bare mass parameter $m_{h,0}$ and radiative corrections δm_h^2:

$$m_h^2 = m_{h,0}^2 + \delta m_h^2 \tag{2.6}$$

The radiative correction term δm_h^2 stems from the fact that in the SM, the higgs boson can couple to any particle with mass, including fermions, massive vector bosons, and itself, producing Feynman diagrams of one-loop or higher order. For any fermion, the leading one-loop diagram, shown in Figure 2.2, leads to a mass correction of the form

$$\delta m_h^2|_f = -N_f \frac{\lambda_f^2}{8\pi^2}\left[\Lambda^2 - 6m_f^2 \ln\left(\frac{\Lambda}{m_f}\right) + 2m_f^2\right] + \mathcal{O}\left(\frac{1}{\Lambda}\right)\ , \tag{2.7}$$

where N_f is the fermion's symmetry factor (equal to 1 for leptons, 3 for quarks), m_f is the fermion's mass, λ_f^2 is the fermion's Yukawa coupling. The largest correction comes from the higgs boson's Yukawa coupling to the top quark, the most massive particle in the SM. This diagram is shown along with the bare mass diagram in Figure 2.2. Each Λ factor stems from the fact that the path integral associated with the fermion loop diverges at high energies. Such a divergence is handled by introducing a cutoff energy scale, Λ, which represents the maximum energy up to which the SM is valid. In the absence of other new physics, Λ can be as large as the Planck scale, around 10^{19} GeV, where it is presumed there are novel effects due to quantum gravity [20].

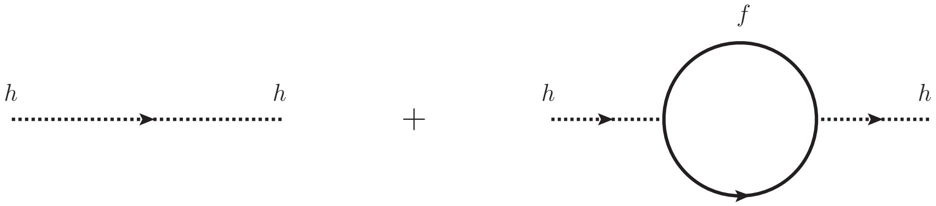

Figure 2.2: Leading Feynman diagrams for the calculation of the SM higgs mass. The diagram on the left corresponds to the term $m_{h,0}$, while the diagram on the right corresponds to all terms in Equation 2.7.

While it is entirely possible that Λ take on such a large value, it seems unlikely given the recently measured higgs mass. If we consider the leading (quadratic) term in Equation 2.7, and focus only on the contribution from the top quark, which has the largest Yukawa coupling, then we have

$$\begin{aligned} m_h^2 &= m_{h,0}^2 - \frac{3\lambda_t^2}{8\pi^2}\Lambda^2 + \cdots \\ (125\ \mathrm{GeV})^2 &= m_{h,0}^2 - \frac{3\lambda_t^2}{8\pi^2}(10^{19}\ \mathrm{GeV})^2 + \cdots \end{aligned} \tag{2.8}$$

To keep the higgs mass at the electroweak scale, the free parameter $m_{h,0}$ must cancel the quadratic term at over 30 decimal places. Such a finely-tuned cancellation is widely considered unnatural [21, 22, 23, 24].

2.2 Supersymmetry

2.2.1 Natural SUSY

Arguably, the simplest way to protect the higgs from being pulled up to the Planck scale is to introduce a new group of scalars with the same Yukawa coupling constants as the SM fermions but whose loop diagrams carry the opposite sign. Such a set of scalars is proposed in models of supersymmetry (SUSY). In these models, there exists an additional scalar degree of freedom for every fermionic degree of freedom in the SM and vice-versa.

In this thesis, we focus on variations of the canonical SUSY model, the Minimal Supersymmetric Standard Model (MSSM). In the MSSM, every fermionic field in the SM has a bosonic superpartner, called a sfermion, and every SM gauge bosonic field has a fermionic superpartner, called a gaugino. The higgs sector comprises two scalar doublets. The SUSY particles are illustrated, along with their SM counterparts, in Figure 2.3.

Since the top quark provides the largest quadratic divergence in the SM, we focus on the scalar partner to the top quark, the stop. It has the same Yukawa coupling λ_t as the top quark but is a spin-0 boson and therefore provides an opposite-sign counterterm to the top's correction to the MSSM higgs mass:

$$\delta m_{h_u}^2 = \frac{3\lambda_t^2}{4\pi^2}(m_t^2 - m_{\tilde{t}}^2)\ln\left(\frac{\Lambda}{m_{\tilde{t}}}\right) + \cdots \tag{2.9}$$

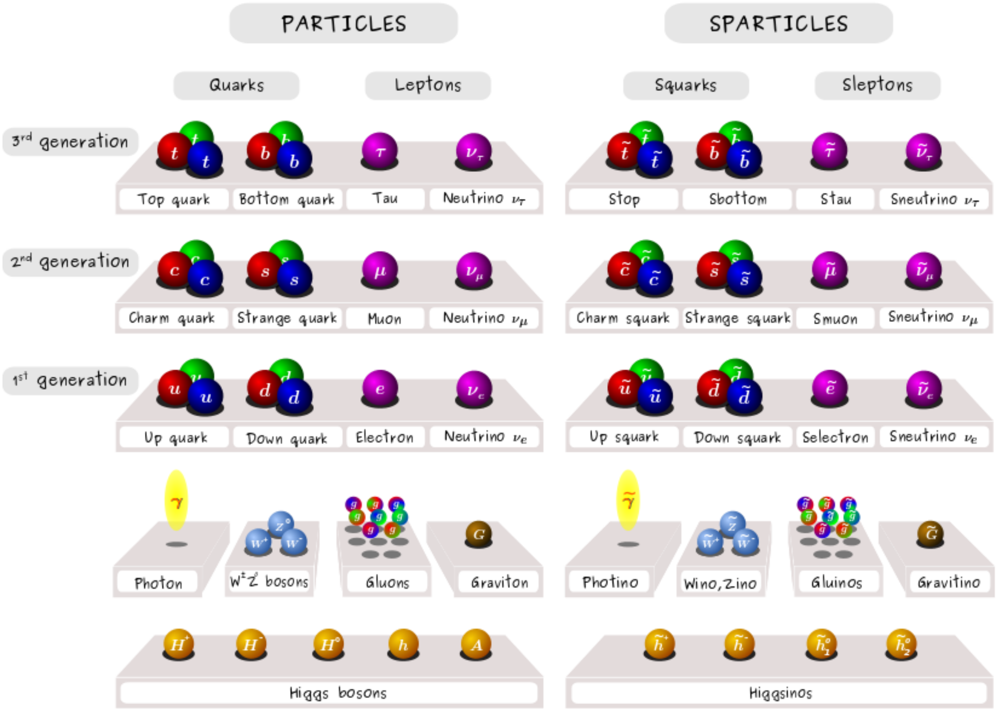

Figure 2.3: Left: the elementary particles of the SM. Right: their SUSY counterparts. Note that there is not always a one-to-one mapping between the mass eigenstates of a SM particle and its superpartner. For example, the superpartners of the W and Z bosons, called gauginos, mix with the higgsinos to form mass eigenstates called charginos and neutralinos. Note that the bino ($\tilde{B}$), the superpartner to the weak hypercharge gauge field in the SM, is a linear combination of the photino and zino. Image credit: Claire David [25].

The quadratically-diverging term from the top is canceled by the contribution from the new scalar, called the top squark or "stop," as shown in Figure 2.4.

Note that we have substituted h_u for h in the mass calculation. Though the details are slightly beyond the scope of this thesis, this notation reflects the fact that in the MSSM, the higgs field is a linear combination of two complex scalar fields, h_u and h_d. For large $\tan\beta$, $h \sim h_u$ and the physical mass of the higgs doublet is given by $m_h^2 = m_{h_u}^2 + |\mu|^2$.

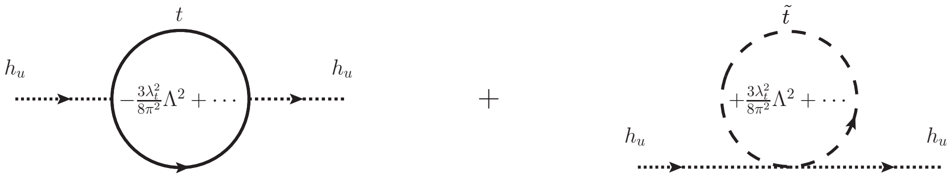

Figure 2.4: Leading Feynman diagrams for radiative corrections to the higgs mass from the top quark (left) and stop (right) in the MSSM. The quadratically-diverging terms that cancel in the MSSM higgs mass calculation are written in the centers of the loops.

In Equation 2.9, we are left with a logarithmic divergence, the severity of which is controlled by the squared mass separation between the top and stop. This mass separation, or sometimes just the mass of the stop, partially defines the degree to which the higgs mass is finely-tuned in the MSSM. Scenarios with minimal fine-tuning are considered natural, though there is no rigorous definition of acceptable fine-tuning. One heuristic is to compare the order of magnitude of the higgs mass squared with a SUSY particle's contribution to that value. If we consider the stop's contribution to the higgs mass squared,

$$\delta m_{h_u}^2|_{\tilde{t}} = -\frac{3\lambda_t^2}{4\pi^2} m_{\tilde{t}}^2 \ln\left(\frac{\Lambda}{m_{\tilde{t}}}\right) + \cdots \tag{2.10}$$

for a UV cutoff of $\Lambda \sim 10$ TeV, which is a somewhat common convention, then to have corrections on the order of the higgs mass squared ($\delta m_{h_u}^2 / m_{h_u}^2 \sim 1$), then we should have $m_{\tilde{t}} \lesssim 400$ GeV. Many popular SUSY models with stops in that mass range were excluded in the first run of the LHC, however, so we might now consider a looser standard of naturalness, in which $\delta m_{h_u}^2/m_{h_u}^2 \sim 10$ and

$$\frac{\delta m_{h_u}^2|_{\tilde{t}}}{m_{h_u}^2} \lesssim 10$$
$$m_{\tilde{t}} \lesssim 1 \text{ TeV} . \tag{2.11}$$

The stop, a scalar, is also subject to its own loop corrections, as shown in Figure 2.5). The gluino diagram (top-left) contributes a mass correction of

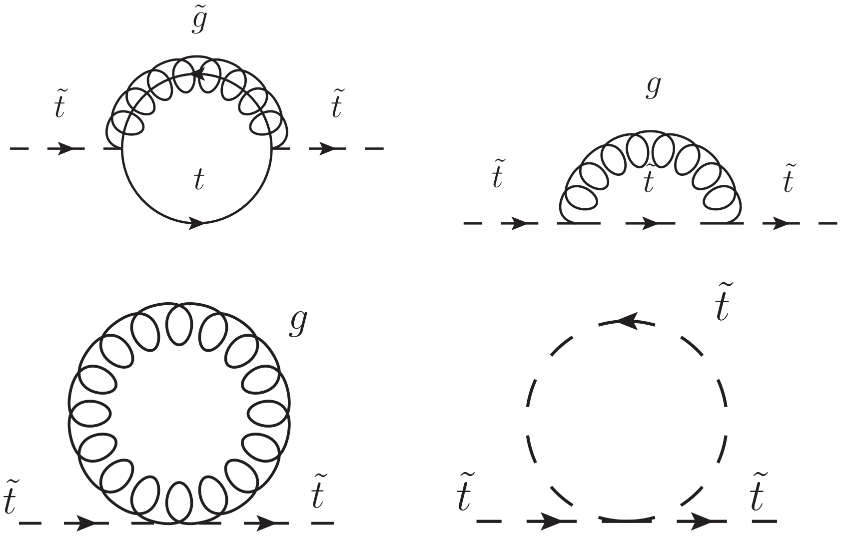

Figure 2.5: Leading Feynman diagrams for radiative corrections to the stop mass in the MSSM, from Ref. [21].

$$\delta m_{\tilde{t}}^2|_{\tilde{g}} = \frac{2g_s^2}{3\pi^2} m_{\tilde{g}}^2 \ln \frac{\Lambda}{m_{\tilde{g}}} + \cdots \ , \tag{2.12}$$

where g_s is a gauge coupling constant.

One can make an analogous argument for a relatively light gluino based on the logic of Equations 2.9–2.11:

$$\begin{aligned} \frac{\delta m_{\tilde{t}}^2|_{\tilde{g}}}{m_{\tilde{t}}^2} &\lesssim 1 \\ m_{\tilde{g}} &\lesssim 2m_{\tilde{t}} \\ m_{\tilde{g}} &\lesssim 2 \text{ TeV} . \end{aligned} \tag{2.13}$$

Arguably, the most universal condition for naturalness is SUSY models is a set of light higgsinos. The higgsino masses are tied to the electroweak scale by the tree-level relation

$$\begin{aligned} m_Z^2 &= -2(m_{h_u}^2 + |\mu|^2) \cdots \\ \mu &\lesssim 200 \text{ GeV}, \end{aligned} \tag{2.14}$$

where μ is now a parameter controlling the higgsino masses. Other particles whose masses often appear in the TeV range in natural SUSY models include the winos, which, like the stop, are tied to the higgs mass at one-loop order, and the left-handed sbottom (bottom squark), which transforms in the same $SU(2)$ multiplet as the left-handed stop.

A summary of the mass ranges in which one might expect to see these particles in a natural SUSY theory is presented in Figure 2.6. It is important to emphasize that this is not the only natural scenario. Many natural models do not require all of these particles to fall in the suggested mass range. The mass ranges are only intended as a set of benchmarks for analyses early LHC Run II data [18, 26, 27].

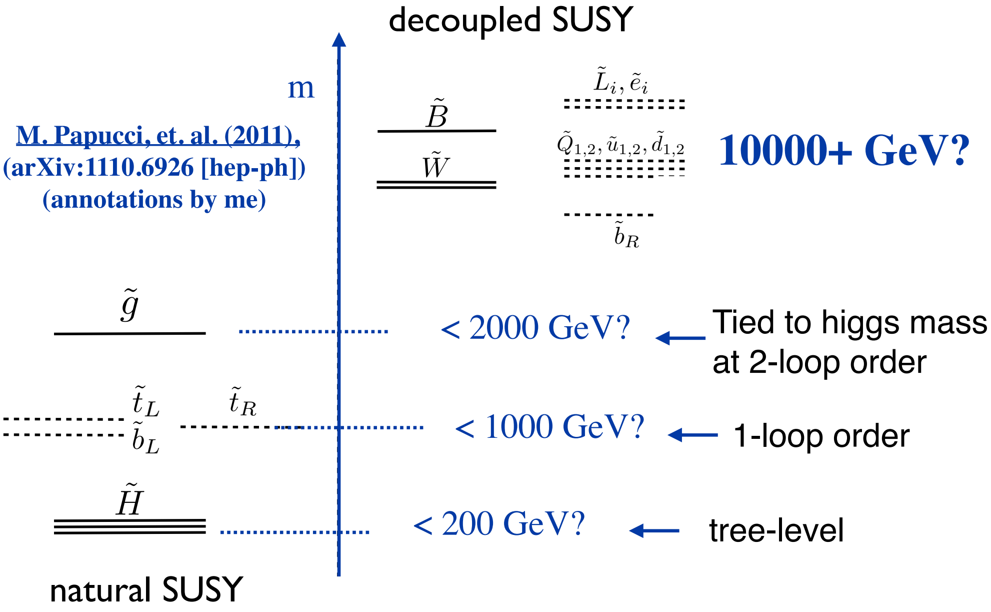

Figure 2.6: An example natural SUSY spectrum, originally from Ref. [22], annotated with possible natural mass ranges for several particles.

The appeal of SUSY extends far beyond the naturalness and hierarchy problems. Part of the reason why SUSY, as a class of models for beyond the standard model (BSM) physics, have been favored for decades is that they are general and flexible enough to answer nearly every big question in modern physics. As suggested by Figure 2.7, SUSY is not the only promising scenario and search target at the LHC, but it is probably as well-motivated as any.

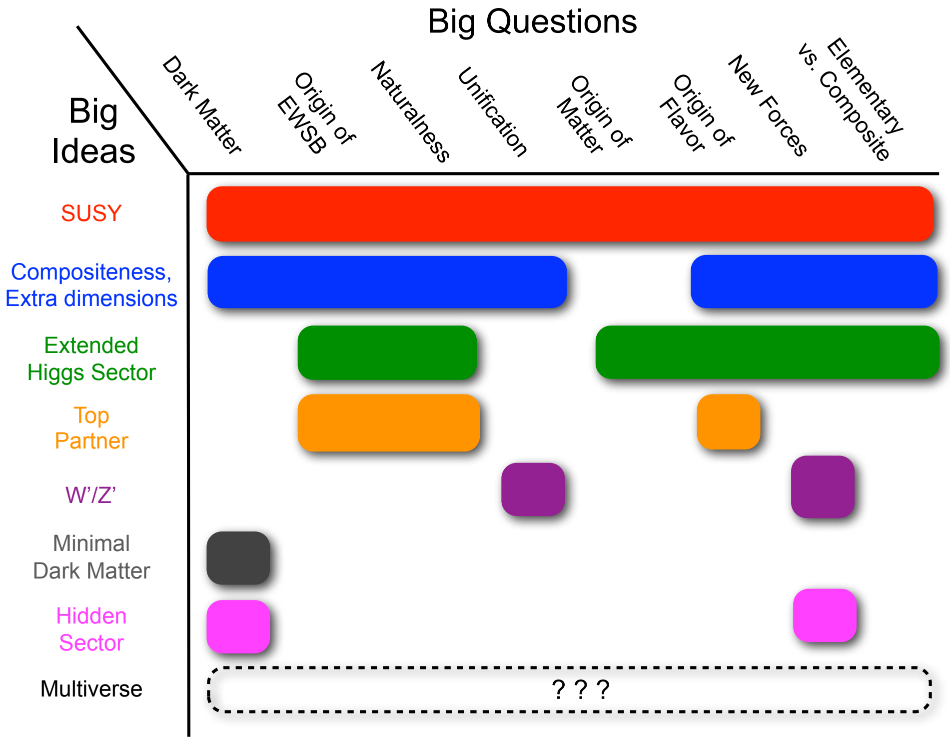

Figure 2.7: Overview of the big questions in theoretical physics that could be answered by SUSY or other popular models of new physics, from Ref. [28].

2.2.2 SUSY phenomenology and experimental signatures

There are no shortage of natural SUSY models nor relevant experimental signatures. These models vary in the production processes, as well as in the exact number and type of final state particles. The models considered in this thesis, however, share a few characteristics. In all of these models, SUSY particles are produced through the strong interaction. These particles undergo a series of R-parity conserving decays. R-parity is a discrete Z_2 symmetry imposed on many SUSY models to enforce baryon and lepton number conservation. R-parity is a new quantum number defined as

$$P_R = (-1)^{3(B-L)+2s}, \tag{2.15}$$

where B is baryon number, L is lepton number, and s is spin. All SUSY particles have $P_R = -1$, while all SM particles have $P_R = +1$ [29]. The most important consequences of R-parity conservation are:

- SUSY particles must be produced in pairs;
- each decay must conserve R-parity, meaning each SUSY particle should decay to one SM and one other SUSY particle;
- and the final states must include at least two stable lightest supersymmetric particles (LSPs). The LSPs are typically taken to be weakly-interacting neutralinos and/or charginos, which are mass eigenstates of the gauginos and higgsinos discussed in Section 2.2.1. If the LSP is a neutralino, then it is coincidentally a dark matter candidate [30].

To understand the experimental signature characteristic of such a model, consider a canonical example of a natural SUSY model, namely the pair production of gluinos that decay via off-shell sbottoms to a final state involving four b quarks and two LSPs:

$$\begin{aligned} pp \to& \tilde{g}\tilde{g}, \\ \tilde{g} \to& \tilde{b}\bar{b}, \\ \tilde{b} \to& b\tilde{\chi}_1^0 \end{aligned} \tag{2.16}$$

A simplified Feynman diagram for this model is provided in Figure 2.8. To give an idea of how such a process may be detected at the LHC, an event display for a real event recorded by the CMS experiment in 2016 is provided in Figure 2.8.

Neither the quarks nor the LSPs can be detected directly, but we can infer their presence through reconstruction techniques. The strong interaction prevents quarks from existing in isolation, so they rapidly combine with other quarks and anti-quarks from the vacuum to form hadrons. We look for collimated sprays of these hadrons, called jets, in the detector to estimate the trajectories of quarks. Four jets, all of which show some characteristics of originating from b quarks, are represented by faint green cones in the event display.

The two neutralino LSPs only interact weakly, so they cannot be detected at all. Nevertheless, we can sum the momentum vectors of all visible particles and infer the momentum sum of the LSPs from any apparent non-conservation of momentum. The kinematic variable representing this momentum sum is called missing transverse momentum, or H_T^{miss}, and is represented in the event display by the purple arrow.

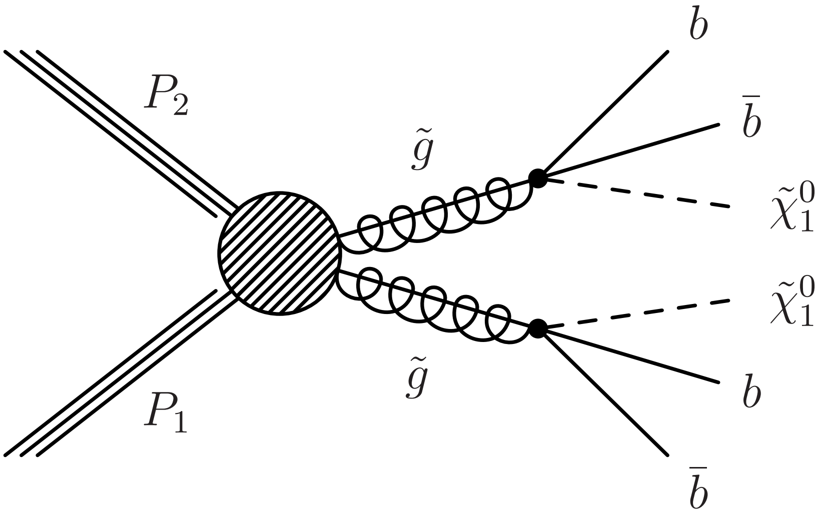

Figure 2.8: Simplified Feynman diagram for the gluino production scenario $pp \to \tilde{g}\tilde{g},\ \tilde{g} \to b\bar{b}\tilde{\chi}_1^0$ (T1bbbb).

Many more details about the specific models considered, as well as the reconstruction and search techniques used in this analysis are provided in the following chapters.

2.2.3 Limits on SUSY production from previous analyses

It is nearly impossible to quote simple precise figures for SUSY processes and particles ruled out by previous analyses, since the MSSM contains a whopping 120 parameters. Any practical SUSY model has to make assumptions about some of

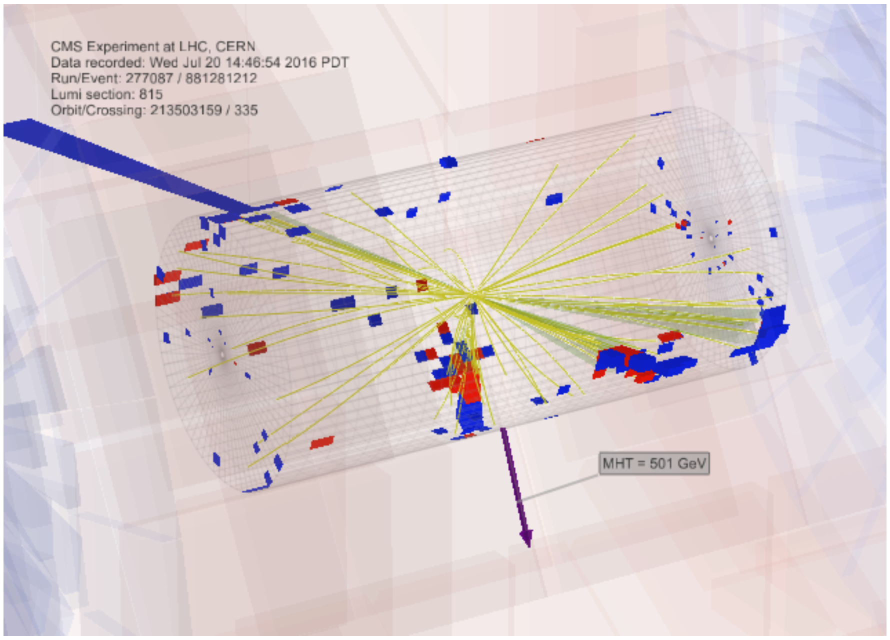

Figure 2.9: Event display for a SUSY candidate event in the analysis search region with exactly 4 jets, all of which are b-tagged. This event, 277087:815:881281212, was recorded by the CMS experiment in 2016. The jets are represented by the faint green cones, while the missing momentum is represented by the purple arrow.

these parameters, and these assumptions affect the conclusions one can take away from experimental results. With that said, we can summarize the most optimistic (if your goal is to exclude) limits set by the ATLAS and CMS experiments in LHC Run I. Simplified scenarios of gluino, stop, and sbottom production were excluded at theoretical reference cross sections at a 95% confidence level at masses as high as $m_{\tilde{g}} = 1375$ GeV, $m_{\tilde{t}} = 755$ GeV, and $m_{\tilde{b}} = 700$ GeV [31, 32, 33] in models with light LSPs. The specific models used to set these limits are described in Section 6.2.2.

Part 2

Experimental Apparatus & Particle Reconstruction

Chapter 3

Large Hadron Collider

Around 100 m underneath the region surrounding the French-Swiss border lies the 26.7 km-long LHC, the largest and most powerful superconducting accelerator ever built. It is designed to collide beams of protons at a center of mass energy of up to $\sqrt{s} = 14$ TeV and a luminosity of 10^{34} cm^{-2}s^{-1}, which corresponds to a rate of over 600 million *pp* collisions per second. As of 2016, the LHC has collided protons at $\sqrt{s} = 13$ TeV and exceeded its design luminosity.

The CERN accelerator complex is shown in Figure 3.1. En route to the LHC rings, protons are passed through a series of smaller accelerators. In order, these are Linac 2, the Proton Synchrotron Booster (PSB), the Proton Synchrotron (PS), and the Super Proton Synchrotron (SPS), which accelerate the protons to 50 MeV, 1.4 GeV, 25 GeV, and 450 GeV, respectively. During the PS stage, the protons

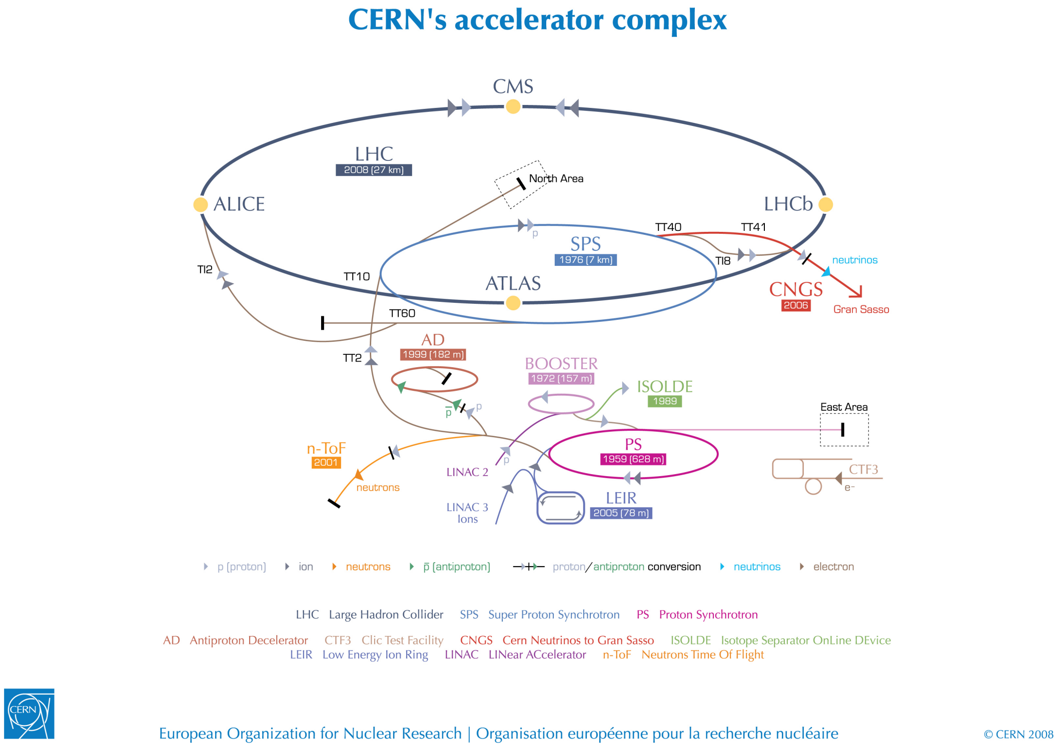

Figure 3.1: Sketch of the CERN accelerator complex, from Ref. [34].

are split into groups of $\mathcal{O}(10^{11})$. These groups, called bunches, are separated in time by intervals of 25 ns. Following acceleration by the SPS, the proton bunches are separated into two 6.5 TeV beams and injected into the LHC rings in opposite directions [35, 36, 37].

The purpose of the LHC is to collide protons at energies high enough to produce particles at previously unprobed mass scales. The upgrade of the collision energy from 8 TeV in Run I to 13 TeV in Run II benefits most searches for new physics, but has the most significant effect on those targeting particles in the TeV range. This effect is perhaps most easily explained by considering the luminosity of parton-parton collisions,

$$\frac{\tau}{\hat{s}}\frac{d\mathcal{L}_{ij}}{d\tau} = \int_{\tau}^{1} dx[f_i^{(a)}(x)f_j^{(b)}(\tau/x) + f_j^{(a)}f_i(b)(\tau/x)]/x \quad [38], \tag{3.17}$$

where the $f_i^{(a)}(x)$ is the number distribution for a parton a of type $i = g, q, \bar{q}$ carrying a fraction x of the proton momentum, $\tau = \hat{s}/s$, and $\hat{s}$ is the center of mass energy of the two colliding partons. This parton luminosity, which has the same dimensions as a cross section, is effectively a measure of the reach of a collider. The key takeaway from the above expression is that parton luminosity falls rapidly with $\sqrt{\hat{s}}$, which reflects the behavior of the proton's parton distribution functions as a function of x. The most interesting quantity is actually the ratio of parton luminosities between colliders of different $\sqrt{s}$, presented in Figure 3.2. The luminosity ratio approximates the amount of data one would have to collect with an 8 TeV collider to obtain the same number of signal events with characteristic mass scale M_X at a 13 TeV collider. This ratio increases exponentially with M_X, meaning that analyses targeting higher mass particles will see the biggest boost in reach with the collider upgrade. As an example, consider a pair of gluinos near the most stringent mass limits set during Run I, $m_{\tilde{g}} \sim 1300$ GeV. For $M_X = 2m_{\tilde{g}} \sim 2600$, we expect a luminosity ratio around 30 for gg scattering processes. In other words, we only need to collect around 1/30 of the data we collected in Run I to achieve the same sensitivity to this process in Run II. Such a significant increase in sensitivity adds extra urgency to our desire to probe natural SUSY in the TeV range.

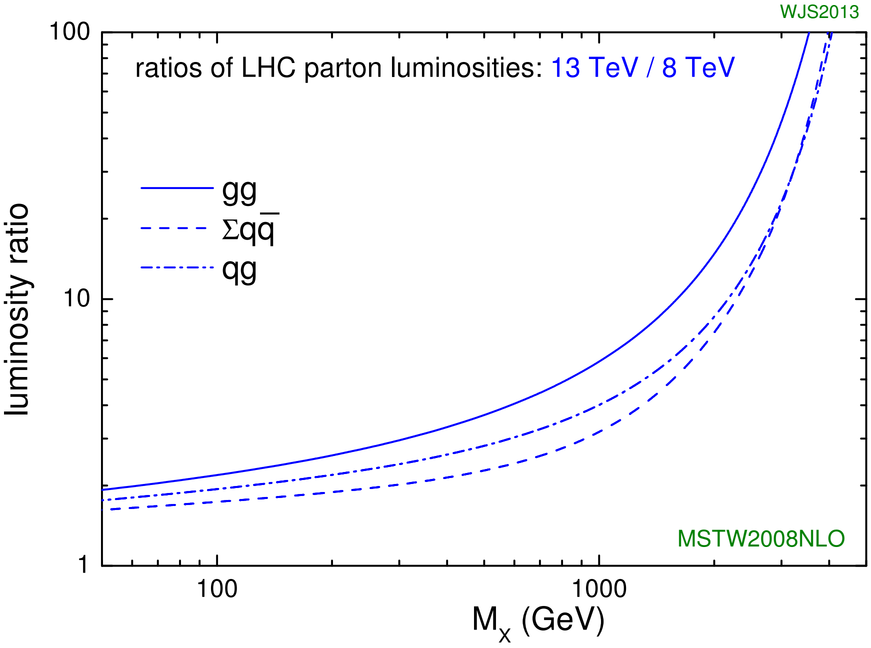

Figure 3.2: From Ref. [39], ratios of parton luminosities at $\sqrt{s} = 13$ TeV to $\sqrt{s} = 8$ TeV as a function of the mass(es) of target particle(s) for various parton-parton scattering processes. The luminosity distributions are calculated using MSTW2008 (NLO) parton distributions, see Ref. [40].

Chapter 4

Compact Muon Solenoid

I would like to be able to name a subsystem of the Compact Muon Solenoid (CMS) detector that plays the biggest role in this analysis, but such a statement would oversimplify. Due to the nature of the analysis, we depend on good performance from the entire detector. As mentioned in Section 2.2.2, the target final states contain missing momentum, which is computed by summing the momenta of all particles in the detector. Such a task requires a hermetic detector design that can detect as much activity stemming from an interaction as possible. The detector must also be comprised of various sub-detectors, each optimized to identify and provide momentum measurements for a particular class of particles. Such is the design of CMS, a superconducting solenoid that provides a uniform axial magnetic field of 3.8 T. From the center out, its sub-detectors are a silicon tracker, an electromagnetic calorimeter, a hadronic calorimeter, and four muon stations interspersed with an iron return yoke. A sectional view of CMS is provided in Figure 4.1 and a slice view showing typical trajectories of different particles is provided in Figure 4.2.

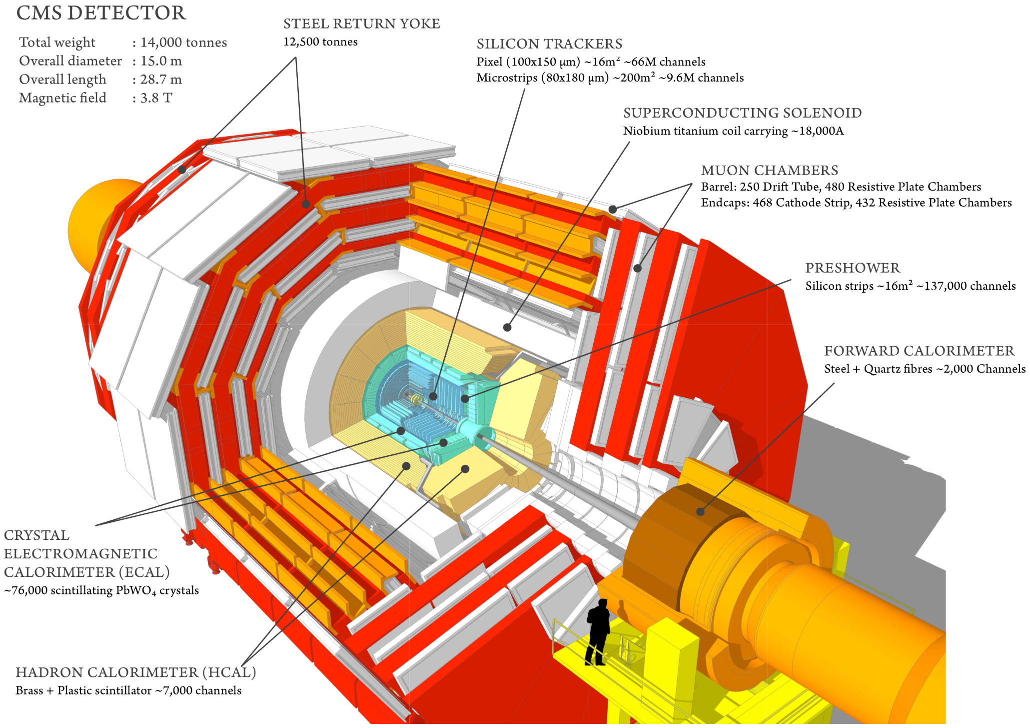

Figure 4.1: Sectional view of the CMS detector, from Ref. [41].

CMS employs a cylindrical coordinate system with an origin placed at the primary interaction point. The z-axis points along the direction of LHC Beam 2, the x-axis points towards the center of the LHC ring, and the y-axis points upward. The xy-plane runs transverse to the beam. We often refer to a particle's transverse

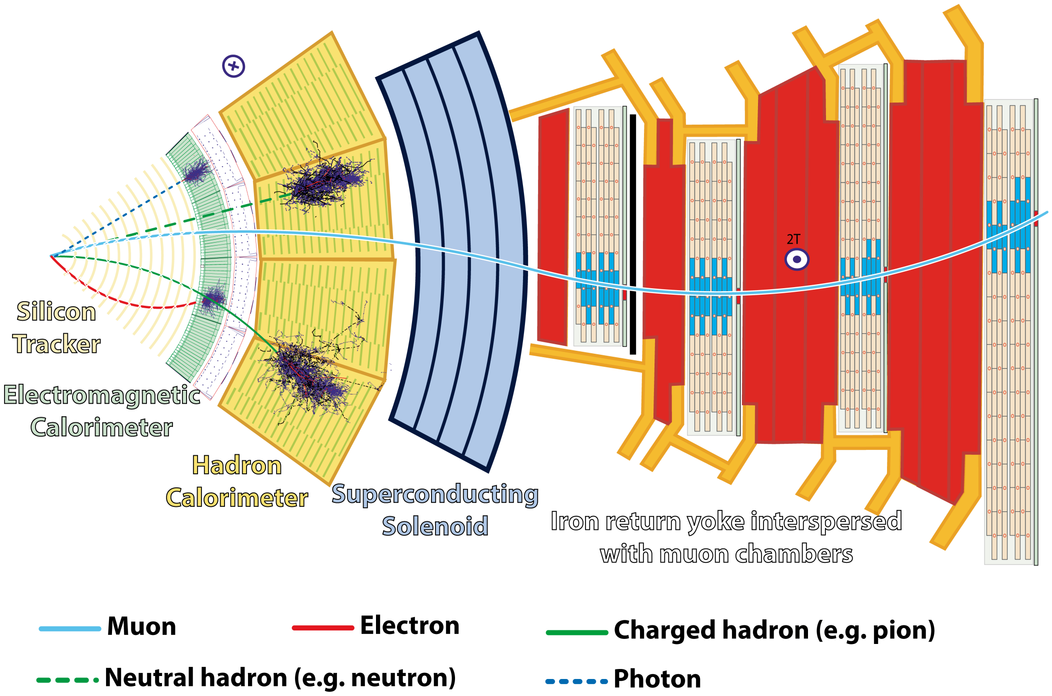

Figure 4.2: Cross-sectional slice of the CMS detector, showing the typical trajectories of each class of particle, from Ref. [42].

momentum, defined as the sum in quadrature of the particle's momentum in the x- and y-directions,

$$p_T = \sqrt{p_x^2 + p_y^2}\ . \tag{4.18}$$

The azimuthal angle in this plane, ϕ, is measure with respect to the x-axis. The polar angle, θ, is measured with respect to the z-axis, but a more useful third coordinate is the pseudorapidity,

$$\eta = -\ln\tan\left(\frac{\theta}{2}\right) \, , \tag{4.19}$$

which follows the same sign convention as the z-axis. This coordinate system is illustrated in Figure 4.3.

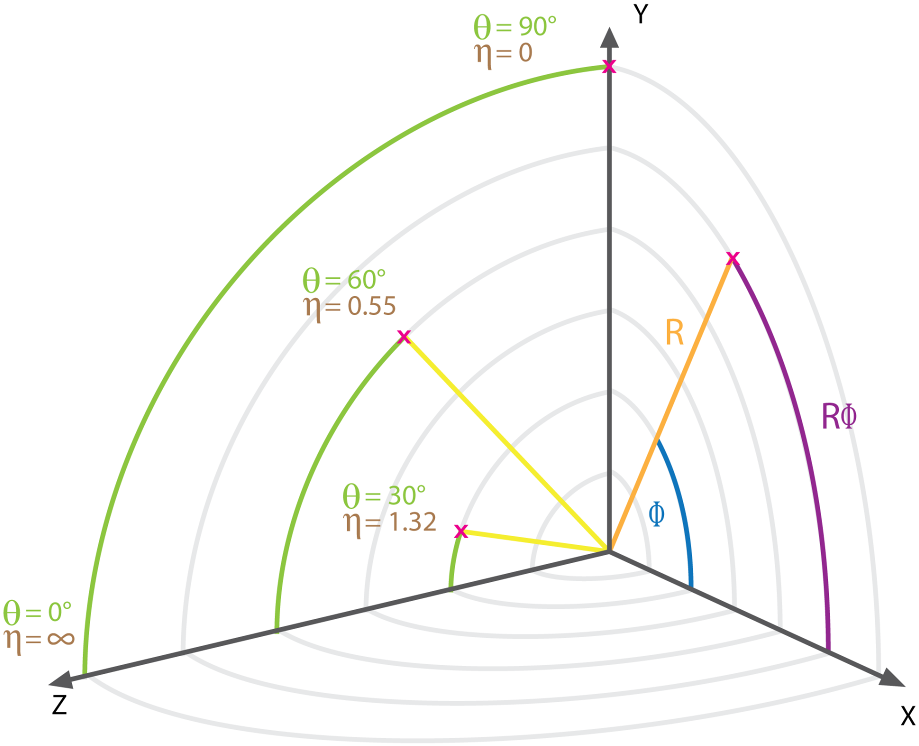

Figure 4.3: Illustration of the cylindrical coordinate system used to track particles inside CMS, from Ref. [43]. LHC Beam 2, not explicitly shown, runs in the positive $z-$direction.

4.1 Inner tracker

Precise measurements of charged particle momenta (which are essential for computing missing momentum) are performed by the inner tracker. The tracker is actually two sub-detectors, a small silicon pixel detector surrounded by a larger strip detector. Combined, the two sub-detectors occupy a cylindrical volume 5.8 m in length and 2.5 m in diameter. The pixel detector contains some 66 million pixels spread over three layers in the detector barrel and two in the endcap. It offers a hit position resolution of around 10 μm in the direction transverse to the beam and 20-40 μm in the longitudinal direction. The strip tracker is made of 9.3 million strips distributed over ten layers in the barrel and twelve in the endcap [44].

4.2 Electromagnetic calorimeter

The primary purpose of the hermetic electromagnetic calorimeter (ECAL) is to identify and measure the energy of electrons and photons. The ECAL is situated just outside of the tracker, with a portion of covering the barrel ($|\eta| < 1.479$), made up of 61,200 lead-tungstate ($PbWO_4$) scintillating crystals, as well as two portions covering the two endcaps ($1.566 < |\eta| < 3.0$), each made up of 7,324 crystals. $PbWO_4$ was chosen is the primary material for the detector because of its high density, short radiation length, and small Molire radius, all of which allow it to produce scintillation in fast, high-granularity photon showers. This scintillation occurs when electrons or photons pass through the detector, producing light in proportion to the particles' energies. Silicon photodetectors are attached to the backs of all crystals to detect the light and convert it to electrical signals that can be analyzed. The ECAL provides electron energy measurements with a resolution of

$$\frac{\sigma_E}{E} = \frac{2.8\%}{\sqrt{E}\ (\mathrm{GeV})} \oplus \frac{12\%}{\sqrt{E}\ (\mathrm{GeV})} \oplus 0.3$$

$$(\mathrm{stochastic} \oplus \mathrm{noise} \oplus \mathrm{constant})\ , \tag{4.20}$$

while the energy resolution for photons, as measured in simulated $h \to \gamma\gamma$ events, varies from 1.1% to 2.6% in the barrel and from 2.2% to 5% in the endcaps [45, 46, 47].

The ECAL is also responsible for distinguishing high energy "prompt" photons, such as those used to measure the $Z \to \nu\bar{\nu}$ background in this analysis (See Section 8.1), from those produced from the decays of neutral pions. A pair of photons from the decay $\pi^0 \to \gamma\gamma$ can be mis-characterized as a single high energy photon if the angle between them is small, as is often the case in the endcap region. To reduce photon mis-characterization, an additional preshower detector with granularity high enough to distinguish these pairs is placed in front of the ECAL endcaps, covering the range $1.65 < |\eta| < 2.6$, as shown in Figure 4.4 [48, 49].

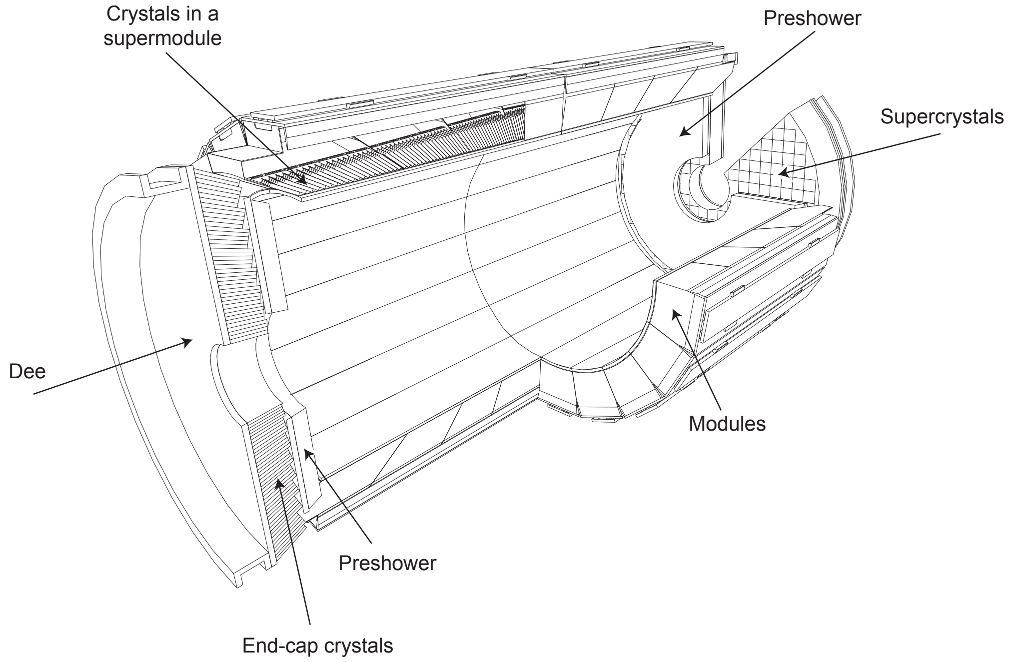

Figure 4.4: Layout of the ECAL showing the barrel, endcap, and preshower components, from Ref. [45].

4.3 Hadronic calorimeter

The hermetic sampling hadronic calorimeter (HCAL) performs a function analogous to that of the ECAL, namely measuring the energies of hadrons through scintillation. It is made up of layers of brass and steel absorbers interleaved with plastic scintillator tiles. When hadrons, particles made up of gluons and quarks, strike the absorber layers, they interact with the brass or steel producing "showers" of particles. As these showers pass through the scintillating layers, the plastic material produces light pulses that are collected by optical fibers then passed to readout boxes. A sum of signals from several layers is called a "tower," and its size is proportional to the energies of the particles.

The HCAL covers an η range up to 5.0, with 36 barrel wedges covering $|\eta| < 1.3$, 36 more wedges on two endcap disks covering $1.5 < |\eta| < 3.0$, and two forward calorimeters covering $3.0 < |\eta| < 5.0$. The HCAL provides the sole measurement of hadron momenta outside of the tracker acceptance ($|\eta| < 2.4$), giving it an essential role in jet and missing momentum reconstruction. The energy resolution of the HCAL was measured on a pion test beam and determined to be

$$\frac{\sigma_E}{E} = \frac{110\%}{\sqrt{E}\ (\text{GeV})} \oplus 9\% \text{ [50, 51]}. \tag{4.21}$$

4.4 Muon system

The outermost subdetector is the muon spectrometer, four stations of gas-ionization chambers interleaved between three layers of the magnetic field's iron return yoke. The muon system's main functions are identifying muons with high purity, providing rapid and efficient trigger decisions, and measuring muon momenta, which complements the work of the tracker, particularly at high momenta.

The system is made up of three types of detectors, the drift tube (DT, $|\eta| < 1.2$), cathode strip (CSC, $0.9 < |\eta| < 2.4$), and resistive plate (RPC, $|\eta| < 1.8$) chambers, as illustrated in Figure 4.5. When a muon passes through each type of chamber, it knocks electrons off the gas atoms. The electrons are picked up by the specific chamber technology, e.g., charged wires, providing positional coordinates for the muon. The full reconstruction of muons and is performed by fitting a trajectory to the muon hit pattern across all stations and in the inner tracker, as further described in Section 5.2 [52, 53, 54].

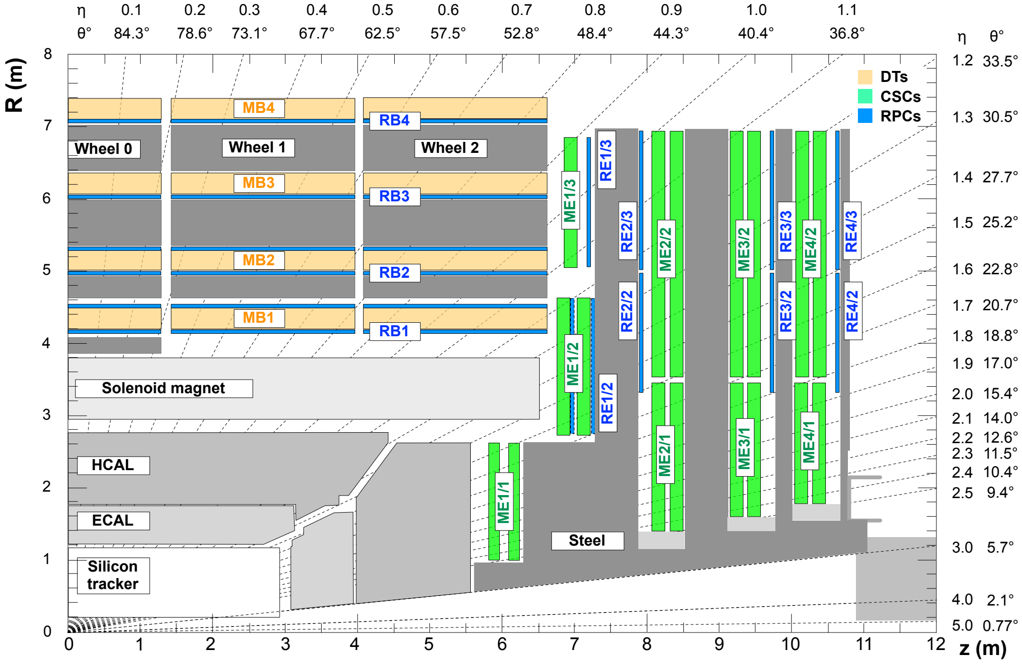

Figure 4.5: rz cross section of a quadrant of the CMS detector, with the muon system covering the region outside of the solenoid magnet, from Ref. [52].

4.5 Trigger and data acquisition

With a proton bunch spacing of 25 ns, the LHC collides protons at a record-high collision rate of 40 MHz. This rate far exceeds that which is feasible for data acquisition (DAQ) and storage, on the order of 1 kHz. A two-level trigger system is designed to reduce the rate manageable values by efficiently identifying and saving events that are candidates for interesting physics and throwing away those that are not.

The Level 1 (L1) trigger system makes hardware- and firmware-based decisions in a time interval of less than 4 μs using information from the calorimeters and muon system, typically reducing the rate to around 100 kHz. Events surviving L1 are received by readout electronics and processed by the high-level trigger (HLT), which makes software-based decisions using simplified versions of offline reconstruction algorithms, reducing the rate to the order of 1 kHz. Events surviving the HLT are stored for offline analysis [55].

Chapter 5

Particle reconstruction and identification

5.1 Tracks

The trajectories of charged particles produced in the primary interaction of each *pp* bunch crossing are reconstructed by the CMS tracking system. This system is tasked with tracking these particles with high efficiency while rejecting falsely reconstructed tracks at a high rate. As the LHC collides proton bunches at an instantaneous luminosity of $10^{34}\text{cm}^{-2}\text{s}^{-1}$, around 20 *pp* interactions occur in each proton bunch crossing. These multiple interactions, called pileup, contaminate the tracker with groups of unrelated hits, which may be combined to form falsely or poorly reconstructed tracks. As the proton bunches are separated by crossing intervals of just 25 ns, interactions from bunch crossings proceeding or following that of the primary interaction may also contribute pileup.

Track reconstruction begins with local measurements performed in the strip and pixel detectors. Signals above a noise suppression threshold in adjacent detector units, i.e., neighboring pixels or strips, are clustered into hits. The positions of pixel clusters are estimated through a first-pass fast algorithm, while the positions of clusters in the strip detector are determined through a charge-weighted averaging of the strip hit positions. In both detectors, cluster positions are corrected to account for the Lorentz drift of charge collected in the magnetic field [44].

Tracks are reconstructed from clustered hits using a track-finding algorithm based on a combinatorial Kalman filter [56]. A total of six track-finding iterations are performed. In each iteration, the algorithm attempts to reconstruct the most easily-identifiable tracks, e.g., those with the highest p_T, and then removes the hits associated with these reconstructed tracks. The combinatorics associated with track-finding are reduced with every iteration, thus simplifying the reconstruction of tracks that are harder to identify, e.g., those at low p_T. The reconstruction of each track is performed in four steps:

1. A seed is defined from two or three hits, depending on the iteration. This seed represents a preliminary estimate of the track trajectory parameters and their uncertainties.
2. The seed trajectory is extrapolated along the expected path of a charged particle in the magnetic field. Compatible hits along this path are added to the track.
3. A Kalman filter and smoother are used to fit for the best estimate of the trajectory parameters.
4. Track selection criteria, including minimum and maximum requirements on the number of tracker layers with hits, are imposed on the resulting track candidates. Those failing the criteria are discarded.

Additional details on track reconstruction are provided in Ref. [44].

5.1.1 Vertices

Identifying the primary interaction vertex (PV), i.e., the one that stems from the hard parton-parton interaction, is an essential step in event reconstruction. High-quality tracks with at least two pixel and five pixel+strip hits are fed into a deterministic annealing algorithm . The algorithm computes a probability for each track to be assigned to a potential vertex, and saves the vertices with at least two compatible tracks. The final position measurement for each vertex is obtained through an adaptive vertex fitter. Typically, the vertex with the largest $\sum p_T^2$ of tracks is chosen as the PV [44, 57].

5.2 Muons

Muon reconstruction is carried out in two steps. The first, called "local" reconstruction, occurs in individual chambers. Within a CSC, DT, or RPC chamber, electronic signals, called "hits," are detected on different layers. Straight line track "segments" are built from the reconstructed hits within one CSC or DT chamber. In an RPC chamber, individual strips with hits are clustered together to form "RPC hits." These local reconstruction algorithms are described in much more detail in Ref. [53].

In the "global" reconstruction step, the products of local reconstruction (CSC-segments, DT segments, or RPC hits) from multiple chambers are combined, often together with data from the inner tracker, to form the muons used for physics analyses. Global reconstruction begins as seeds are created from groups of CSC or DT segments. A Kalman filter technique is used to fit information from all three muon subdetectors into "standalone" muon candidates. These candidates may be combined with inner tracks to form either "tracker" muons or "global" muons. Inner track momenta are propagated to the muon system. Tracker muons are formed when a tracks are matched geometrically to DT or CSC segments, while global muons are formed when tracks match geometrically with standalone muons. Tracker muons tend to have higher efficiency and lower purity than global muons because they do not use information from all three subdetectors. They are especially useful for identifying muons at low-p_T, taking advantage of the fine resolution of the inner tracker. The additional information from the muon system used to reconstruct global muons, on the other hand, significantly improves momentum resolution, particularly at high-p_T ($\gtrsim 200$ GeV).

The values of a muon momenta are determined from an optimal combination of refits of available data, as described in Ref. [54]. Finally, muons are included in the Particle Flow (PF) algorithm (see Section 5.5), which may further refine the muon momentum values using event-level information.

Both tracker and global muons are used in this analysis, though they must also be identified by the PF algorithm. We impose the following additional quality requirements, defined in Ref. [54], on muon candidates:

- the track from the inner tracker must have a valid hit fraction of at least 0.8;
- and, for global muons, the χ^2/d.o.f. must be less than 3, the link between the tracker and standalone tracks on a common surface must have a local position χ^2 less than 12, the track kink finder logic must output a χ^2/d.o.f.

less than 20, and the candidate's segment compatibility likelihood score must be greater than 0.303;

- while, for tracker muons, the only requirement is that the candidate's segment compatibility likelihood score must be greater than 0.451.

5.3 Electrons

Electrons are reconstructed from tracks in the inner tracker matched to ECAL superclusters, or groups of cells. The trajectories of electron candidates are estimated by combining the track and cluster with a Gaussian sum filter. This filter takes into account any energy an electron may lose if it emits a photon through bremsstrahlung radiation before reaching the ECAL.

To distinguish prompt electrons from charged pions, electrons from semileptonic decays of b or c quarks, or electrons from photon conversions ($\gamma \rightarrow e^+e^-$), we impose a few additional requirements on the electron shower shape and the relative amount of energy associated with the electron in the ECAL and HCAL [58].

5.4 Photons

Photons are also reconstructed from ECAL superclusters. The easiest photons to identify are those that are not associated with any tracks, but a significant fraction of prompt photons convert to e^+e^- pairs before reaching the ECAL. These "converted" photons are selected from pairs of oppositely charged tracks that are not compatible with other electron signatures. Prompt photons are distinguished from photons from neutral hadron decays, e.g., $p^0 \to \gamma\gamma$, by the weighted variance of the energy deposited in the ECAL, $\sigma_{i\eta i\eta}$, as well as the amount of energy, if any, deposited in HCAL towers [59].

5.5 Particle flow

Higher-level physics objects are defined using the the particle-flow (PF) algorithm, which combines event-level information from each of the sub-detectors to optimally classify and reconstruct individual particles [60, 61]. A very brief summary of the algorithm follows:

- Inputs to the algorithm include tracks from the inner tracker and the muon system, as well as clusters of energy deposits in the calorimeters. These clusters are first seeded by local energy maxima in calorimeter cells. Signals from adjacent cells are clustered together if their energies exceed an energy noise threshold, 80 MeV in the ECAL, up to 300 MeV in the ECAL end-caps and 800 MeV in the HCAL.

- PF “blocks” are formed from a tentative linking between pairs of elements (tracks and/or clusters) in the detector. This linking is designed to fully reconstruct each particle while avoiding double-counting between sub-detectors. The quality of each link is quantified by a “link distance,” which is defined differently for each possible linking of elements and is described in the following sections. The resulting blocks typically contain one, two, or three elements. For each block the PF algorithm proceeds as follows:
  - A PF muon is defined as a global muon (see Section 5.2) whose momentum is compatible with that of track measured solely in the tracker. The corresponding tracker track is removed from the block.
  - A subset of the remaining tracks are used to postulate the presence of electrons. These tracks are characterized by short lengths and a loss of energy between tracker layers in the direction of the ECAL, consistent with bremsstrahlung radiation. Each track’s trajectory is extrapolated to the ECAL system, and if it is compatible with an ECAL cluster or a combination of cluster, the measurements of the track’s momentum and the total cluster energy are linked to form a PF electron. The corresponding track and cluster(s) are removed from the block.
  - The remaining elements can be linked to form PF charged hadrons, neutral hadrons, or photons. The remaining high-quality tracks are

compared to the HCAL and ECAL clusters. In the event that a track is linked to several clusters, only the energy of the closest cluster is used for comparison. If more than one track is linked to an HCAL cluster, the sum of the track momenta is used for comparison. Links formed between tracks and ECAL clusters are retained if the total calorimeter energy is smaller than the total charged-particle momentum in the event.

- PF charged hadrons arise from the remaining tracks linked to an HCAL clusters. The momentum and energy of the hadron are initially obtained from the track(s) under the charged pion mass hypothesis. If the momentum of the track(s) is compatible with the total calibrated calorimeter energy within uncertainties, the momentum of the charged-hadron is redefined by a fit of the measurements performed in the tracker and calorimeters. For many of these hadrons, the tracker measurement, which is typically performed with $O(100)$ MeV precision, provides the most useful information used in the fit. However, for hadrons with very high momenta ($\gtrsim 200$) GeV or high pseudo-rapidity, for which the tracker performance is degraded, the calorimeter energy measurement greatly improves the measurement. The ability to combine these complimentary measurements is one of the most significant strengths of the PF algorithm and is instrumental in jet reconstruction.

5.6 Jets

Jets are clustered from all PF objects using an anti-k_t algorithm. As is the case in other sequential recombination jet algorithms, this clustering algorithm is parametrized by "distance measures," which compare the energy and geometric separation between particles [62, 63]. The distance measures that govern this algorithm are d_{ij}, which represents the energy and geometric distance between two entities i and j (particles or pseudo-jets, see below), and d_{iB}, which represents the distance between entity i and the beam B. These measures are defined as follows:

$$d_{iB} = \frac{1}{p_{T,i}^2} \tag{5.22}$$

$$d_{ij} = \min\left(\frac{1}{p_{T,i}^2}, \frac{1}{p_{T,j}^2}\right) \cdot \frac{\Delta_{ij}^2}{R^2} \tag{5.23}$$

where $\Delta_{ij} = \sqrt{(y_i - y_j)^2 + (\phi_i - \phi_j)^2}$, and $p_{T,i}$, y_i and ϕ_i are the transverse momentum, rapidity, and azimuth of entity i, respectively. R is the jet radius parameter, which is set to 0.4 in most CMS analyses to balance the effects from energy lost from particles outside the jet area and energy contributions from sources not related to the underlying parton, including pileup interactions [64].

For every pair of entities (particles or pseudo-jets), this algorithm proceeds by comparing the two distance measures. If $d_{ij} < d_{iB}$, i and j are combined to form a pseudo-jet, while if $d_{iB} < d_{ij}$, then i is classified as a jet and is removed from further iterations. These distances are then recalculated for the next pair of entities and the process proceeds until all entities have been clustered or classified as individual jets. The initial list of entities is made up of all PF particles, and all of these particles are clustered into jets, with two exceptions:

- To reduce the impact of pileup interactions on jet counting and jet energy measurements, charged particles not originating from the primary vertex are removed from jets.
- In the control regions used to measure the $Z \rightarrow \nu\bar{\nu}$ background (see Section 8.1), to avoid double-counting particle momenta, any jets overlapping with a fully-identified muon, electron, or photon within $\Delta R < 0.4$ are discarded. This angular separation ΔR is defined as the 2D-separation in pseudo-rapidity and azimuth between the particle and the jet, $\Delta R = \sqrt{(\Delta\eta)^2 + (\Delta\phi)^2}$.

The structure of the distance parameters ($d \sim 1/p^2$) is chosen to minimize the effects of soft radiation. Consider a soft radiation particle i, a hard particle j, e.g., from hard radiation or a parton produced in the hard interaction, and another similarly soft particle k. If the first soft particle has a similar geometric separation from the other two particles ($\Delta_{ij} \sim \Delta_{ik}$), and if $p_{T,i} \ll p_{T,j}$ and $p_{T,i} \sim p_{T,k}$, then

$$d_{ij} = \min\left(\frac{1}{p_{T,i}^2}, \frac{1}{p_{T,j}^2}\right) \cdot \frac{\Delta_{ij}^2}{R^2} \approx \frac{1}{p_{T,j}} \cdot \frac{\Delta_{ij}}{R^2} \tag{5.24}$$

$$d_{ik} = \min\left(\frac{1}{p_{T,i}^2}, \frac{1}{p_{T,k}^2}\right) \cdot \frac{\Delta_{ik}^2}{R^2} \approx \frac{1}{p_{T,i}^2} \cdot \frac{\Delta_{ij}^2}{R^2} \tag{5.25}$$

$$d_{ij} \ll d_{ik} \tag{5.26}$$

and the soft particle is much more likely to be clustered into a jet with the hard particle, where it will make a small contribution to the jet's energy, than it is to be combined with the other soft one, in which case a high-momentum jet not originating from any hard parton might be created.

5.6.1 *b*-tagging

Many natural SUSY scenarios produce final states with b-quarks, which may emerge from the decays of stops, sbottoms, or SM top quarks. Jets that arise from b-hadronization can be identified with decent efficiency by exploiting the unique characteristics of b-hadrons, including large masses, long lifetimes, and occasional semi-leptonic decays. This analysis uses a multivariate classification algorithm called "Combined Secondary Vertex" (CSV), which uses a neural network to combine several discriminating variables, including, but not limited to,

- the presence of a secondary vertex displaced from the PV, which is characteristic of a particle with a long lifetime;
- the vertex mass;
- and the number of tracks associated with the vertex, which may be large for a heavy-flavor hadron.

The chosen working point of the CSV discriminator identifies b-jets with a 70% efficiency for misidentification rates of around 20% and 1% for charm- and light-flavor-parton jets, respectively [65, 66, 67].

Part 3

Searching for SUSY

Chapter 6

Data samples and simulation

6.1 13 TeV data samples

This search is performed on a data samples corresponding to 36.3 fb^{-1} of pp collisions at $\sqrt{s} = 13$ TeV collected by the CMS detector. The total luminosity delivered during this period by the LHC is 41.40 fb^{-1} and the total recorded by CMS is 38.27 fb^{-1} [68]. The 36.3 fb^{-1} sample used in this search is a subset of the luminosity recorded by CMS while all sub-detectors were fully operational and the magnetic field strength was 3.8 T.

A plot of the cumulative luminosity delivered by the LHC and the integrated luminosity recorded by CMS versus the day of the year is shown in Figure 6.1, along with a non-cumulative distribution of the total luminosity delivered and recorded each day.

6.2 MC simulation

6.2.1 Standard model backgrounds

While the SM background contributions to the search region are largely measured using control regions in data, Monte Carlo (MC) simulations are vital to several aspects of this analysis, including:

- Designing and optimizing the search strategy prior to data-taking
- Validating the methods used to measure the backgrounds (e.g., through MC closure tests)
- Determining components of the translation factors used to extrapolate from the number of events observed in control regions to the estimated background yield in the search region (e.g., lepton acceptance and efficiency, photon fragmentation rates, etc.)
- Commissioning and validation of data during the first weeks of collisions each year

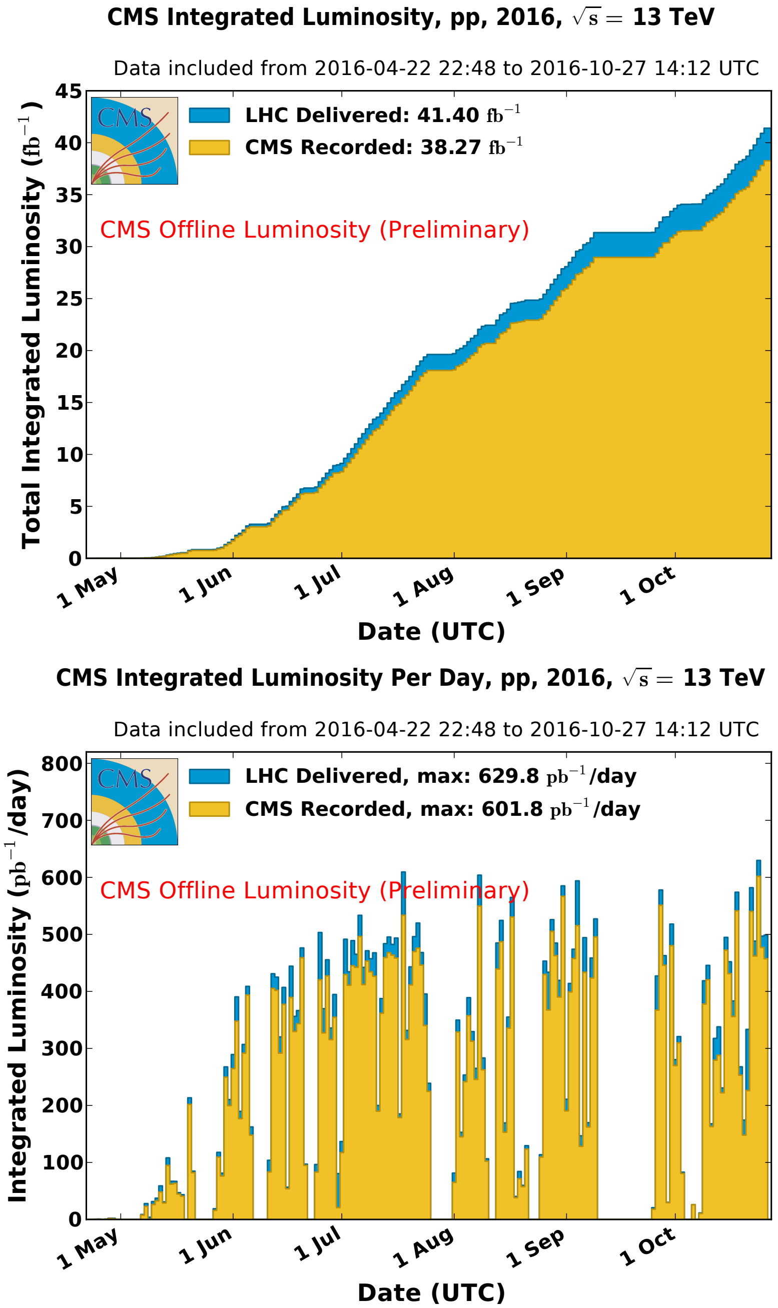

Figure 6.1: Top: cumulative luminosity delivered by the LHC (blue) and recorded by CMS (orange) during stable beams and for *pp* collisions at $\sqrt{s} = 13$ TeV in 2016. Bottom: total luminosity delivered and recorded each day (not cumulative) in 2016. From Ref. [68].

The MadGraph5_aMC@NLO 2.2.2 [69] event generator at leading order (LO) is used to simulate $t\bar{t}$, W+jets, Z+jets, γ+jets, and QCD multijet events. This generator at next-to-leading order (NLO) is used to describe single top events in the s-channel, diboson events (WW, ZZ, and WZ production), and rare processes ($t\bar{t}W$, $t\bar{t}Z$, $t\bar{t}\ t\bar{t}$, and triboson production), except for WW events in which both $W^{\pm}$ bosons decay to a charged lepton and a neutrino, which are generated with the POWHEG v1.0 [70, 71, 72, 73, 74] program at NLO. Single top events in the t- and tW-channels are also generated with POWHEG at NLO.

The NNPDF3.0LO [75] parton distribution functions (PDF) are used for the samples generated at leading order, and the NNPDF3.0NLO [75] PDFs for the samples generated at NLO.

The samples are normalized using the most accurate cross section calculations currently available [73, 74, 69, 76, 77, 78, 79, 80, 81, 82, 83, 84], with NLO or next-to-NLO accuracy for all processes except for QCD and γ+jets, which are both normalized to LO cross sections. The samples used, as well as their cross sections and effective luminosities, are summarized in Tables 6.1–6.8.

The parton showering and hadronization in all MC samples are modeled by the PYTHIA 8.2 [85] program. The effects of pileup are modeled by generating all events with a distribution of pp interactions per bunch crossing with a mean of 20. The detector response is simulated using the Geant4 [86] package.

Table 6.1: SM $t\bar{t}$ MC samples used in the analysis. The cross sections are calculated to NNLO.

Dataset	σ (pb)	$\int \mathcal{L}$ dt(fb^{-1})
TTJets_TuneCUETP8M1_13TeV-madgraphMLM-pythia8	831.76	12.34
TTJets_SingleLeptFromT_TuneCUETP8M1_13TeV-madgraphMLM-pythia8	182.72	283.90
TTJets_SingleLeptFromTbar_TuneCUETP8M1_13TeV-madgraphMLM-pythia8	182.72	326.48
TTJets_DiLept_TuneCUETP8M1_13TeV-madgraphMLM-pythia8	88.34	346.25
TTJets_HT-600to800_TuneCUETP8M1_13TeV-madgraphMLM-pythia8	2.734	5231.81
TTJets_HT-800to1200_TuneCUETP8M1_13TeV-madgraphMLM-pythia8	1.121	9416.61
TTJets_HT-1200to2500_TuneCUETP8M1_13TeV-madgraphMLM-pythia8	0.198	14819.34
TTJets_HT-2500toInf_TuneCUETP8M1_13TeV-madgraphMLM-pythia8	0.002	221088.29

Table 6.2: SM QCD MC samples used in the analysis. All cross sections are calculated to LO.

Dataset	σ (pb)	$\int \mathcal{L}$ dt(fb^{-1})
QCD_HT200to300_TuneCUETP8M1_13TeV-madgraphMLM-pythia8	1735000	0.03
QCD_HT300to500_TuneCUETP8M1_13TeV-madgraphMLM-pythia8	366800	0.16
QCD_HT500to700_TuneCUETP8M1_13TeV-madgraphMLM-pythia8	29370	1.95
QCD_HT700to1000_TuneCUETP8M1_13TeV-madgraphMLM-pythia8	6524	6.68
QCD_HT1000to1500_TuneCUETP8M1_13TeV-madgraphMLM-pythia8	1064	12.62
QCD_HT1500to2000_TuneCUETP8M1_13TeV-madgraphMLM-pythia8	121.5	32.63
QCD_HT2000toInf_TuneCUETP8M1_13TeV-madgraphMLM-pythia8	25.42	239.30

Table 6.3: SM $Z \to \nu\nu$+jets MC samples used in the analysis. The cross sections are calculated to NNLO.

Dataset	σ (pb)	$\int \mathcal{L}$ dt(fb^{-1})
ZJetsToNuNu_HT-100To200_13TeV-madgraph	344.3	54.21
ZJetsToNuNu_HT-200To400_13TeV-madgraph	95.23	209.12
ZJetsToNuNu_HT-400To600_13TeV-madgraph	13.19	77.25
ZJetsToNuNu_HT-600To800_13TeV-madgraph	3.221	1754.33
ZJetsToNuNu_HT-800To1200_13TeV-madgraph	1.474	1462.80
ZJetsToNuNu_HT-1200To2500_13TeV-madgraph	0.359	1018.45
ZJetsToNuNu_HT-2500ToInf_13TeV-madgraph	0.00820	49463.85

Table 6.4: SM $W \to \ell\nu$+jets MC samples used in the analysis. The cross sections are calculated to NNLO.

Dataset	σ (pb)	$\int \mathcal{L}$ dt(fb^{-1})
WJetsToLNu_HT-100To200_TuneCUETP8M1_13TeV-madgraphMLM-pythia8	1627.45	18.16
WJetsToLNu_HT-200To400_TuneCUETP8M1_13TeV-madgraphMLM-pythia8	435.24	45.88
WJetsToLNu_HT-400To600_TuneCUETP8M1_13TeV-madgraphMLM-pythia8	59.18	123.64
WJetsToLNu_HT-600To800_TuneCUETP8M1_13TeV-madgraphMLM-pythia8	14.58	221.32
WJetsToLNu_HT-800To1200_TuneCUETP8M1_13TeV-madgraphMLM-pythia8	6.66	1123.13
WJetsToLNu_HT-1200To2500_TuneCUETP8M1_13TeV-madgraphMLM-pythia8	1.608	153.44
WJetsToLNu_HT-2500ToInf_TuneCUETP8M1_13TeV-madgraphMLM-pythia8	0.039	6497.28

Table 6.5: SM single-top MC samples used in the analysis. The cross sections are calculated to NLO.

Dataset	σ (pb)	$\int \mathcal{L}$ dt(fb^{-1})
ST_s-channel_4f_leptonDecays_13TeV-amcatnlo-pythia8_TuneCUETP8M1	3.340	186.52
ST_t-channel_antitop_4f_leptonDecays_13TeV-powheg-pythia8_TuneCUETP8M1	26.23	63.52
ST_t-channel_top_4f_leptonDecays_13TeV-powheg-pythia8_TuneCUETP8M1	44.07	70.95
ST_tW_antitop_5f_inclusiveDecays_13TeV-powheg-pythia8_TuneCUETP8M1	35.60	27.18
ST_tW_top_5f_inclusiveDecays_13TeV-powheg-pythia8_TuneCUETP8M1	35.60	28.04

Table 6.6: SM diboson and other rare process MC samples used in the analysis. The cross sections are calculated to NNLO.

Dataset	σ (pb)	$\int \mathcal{L}$ dt(fb^{-1})
TTZToLLNuNu_M-10_TuneCUETP8M1_13TeV-amcatnlo-pythia8	0.253	732.43
TTZToQQ_TuneCUETP8M1_13TeV-amcatnlo-pythia8	0.530	662.95
TTWJetsToLNu_TuneCUETP8M1_13TeV-amcatnloFXFX-madspin-pythia8	0.204	637.67
TTWJetsToQQ_TuneCUETP8M1_13TeV-amcatnloFXFX-madspin-pythia8	0.403	1068.83
WWTo1L1Nu2Q_13TeV_amcatnloFXFX_madspin_pythia8	50.00	56.16
WWTo2L2Nu_13TeV-powheg	12.18	163.10
WZTo1L1Nu2Q_13TeV_amcatnloFXFX_madspin_pythia8	10.71	1047.14
WZTo1L3Nu_13TeV_amcatnloFXFX_madspin_pythia8	3.058	299.22
ZZTo2Q2Nu_13TeV_amcatnloFXFX_madspin_pythia8	4.040	4674.17
ZZTo2L2Q_13TeV_amcatnloFXFX_madspin_pythia8	3.220	3037.46
TTTT_TuneCUETP8M1_13TeV-amcatnlo-pythia8	0.009	45574.54
WWZ_TuneCUETP8M1_13TeV-amcatnlo-pythia8	0.165	1337.26
WZZ_TuneCUETP8M1_13TeV-amcatnlo-pythia8	0.056	3935.06
ZZZ_TuneCUETP8M1_13TeV-amcatnlo-pythia8	0.014	15296.85

Table 6.7: SM DY+jets MC samples used in the analysis. The cross sections are calculated to NNLO.

Dataset	σ (pb)	$\int \mathcal{L}$ dt(fb^{-1})
DYJetsToLL_M-50_HT-100to200_TuneCUETP8M1_13TeV-madgraphMLM-pythia8	183.10	58.05
DYJetsToLL_M-50_HT-200to400_TuneCUETP8M1_13TeV-madgraphMLM-pythia8	50.49	192.16
DYJetsToLL_M-50_HT-400to600_TuneCUETP8M1_13TeV-madgraphMLM-pythia8	6.99	1189.20
DYJetsToLL_M-50_HT-600toInf_TuneCUETP8M1_13TeV-madgraphMLM-pythia8	2.70	1907.56

Table 6.8: SM γ+jets MC samples used in the analysis. The cross sections are calculated to LO.

Dataset	σ (pb)	$\int \mathcal{L}$ dt(fb^{-1})
GJets_DR-0p4_HT-100To200_TuneCUETP8M1_13TeV-madgraphMLM-pythia8	5000	3.081
GJets_DR-0p4_HT-200To400_TuneCUETP8M1_13TeV-madgraphMLM-pythia8	1079	54.53
GJets_DR-0p4_HT-400To600_TuneCUETP8M1_13TeV-madgraphMLM-pythia8	125.9	148.2
GJets_DR-0p4_HT-600ToInf_TuneCUETP8M1_13TeV-madgraphMLM-pythia8	43.36	500.1

6.2.2 Signal models and scans

The conventions of natural SUSY discussed in Section 2.2.1 lend themselves well to simplified SUSY models, i.e., scenarios in which only a few SUSY particles are relevant and accessible at the LHC. The results of this search are interpreted in the context of simplified models [87, 88, 89, 90] of strong production of gluino and squark pairs. Each model is characterized by two parameters, the mass of the pair-produced supersymmetric particle (e.g., $\tilde{g}$) and the mass of the lightest supersymmetric particle (LSP). With a few exceptions in some models, the masses of all other supersymmetric particles are generally assumed to be so large that they have no impact on the production or decay kinematics. The gluino is assumed to have a short lifetime [91].

Four scenarios of gluino production and four scenarios of squark production are considered. These scenarios are summarized in Table 6.9. Simplified Feynman diagrams are provided for each scenario in Figures 6.2–6.4. Note that in the T1qqqq, T5qqqqVV, and T2qq scenarios, $q = u, d, c, s$ and the four corresponding light-flavored squarks are assumed to be degenerate. In the case of T1qqqq and T5qqqqVV, the gluino decays to final states including each flavor with equal probability.

In each gluino production scenario, the gluino decays via off-shell squark (e.g., $\tilde{g} \to \tilde{q}\bar{q} \to q\bar{q}\tilde{\chi}_1^0$). In the T5qqqqVV scenario, the gluino decays to a light-flavored quark-antiquark pair and either the next-to-lightest neutralino $\tilde{\chi}_2^0$ or the lightest chargino $\tilde{\chi}_1^\pm$. These electroweak particles then decay to the LSP ($\tilde{\chi}_1^0$) and either an on- or off-shell SM Z boson, in the case of the $\tilde{\chi}_2^0$, or an on- or off-shell SM $W^\pm$ boson, in the case of the $\tilde{\chi}_1^\pm$. If the decay proceeds via a $W^\pm$ boson, the quark and anti-quark do not have the same flavor. The probability for the decay to proceed via the chains involving the $\tilde{\chi}_2^0$, $\tilde{\chi}_1^+$, or $\tilde{\chi}_1^-$ is assumed to be 1/3 for each chain. The masses of the intermediate $\tilde{\chi}_2^0$ and $\tilde{\chi}_1^\pm$ are equal to the mean of the $\tilde{g}$ and $\tilde{\chi}_1^0$ masses; that is,

$$\begin{aligned} m_{\tilde{\chi}_2^0} &= \frac{1}{2}(m_{\tilde{g}} + m_{\tilde{\chi}_1^0}) \\ m_{\tilde{\chi}_1^\pm} &= \frac{1}{2}(m_{\tilde{g}} + m_{\tilde{\chi}_1^0}) \end{aligned}$$

In the T1tbtb scenario, each gluino decays either as $\tilde{g} \to \bar{t}b\tilde{\chi}_1^+$ or its charge conjugate, each with a 50% probability. The $\tilde{\chi}_1^+$ is assumed to be nearly degenerate with the $\tilde{\chi}_1^0$, which is characteristic of the two particles appearing in the same $SU(2)$ multiplet. The $\tilde{\chi}_1^+$ decays to the $\tilde{\chi}_1^0$ and an off-shell $W^\pm$ boson.

The T1tttt, T1bbbb, T2tt, and T2bb models each have a unique decay chain; that is, the branching ratio of the pair-produced particle to the given final state is 1.

The signal samples are generated with the MadGraph5_aMC@NLO program at leading order, which generates up to two partons present in addition to the

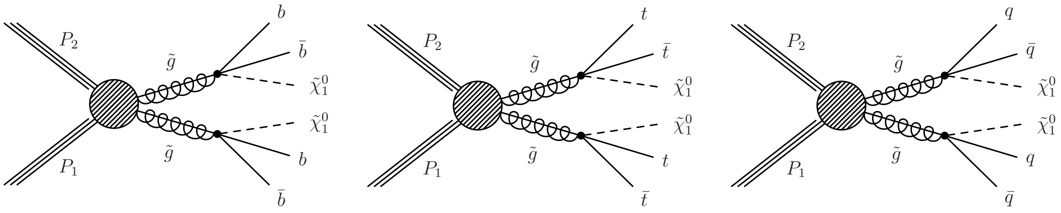

Figure 6.2: Simplified Feynman diagrams for the gluino production scenarios considered in this analysis, the (left) T1bbbb, (middle) T1tttt, and (right) T1qqqq simplified models.

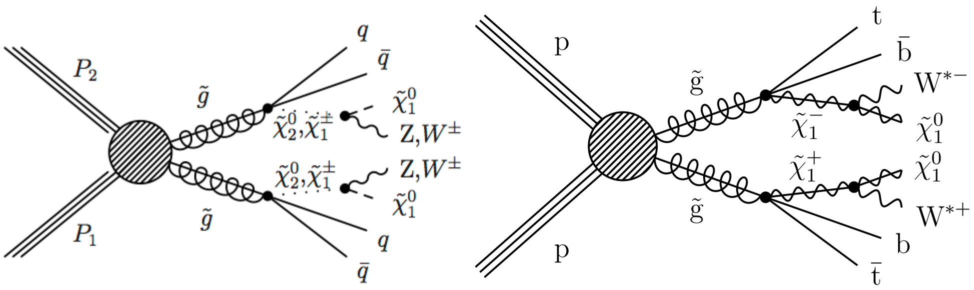

Figure 6.3: Simplified Feynman diagrams for the additional gluino production scenarios considered in this analysis, the (left) T5qqqqVV and (right) T1tbtb simplified models. For the T5qqqqVV model, if the gluino decays as $\tilde{g} \to \tilde{q}_i\bar{q}_i \to q_j\bar{q}_i\tilde{\chi}_1^\pm \to q_j\bar{q}_iW^\pm\tilde{\chi}_1^0$. the quark q_j and antiquark $\bar{q}_i$ do not have the same flavor.

gluino pair. The decays of the gluino are modeled with a phase-space matrix element [85]. The parton showering and hadronization are modeled by the PYTHIA 8.2 program. The signal production cross sections are computed [92, 93, 94, 95, 96] with NLO plus next-to-leading-logarithm (NLL) accuracy.

Enormous computational resources are required to fully generate MC samples for and simulate the detector response of over one thousand individual signal mass points across all seven SMS scenarios. To reduce the time and resources needed to

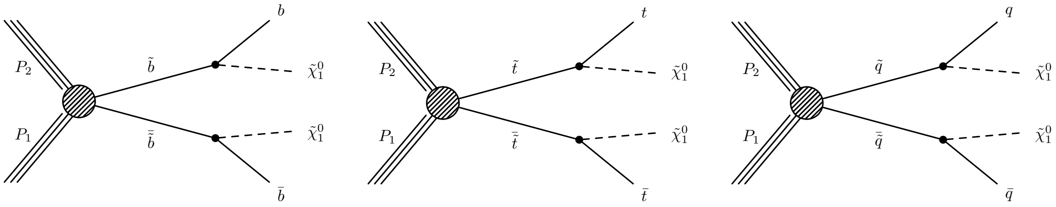

Figure 6.4: Simplified Feynman diagrams for the squark production scenarios considered in this analysis, the (left) T2bb, (middle) T2tt, and (right) T2qq simplified models.

Table 6.9: SMS signal models considered in the interpretation of this analysis. Here $q_i(j) = u, d, c, s$, $q_i \neq q_j$, and the four light-flavored squarks are assumed to be degenerate.

SMS Model	Production	Decay
T1bbbb	$pp \to \tilde{g}\tilde{g}$	$\tilde{g} \to b\bar{b}\tilde{\chi}_1^0$
T1tttt	$pp \to \tilde{g}\tilde{g}$	$\tilde{g} \to t\bar{t}\tilde{\chi}_1^0$
T1qqqq	$pp \to \tilde{g}\tilde{g}$	$\tilde{g} \to q\bar{q}\tilde{\chi}_1^0$
T5qqqqVV	$pp \to \tilde{g}\tilde{g}$	$\tilde{g} \to q_i\bar{q}_i Z\tilde{\chi}_1^0$ $\tilde{g} \to q_i\bar{q}_j W^{\pm}\tilde{\chi}_1^0$
T2bb	$pp \to \tilde{b}\bar{\tilde{b}}$	$\tilde{b} \to b\tilde{\chi}_1^0$
T2tt	$pp \to \tilde{t}\bar{\tilde{t}}$	$\tilde{t} \to t\tilde{\chi}_1^0$
T2qq	$pp \to \tilde{q}\bar{\tilde{q}}$	$\tilde{q} \to q\tilde{\chi}_1^0$
T1tbtb	$pp \to \tilde{g}\tilde{g}$	$\tilde{g} \to \bar{t}b\tilde{\chi}_1^+$ $\tilde{g} \to t\bar{b}\tilde{\chi}_1^-$

fully simulate all signal processes, the detector response is modeled with the CMS fast simulation program [97, 98]. For several model points, we fully simulate the detector response Geant4-based simulation so we can directly compare the fast and full simulation performance. In general, the fast simulation produces results consistent with those obtained through full simulation. We correct for two notable differences observed between full and fast simulation; we apply a correction of 1%

to account for differences in the efficiency of the jet quality requirements [99], and corrections of 3–10% to account for differences in the efficiency of the b-jet tagging algorithm.

As in the case of the SM background samples generated at leading order, NNPDF3.0LO PDFs are used for the signal samples. All signal events are generated with a pileup distribution with a mean of 20. This distribution is corrected to match the corresponding distribution in data.

Chapter 7

Designing an inclusive search

Since SUSY offers an enormous variety of models and final states, we design our search to be inclusive and generic so that we maintain sensitivity to a diverse array of new physics scenarios. The SMS models described in Section 6.2.2 serve as general guidelines for designing our search. Since all of the models include gluinos or squarks decaying to multiple hadrons and weakly-interacting SUSY particles, which escape detection, we conduct our search in a sample of events with at least two jets and missing transverse momentum. As introduce in Section 2.2.2, missing transverse momentum (H_T^{miss}) is defined as the negative of the vector sum of jet transverse momenta,

$$H_T^{\text{miss}} = \left| -\sum_{\text{jets}} \vec{p}_T \right| , \tag{7.27}$$

and is a proxy for the net momenta of all undetectable particles, i.e., neutralinos or neutrinos. Standard model processes with final states containing genuine (not instrumental) missing momentum involve either the decay of a Z boson to a pair of neutrinos ($Z \to \nu\bar{\nu}$) or the decay of $W^{\pm}$ boson to a charged lepton and a neutrino ($W \to \ell\nu$). To suppress the latter background process, we restrict our search region to events containing no isolated electrons or muons.

7.1 Trigger

Events in the zero lepton search region (SR) are selected using a set of triggers with online E_T^{miss} and H_T^{miss} thresholds of 100-120 GeV. During the second half of 2016, the lower thresholds (100, 100 GeV) were prescaled. The efficiency of the logical OR of these triggers in the full 2016 data set is measured in a sample of events selected by a single electron trigger with an offline requirement of a 25 GeV electron. This selection yields a relatively pure ($> 95\%$) sample of $t\bar{t}$ and W+jets events with genuine missing momentum from neutrinos. The efficiency measured in this sample is used to take into account any trigger inefficiency when determining the expected amount of signal, which has genuine missing momentum from neutralinos, in the search region.

The trigger reaches a plateau efficiency of around 98% for an offline selection of $H_T^{\text{miss}} > 250$ GeV and $300 < H_T < 1500$ GeV. The trigger efficiency exhibits

Table 7.1: Trigger efficiency for the logical OR of the search region triggers, measured in a sample selected by a single electron trigger. Uncertainties are statistical only.

Trigger ϵ [%]	$250 < H_T^{\text{miss}} \leq 300$ GeV	$300 < H_T^{\text{miss}} \leq 350$ GeV	$350 < H_T^{\text{miss}} \leq 500$ GeV	$H_T^{\text{miss}} > 500$ GeV
$300 < H_T < 1500$ GeV	$98.1^{+0.1}_{-0.1}$	$98.8^{+0.1}_{-0.2}$	$99.3^{+0.1}_{-0.2}$	$98.9^{+0.3}_{-0.4}$
$H_T > 1500$ GeV	$88.0^{+2.7}_{-3.3}$	$93.0^{+2.7}_{-3.9}$	$92.8^{+2.2}_{-2.9}$	$98.4^{+1.0}_{-2.1}$

a slower turn-on as a function of offline H_T^{miss} at higher values of H_T, so we report efficiency values in four bins of offline H_T^{miss} and two bins of offline H_T in Table 7.1. We observe no statistically significant dependence of the efficiency on N_{jet} and $N_{b\text{-jet}}$. All of these efficiency measurements take into account the trigger prescaling at lower H_T^{miss} thresholds throughout part of the year.

7.2 Baseline event selection

The following requirements define the baseline selection:

- $N_{\text{jet}} \geq 2$: All events are required to contain at least two "good" jets, defined by
    - $p_T > 30$ GeV,
    - $|\eta| < 2.4$,
    - and satisfying the "loose" jet ID criteria defined in Section 5.6.

- $H_T > 300$ GeV, where $H_T = \sum_{\text{jets}} p_T$. The jets must meet the criteria listed above. This variable is a proxy for the mass-energy scale of an event.

- $H_T^{\text{miss}} > 300$ GeV. All jets included in the vector sum must satisfy $p_T > 30$ GeV, $|\eta| < 5$. The jets within tracker acceptance ($-2.4 < \eta < 2.4$) must also satisfy the "loose" jet ID described above. This variable is arguably the most valuable discriminator between SM and SUSY processes.

- Muon veto:

  Muon candidates are selected using the selection described in 5.2 and are required to have $p_T > 10$ GeV and $|\eta| < 2.4$. To distinguish between prompt muons and muons from b-hadron decays, muons are required to satisfy an isolation requirement, $I_{\text{mini}} < 0.2$. I_{mini}, or mini-isolation, is a measure of the amount of activity, mostly hadronic, around a lepton candidate. Leptons produced in the decay of a heavy-flavor hadron will tend to have higher values of I_{mini}, while prompt leptons, i.e. those produced in the decay of an on-shell W, will tend to have lower values of I_{mini}. I_{mini} is defined as:

$$\begin{aligned} I_{\text{mini}} = \frac{1}{p_T^{\text{lep}}} \Bigg\{ & \sum_{\text{cone}} p_T(\text{charged hadrons from PV}) \\ & + \max\Bigg[0, \sum_{\text{cone}} p_T(\text{phot.}) + \sum_{\text{cone}} p_T(\text{ntrl. had.}) \\ & - \frac{1}{2}\sum_{\text{cone}} p_T(\text{chg. had. not from PV})\Bigg]\Bigg\} \end{aligned}$$

In the above equation, the transverse momenta of PF candidates within a cone of $\Delta R = \sqrt{(\Delta\eta)^2 + (\Delta\phi)^2} < 0.4$ around the muon candidate are summed and then divided by the p_T of the muon candidate. The first term sums over candidates identified as charged hadrons (e.g., pions or protons) originating from the primary vertex. The following terms sums over candidates identified as photons and neutral hadrons (e.g., kaons or neutrons). To account for possible pileup contamination from these neutral candidates, we subtract one half of the total transverse momenta of particles identified by PF as charged hadrons *not* originating from the primary vertex. The rationale behind this approximation is that the soft activity (not from the primary interaction) should be composed of around one half of the number of charged particles as neutral particles. To further suppress cosmic muons and muons from hadronic decays, we also require the muon tracks to have a transverse impact parameter less than 2 mm and a longitudinal separation less than 5 mm with respect to the PV. Any event with a muon satisfying all of the above criteria is vetoed.

- Electron veto:

  Electron candidates are selected using the selection described in Section 5.3 and are required to have $p_T > 10$ GeV and $|\eta| < 2.5$. As in the case of muons, electron candidates are also required to pass an isolation cut, $I_{\text{mini}} < 0.1$, where I_{mini} is defined as above. Any event with an electron satisfying all of these criteria is vetoed.

- Isolated track vetoes: Following the event selection described above, including the muon and electron event vetoes, the dominant source of background for many of the search regions is $t\bar{t}$, single-top, and W+jets events with one $\mathrm{W} \to \ell\nu$ decay. In about half these background events, the W boson decays to a τ lepton and the τ lepton decays hadronically, while in the other half, an electron or muon is not identified or does not satisfy the criteria for an isolated electron or muon candidate given above. To suppress these backgrounds, we reject events with one or more isolated charged track. The requirements for the definition of an isolated track differ slightly depending on whether the track is identified as leptonic or hadronic by the PF algorithm. For leptonic tracks, we require:

  - $p_T > 5$ GeV,
  - $I_{\text{track}} < 0.2$,

  where I_{track} is the scalar p_T sum of other charged tracks within $\Delta R \equiv \sqrt{(\Delta\phi)^2 + (\Delta\eta)^2} < 0.3$ of the primary track, divided by the p_T value of the primary track. For hadronic tracks, we apply slightly tighter requirements to reduce hadronic (non-τ) signal loss:

- $p_T > 10$ GeV,
- $I_{\text{track}} < 0.1$.

Since the isolation sum does not include neutral-particle candidates, the isolation distributions and efficiencies of leptonic tracks should be similar to those of pions from single-prong τ decays, e.g., $\tau \to \pi\nu$. This similarity is exploited to validate the rate at which the hadronic track veto suppresses $\tau \to$ hadrons events in Section 8.2.3. To retain more signal, thus improving signal-to-background event discrimination, isolated tracks are considered only if they satisfy

$$m_T(\text{track}, E_T^{\text{miss}}) = \sqrt{2 p_T^{\text{track}} E_T^{\text{miss}} (1 - \cos\Delta\phi)} < 100 \text{ GeV}, \qquad (7.28)$$

where p_T^{track} is the transverse momentum of the track and E_T^{miss} is a variable defined in Refs. [100, 101] that is effectively identical to H_T^{miss} for genuine-H_T^{miss} processes. $\Delta\phi$ is the azimuthal separation between the track and E_T^{miss}. Most isolated tracks in standard model background events originate from the decay of a single on-shell W, meaning the invariant mass of the W decay products (i.e. the lepton and neutrino) is $m_W \approx 80$ GeV [102]. The transverse mass of the track-E_T^{miss} system, a proxy to m_W in standard model events with one $W \to \ell\nu$ decay, will thus be around or below m_W. No such restriction applies to most signal events, in which the missing momentum originates from multiple neutralinos, so this requirement preferentially saves signal over background. To reduce the influence of tracks from extraneous pp interactions (pileup), isolated tracks are considered only if their nearest distance of approach along the beam axis to a reconstructed vertex is smaller for the primary event vertex than for any other vertex:

$$\min(d_z(\mathrm{V})) = d_z(\mathrm{PV}) \; . \tag{7.29}$$

- Angular cut:

  SM processes not involving neutrinos can also produce final states with missing momentum if jets are poorly reconstructed. The majority of strongly-produced QCD multijet events in our high-H_T^{miss} search region have at least one jet with drastically undermeasured momentum and thus a spurious momentum imbalance. A signature of such an event is a jet closely aligned in direction with the H_T^{miss} vector, as illustrated in Figure 7.1. To suppress this background, we reject all events in which the two highest-p_T jets lie within 0.5 radians of the H_T^{miss} vector in the azimuthal coordinate:

$$\begin{aligned} &\Delta\phi(j_1,\ H_T^{\mathrm{miss}}) > 0.5 \\ &\Delta\phi(j_2,\ H_T^{\mathrm{miss}}) > 0.5 \end{aligned} \tag{7.30}$$

Figure 7.1: Sketch of a typical QCD multijet event. The true (generated) jet momenta are represented by the gray arrows, while the reconstructed jet momenta are shown in black. One jet's momentum is severely undermeasured, resulting in a false missing momentum imbalance.

This requirement is relaxed for the third- and fourth-highest-p_T jets:

$$\begin{aligned} &\Delta\phi(j_3,\ H_T^{\text{miss}}) > 0.3 \\ &\Delta\phi(j_4,\ H_T^{\text{miss}}) > 0.3 \end{aligned} \tag{7.31}$$

No such requirement is placed on other jets.

7.3 Search binning

7.3.1 Nominal analysis: 174 bins

The signal models we consider differ from each primarily in the number of quarks and heavy-flavor quarks produced in the gluino and/or squark decay. Each of these models can be further divided into separate topologies with a different

Table 7.2: Definition of the search intervals in the H_T^{miss} and H_T variables. Intervals 1 and 4 are discarded for $N_{\text{jet}} \geq 7$.

Interval	H_T^{miss} [GeV]	H_T [GeV]
1	300–350	300–500
2	300–350	500–1000
3	300–350	>1000
4	350–500	350–500
5	350–500	500–1000
6	350–500	>1000
7	500–750	500–1000
8	500–750	>1000
9	>750	750–1500
10	>750	>1500

mass splitting between the gluino/squark and LSP. Should we observe discrepancies in the data, namely significant excesses over our SM expectation, we would like to have a means of characterizing the discrepancies. To this end, we divide the full search region into 174 independent search regions, defined by the following intervals in four variables:

- N_{jet}: 2, 3$-$4, 5$-$6, 7$-$8, $\geq$9;
- $N_{b\text{-jet}}$: 0, 1, 2, $\geq$3;
- H_T^{miss} and H_T: a total of 10 orthogonal 2D-intervals, listed in Table 7.2 and illustrated in Figure 7.3.

Note that we exclude search regions in which $H_T < H_T^{\text{miss}}$, as H_T^{miss} should not exceed H_T in a physical event. In addition, for every search interval selected in

N_{jet} and $N_{b\text{-jet}}$, we define a low-H_T^{miss} sideband, $250 < H_T^{\text{miss}} < 300$ GeV with the same H_T boundaries as the bins with $300 < H_T^{\text{miss}} < 350$ GeV. This sideband is used to measuring the QCD background (see Chapter 8.4).

For $N_{\text{jet}} = 2$, only bins with $N_{b\text{-jet}} = 0, 1, 2$ exist. For $N_{\text{jet}} \geq 7$, $H_T - H_T^{\text{miss}}$ bins C1, 1, and 4 are dropped due to low population and low expected signal sensitivity. The total number of independent search bins is thus $1 \times 3 \times 10 + 2 \times 4 \times 10 + 2 \times 4 \times 8 = 174$ and the total number of sideband bins is $1 \times 3 \times 3 + 2 \times 4 \times 3 + 2 \times 4 \times 2 = 49$.

The binning in N_{jet} and $N_{b\text{-jet}}$ is illustrated in Figure 7.2. The decay chains for several gluino and squark SMS models are written in the bins with the highest expected number of signal events for each model. The binning in these two variables is complimentary; generally, the models considered are concentrated in different bins. Should we observe an excess of events in the data, the bins in which the excess does and does not appear could provide useful information for characterizing a potential source of new physics.

This fine search binning also provides additional discrimination between signal and background, as the size and composition of the SM background varies greatly across the search regions.

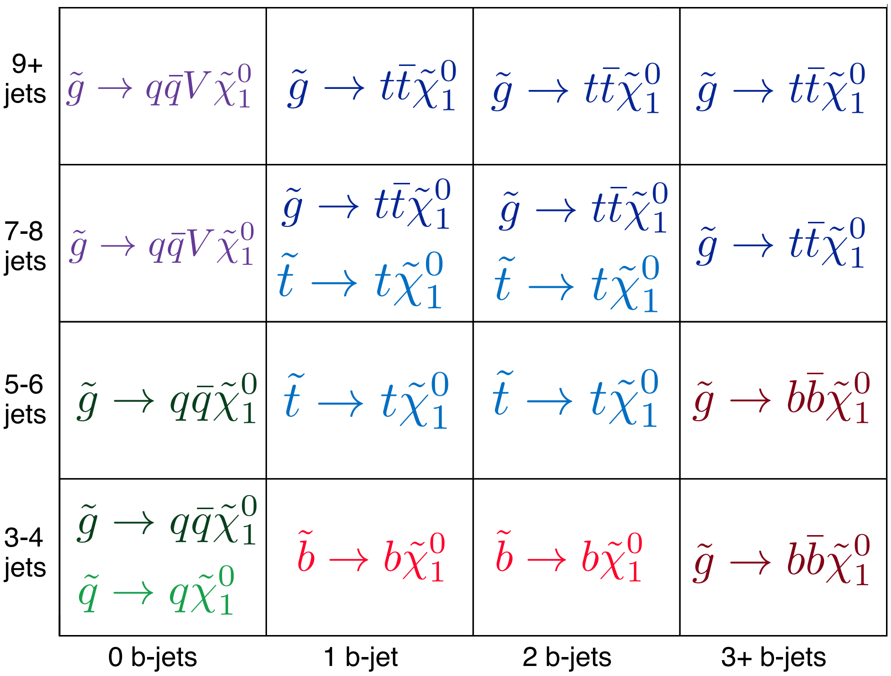

	0 b-jets	1 b-jet	2 b-jets	3+ b-jets
9+ jets	$\tilde{g} \rightarrow q\bar{q}V\tilde{\chi}_1^0$	$\tilde{g} \rightarrow t\bar{t}\tilde{\chi}_1^0$	$\tilde{g} \rightarrow t\bar{t}\tilde{\chi}_1^0$	$\tilde{g} \rightarrow t\bar{t}\tilde{\chi}_1^0$
7-8 jets	$\tilde{g} \rightarrow q\bar{q}V\tilde{\chi}_1^0$	$\tilde{g} \rightarrow t\bar{t}\tilde{\chi}_1^0$ $\tilde{t} \rightarrow t\tilde{\chi}_1^0$	$\tilde{g} \rightarrow t\bar{t}\tilde{\chi}_1^0$ $\tilde{t} \rightarrow t\tilde{\chi}_1^0$	$\tilde{g} \rightarrow t\bar{t}\tilde{\chi}_1^0$
5-6 jets	$\tilde{g} \rightarrow q\bar{q}\tilde{\chi}_1^0$	$\tilde{t} \rightarrow t\tilde{\chi}_1^0$	$\tilde{t} \rightarrow t\tilde{\chi}_1^0$	$\tilde{g} \rightarrow b\bar{b}\tilde{\chi}_1^0$
3-4 jets	$\tilde{g} \rightarrow q\bar{q}\tilde{\chi}_1^0$ $\tilde{q} \rightarrow q\tilde{\chi}_1^0$	$\tilde{b} \rightarrow b\tilde{\chi}_1^0$	$\tilde{b} \rightarrow b\tilde{\chi}_1^0$	$\tilde{g} \rightarrow b\bar{b}\tilde{\chi}_1^0$

Figure 7.2: Two-dimensional plane in N_{jet} and $N_{b\text{-jet}}$ showing the bins with the highest expected number of signal events for several SMS models.

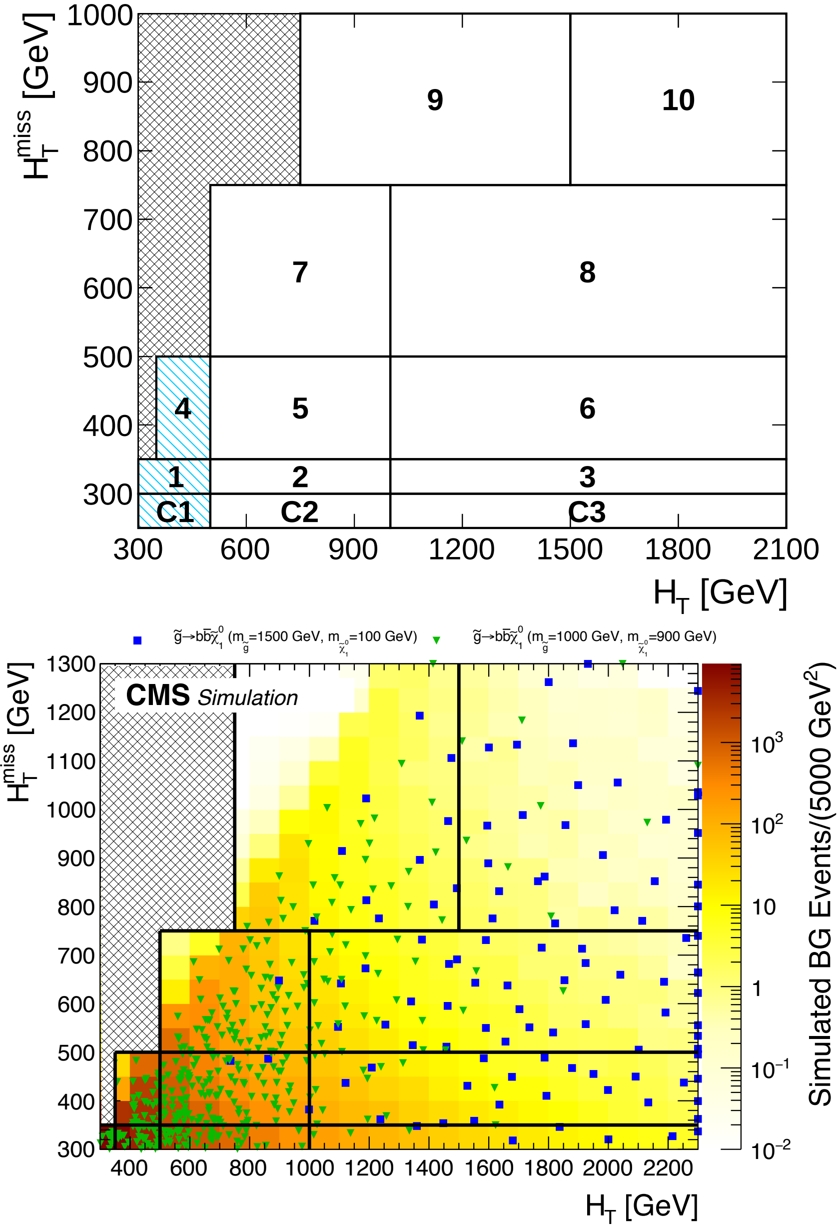

Figure 7.3: Top: two-dimensional plane in H_T and H_T^{miss} showing the signal bins and the QCD sideband bins. The same H_T and H_T^{miss} regions are used for each N_{jet} and $N_{b\text{-jet}}$ bin, except for the bins with teal shading, which are excluded for $N_{\text{jet}} \geq 7$. Bottom: the expected distribution of events in this binning from the total SM background (z-axis), and two T1bbbb model points (scatter). These distributions are taken from simulation.

7.3.2 Aggregate search regions

In addition to the 174 distinct search regions described above, we also prepare and present full results in 12 aggregate regions, determined by summing the results from the nominal search regions while accounting for correlations between regions. The aggregate regions, which are not orthogonal are each intended to represent a simple, one-bin search for an interesting signal topology. While the aggregate regions do not provide as much sensitivity to the presence of many of our target signal models as the full set of search regions, they allow the data to be used in a simpler manner for for investigating other signal scenarios not examined in this thesis. The aggregate regions, and the signal topologies they are intended to help probe, are specified in Table 7.3. The aggregate regions are characterized by their heavy flavor (top or bottom quark) content, parton (or jet) multiplicity, and the mass difference Δm (or available kinematic phase space) between the strongly produced particles and weak decay products. Aggregate regions specifically 11 and 12 target models with direct top squark production.

Table 7.3: Definition of the aggregate search regions. Note that the cross-hatched regions in Fig. 7.3, corresponding to large H_T^{miss} relative to H_T, are excluded from the definition of the aggregate regions.

Region	N_{jet}	$N_{b\text{-jet}}$	H_T [GeV]	H_T^{miss} [GeV]	Parton multiplicity	Heavy flavor ?	Δm
1	≥2	0	≥500	≥500	Low	No	Small
2	≥3	0	≥1500	≥750	Low	No	Large
3	≥5	0	≥500	≥500	Medium	No	Small
4	≥5	0	≥1500	≥750	Medium	No	Large
5	≥9	0	≥1500	≥750	High	No	All
6	≥2	≥2	≥500	≥500	Low	Yes	Small
7	≥3	≥1	≥750	≥750	Low	Yes	Large
8	≥5	≥3	≥500	≥500	Medium	Yes	Small
9	≥5	≥2	≥1500	≥750	Medium	Yes	Large
10	≥9	≥3	≥750	≥750	High	Yes	All
11	≥7	≥1	≥300	≥300	Medium high	Yes	Small
12	≥5	≥1	≥750	≥750	Medium	Yes	Large

Chapter 8

Estimation of SM backgrounds

Following the event selection described in Section 7.2, in the bulk of the search region the dominant background is the production of SM Z bosons in association with jets. The Z boson decays to neutrinos 20% of the time [102], yielding a jets + H_T^{miss} final state that is virtually indistinguishable from that of many of our target SUSY models. Leptonically-decaying $W^{\pm}$ bosons and top quarks produced in association with jets contribute a significant background as well, particularly in the bins with higher multiplicities of jets and b-jets. QCD multijet events with a fake-H_T^{miss} signature from mis-measured jet momenta contribute a smaller background, mostly in bins with lower H_T^{miss}. The background composition, as determined in simulation, in select search regions is shown in Figure 8.1.

As the cross sections for these backgrounds generally exceed those of our target SUSY models by multiple orders of magnitude, many of the search regions of highest signal sensitivity lie on extreme tails of the kinematic distributions of our search variables (Figure 8.3). These distributions are difficult to model in simulation, so we model them using dedicated techniques and control regions (CRs) in data for each background process. The CRs are designed to capture the kinematic shapes of the backgrounds in the search region. Any residual differences between the backgrounds in the search and control regions is corrected for using translation factors derived in simulation. These translation factors are generally functions of physical quantities that are known in the standard model to small uncertainties (e.g., the relative branching ratios of Z bosons to neutrinos and charged leptons) or other observables that can be validated directly in data (e.g., lepton efficiencies). These CRs and background estimation techniques were developed during Run I [103, 104] and have been improved for Run II to robustly measure backgrounds in search regions of more extreme kinematics.

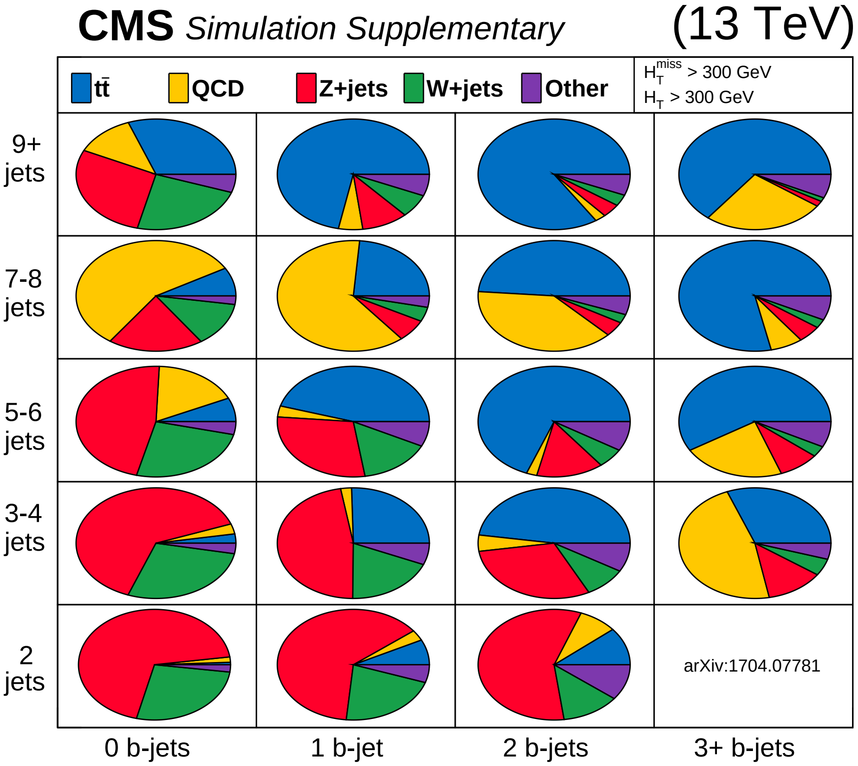

Figure 8.1: Background composition in the N_{jet} versus $N_{b\text{-jet}}$ plane, integrating over all bins of H_T^{miss} and H_T. Bottom: background composition in the N_{jet} versus $N_{b\text{-jet}}$ plane in events with $300 < H_T^{\text{miss}} < 350$ GeV (left), events with $350 < H_T^{\text{miss}} < 500$ GeV(middle), and events with $H_T^{\text{miss}} > 500$ GeV (right). The expected contribution from each process is obtained from simulation after applying the full baseline selection described in Section 7.2.

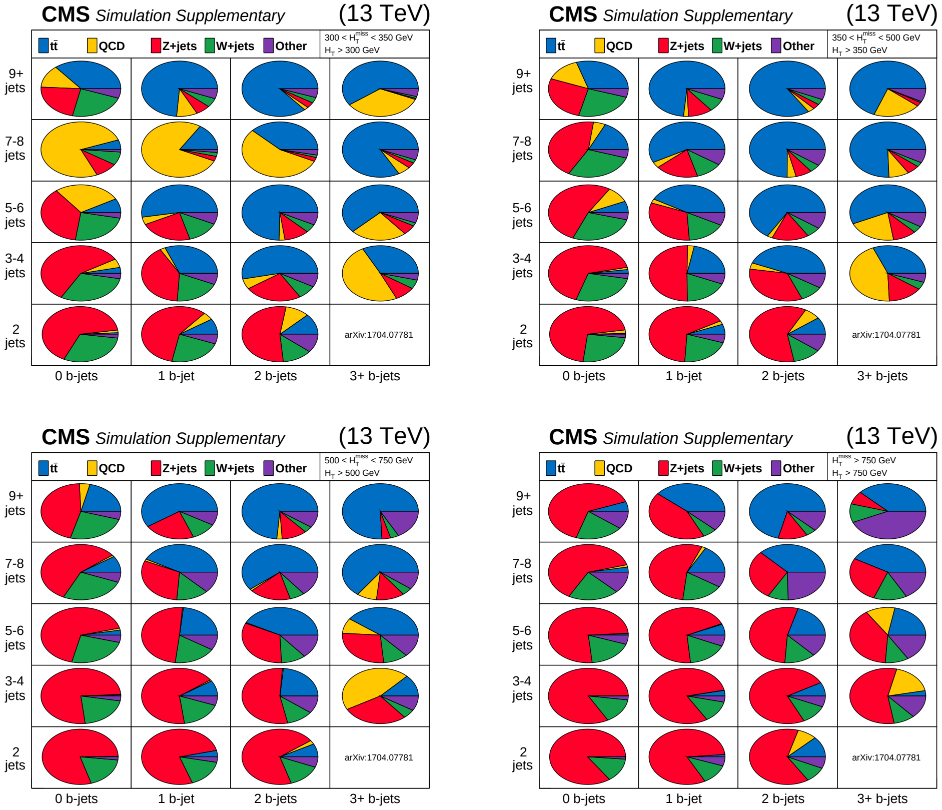

Figure 8.2: Background composition in the N_{jet} versus $N_{b\text{-jet}}$ plane in events with $300 < H_T^{\text{miss}} < 350$ GeV (top-left), events with $350 < H_T^{\text{miss}} < 500$ GeV(top-right), events with $500 < H_T^{\text{miss}} < 750$ GeV (bottom-left), and events with $H_T^{\text{miss}} > 750$ GeV (bottom-right). The expected contribution from each process is obtained from simulation after applying the full baseline selection described in Section 7.2.

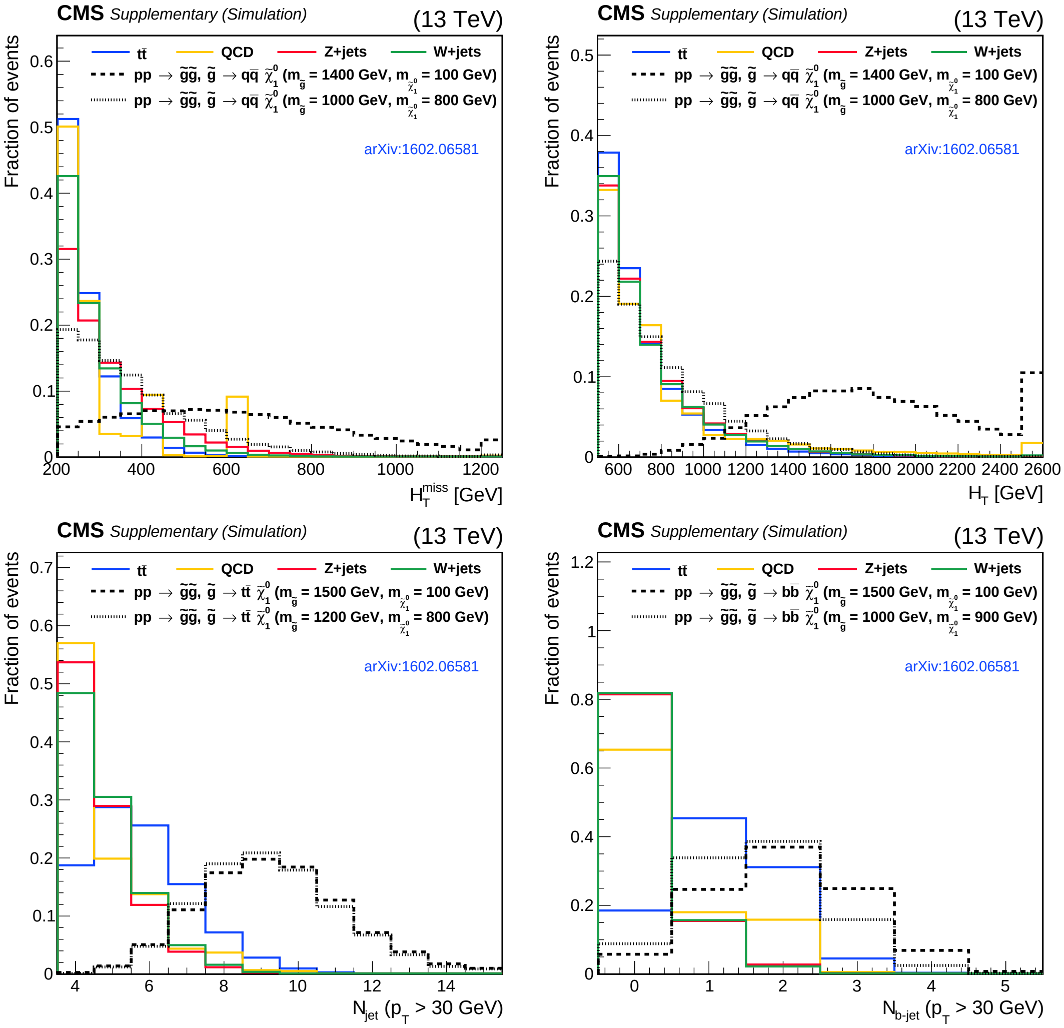

Figure 8.3: Kinematic shape comparisons showing distributions of H_T^{miss} (top left), H_T (top right), the number of jets (bottom left), and the number of b-tagged jets (bottom right) for the main background processes and six example gluino production signal models. The full baseline selection is applied in each plot.

8.1 $Z \to \nu\bar{\nu}$ +jets

Estimating the expected background from SM Z bosons decaying to neutrinos is a classic problem in SUSY and dark matter searches. At previous hadron collider experiments, this background was estimated using control samples of $Z \to \ell^+\ell^-$ events, where $\ell = e$ and/or μ [105, 106, 107]. This control region allows for an almost completely data-driven background measurement, since the control region process is governed by the same production and decay kinematics as the background in the signal region. The main disadvantage of this control region is that it provides limited statistical precision, due mainly to the low branching ratio of Z bosons to charged leptons [102],

$$\frac{\Gamma(Z \to e^+e^-) + \Gamma(Z \to \mu^+\mu^-)}{\Gamma(Z \to \nu\bar{\nu})} = 0.336 \tag{8.32}$$

Some of the first SUSY searches performed on $\sqrt{s} = 7$ TeV LHC data debuted alternative methods for estimating this background using control samples of single isolated γ+jets events [108, 109, 110]. These methods take advantage of higher γ+jets production cross sections while relying on similarities between photon and Z boson kinematics at high-p_T. In this analysis, a γ+jets sample is used to directly estimate the $Z \to \nu\bar{\nu}$ background in bins with $N_{b\text{-jet}} = 0$, while a $Z \to \ell^+\ell^-$ sample is used to validate the background estimation from photon events in bins with $N_{b\text{-jet}} = 0$ and to extrapolate the prediction to the bins with $N_{b\text{-jet}} > 0$.

8.1.1 Control region

A control sample of events with a single isolated photon is selected using a trigger that requires a photon candidate with $p_T > 175$ GeV. Offline, that photon candidate is required to have $p_T > 200$ GeV and $|\eta| < 2.4$, excluding the barrel-endcap transition region ($1.442 < |\eta| < 1.566$), and to pass all of the quality criteria described in Section 5.4. To preferentially select for directly produced photons, i.e., those produced through Compton scattering ($qg \rightarrow q\gamma$) or quark-antiquark annihilation ($q\bar{q} \rightarrow g\gamma$), the candidate is also required to pass a p_T- and η-dependent isolation cut.

An orthogonal sample of dilepton events is also selected using a set of triggers that requires either

- at least one isolated electron or muon with $p_T > 15$ GeV, and either $H_T >$ 350 or 400 GeV depending on the LHC instantaneous luminosity,
- at least one electron with either $p_T >$ 105 or 115 GeV depending on the instantaneous luminosity,
- at least one muon with $p_T > 50$ GeV, or
- at least one isolated electron (muon) with $p_T >$ 27 (24) GeV.

Offline, the events are required to contain exactly one e^+e^- or one $\mu^+\mu^-$ pair with an invariant mass within 15 GeV of the nominal Z boson mass, with the lepton candidates satisfying the same criteria for isolated electrons and muons described in Sections 5.2–5.3. The combined efficiency of the triggers with respect to the offline selection is presented in Table 8.1.

Sample	$\epsilon_{\mathrm{TRIG}} \oplus \mathrm{STAT} \oplus \mathrm{SYST}$	
	$300 < H_T < 1000$ GeV	$H_T > 1000$ GeV
e^+e^-	$98.5^{+0.2+1.0}_{-0.3-1.5}\%$	$94.3^{+0.8+2.0}_{-1.0-2.0}\%$
$\mu^+\mu^-$	$99.3^{+0.1+0.5}_{-0.1-1.0}\%$	

Table 8.1: Combined efficiency of the triggers used to select the dilepton control samples.

In both control samples, the visible p_T of the selected objects (either the γ of the $\ell^+\ell^-$ system) is subtracted from the event to emulate missing momentum and mimic the detector's response to an invisibly decaying Z boson. All jet-based quantities, including N_{jet}, H_T, and H_T^{miss}, are recomputed from the modified events, and a set of control bins with selection mirroring that of the search bins, up to selection in $N_{b\text{-jet}}$ (see below), is constructed.

8.1.2 Translation factor

True direct photon events comprise around 85% of the control sample. The other events contain either a fragmentation photon, i.e., emitted through initial- or final-state radiation or during hadronization, or a non-prompt photon, i.e., from an unstable hadron's decay. These other photons are considered a background to the control sample because their production and kinematics do not mimic those of the target $Z \to \nu\bar{\nu}$ background. Their contributions, which must be accounted for in the prediction are estimated in both data and simulation. The purity of the sample, or the fraction of events with a prompt (direct or fragmentation) photon, β_γ is determined from a fit to the photon isolation variable. The fraction of these events with a direct photon, $\mathcal{F}_{\text{dir}}^{\text{sim}}$, is evaluated in simulation. Additionally, a small difference in photon reconstruction efficiency is observed between simulation and data. This difference is described by a collection of H_T^{miss}-dependent factors, $\mathcal{C}_{\text{data/sim}}^{\gamma}$.

The estimated number of $Z \to \nu\bar{\nu}$ background events contributing to each $N_{b\text{-jet}} = 0$ search region is given by:

$$N_{Z\to\nu\bar{\nu}}^{\text{pred}}\Big|_{N_{b\text{-jet}}=0} = \rho \mathcal{R}_{Z\to\nu\bar{\nu}/\gamma}^{\text{sim}} \mathcal{F}_{\text{dir}}^{\text{sim}} \beta_\gamma N_\gamma^{\text{obs}} \,/\, \mathcal{C}_{\text{data/sim}}^{\gamma}, \tag{8.33}$$

where N_γ^{obs} is the number of events observed in the corresponding N_{jet}, H_T, H_T^{miss}, and $N_{b\text{-jet}} = 0$ bin of the γ+jets control sample, $\mathcal{R}_{Z\to\nu\bar{\nu}/\gamma}^{\text{sim}}$ is the ratio of the number $Z \to \nu\bar{\nu}$ events to the number of direct-γ events in that bin, and β_γ, $\mathcal{F}_{\text{dir}}^{\text{sim}}$, and $\mathcal{C}_{\text{data/sim}}^{\gamma}$ are as described above. The ratio $\mathcal{R}_{Z\to\nu\bar{\nu}/\gamma}^{\text{sim}}$ is determined from simulated samples of $Z \to \nu\bar{\nu}$ and direct-γ events and is shown in Figure 8.4. Note that this ratio takes into account and corrects for any photon events that are lost because the photons are out of kinematic or geometric detector acceptance.

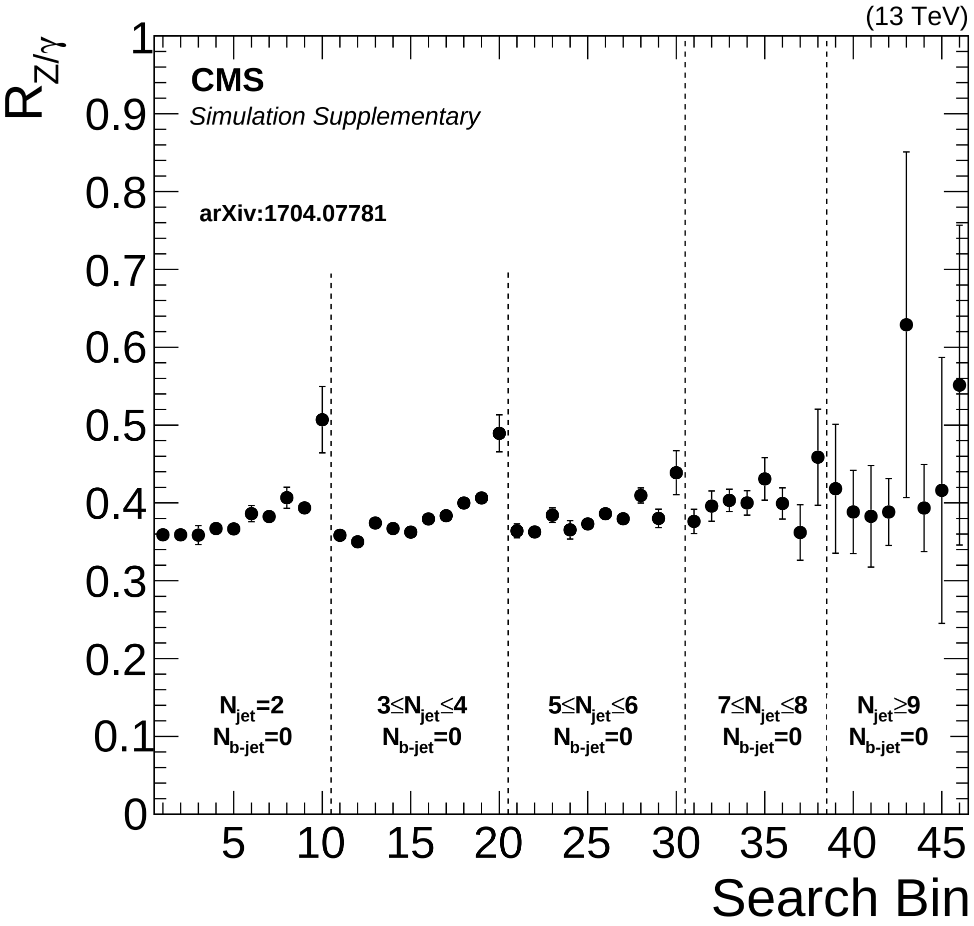

Figure 8.4: Distribution of $\mathcal{R}^{\text{sim}}_{Z\to\nu\bar{\nu}/\gamma}$ after baseline selection in the 46 search bins with $N_{\text{b-jet}} = 0$. Points with error bars show the computed value in each bin with statistical uncertainties from the simulated samples.

To protect against potential differences between simulation and data in the $\mathcal{R}_{Z\to\nu\bar{\nu}/\gamma}$ ratio, including those that might not be accounted for in the leading order γ+jets sample, one final multiplicative correction is introduced:

$$\rho = \frac{\left\langle \mathcal{R}^{\mathrm{obs}}_{Z\to\ell^+\ell^-/\gamma} \right\rangle}{\left\langle \mathcal{R}^{\mathrm{sim}}_{Z\to\ell^+\ell^-/\gamma} \right\rangle} = \frac{\sum N^{\mathrm{obs}}_{Z\to\ell^+\ell^-}}{\sum N^{\mathrm{sim}}_{Z\to\ell^+\ell^-}} \cdot \frac{\sum N^{\mathrm{sim}}_{\gamma}}{\sum N^{\mathrm{obs}}_{\gamma}} \cdot \frac{\left\langle \beta^{\mathrm{data}}_{\ell\ell} \right\rangle}{\left\langle \mathcal{C}^{\ell\ell}_{\mathrm{data/sim}} \right\rangle} \cdot \frac{\left\langle \mathcal{C}^{\gamma}_{\mathrm{data/sim}} \right\rangle}{\left\langle \mathcal{F}^{\mathrm{sim}}_{\mathrm{dir}} \beta_{\gamma} \right\rangle}, \tag{8.34}$$

where $N^{\mathrm{obs}}_{Z\to\ell^+\ell^-}$, $N^{\mathrm{sim}}_{Z\to\ell^+\ell^-}$, and $N^{\mathrm{sim}}_{\gamma}$ are the numbers of events in the indicated control regions, with the simulated samples normalized to the integrated luminosity of the data. The $\beta^{\mathrm{data}}_{\ell\ell}$ factors represent the fraction of true $Z \to \ell^+\ell^-$ events in the dilepton control sample and are obtained from fits to the measured $m_{\ell\ell}$ distributions (see Figure 8.5). As in the case of the photon samples, additional corrections, $\mathcal{C}^{\ell\ell}_{\mathrm{data/sim}}$, are applied to account for differences in lepton reconstruction efficiencies between simulation and data.

The dilepton sample lacks sufficient statistics for a precise measurement of ρ in several search bins, so we examine the projections of ρ along each search variable's distribution in Figure 8.6. The double ratio shows a modest dependence on H_T and N_{jet}, so we bin this factor in H_T:

$$\rho(H_T) = 0.91 + \left(9.6 \times 10^{-5}\ \mathrm{GeV}^{-1}\right) \min\left(H_T,\ 900\ \mathrm{GeV}\right) \tag{8.35}$$

The background estimation for bins with $N_{b\text{-jet}} > 0$ is determined by scaling the estimated background in $N_{b\text{-jet}} = 0$ bins by additional translation factors

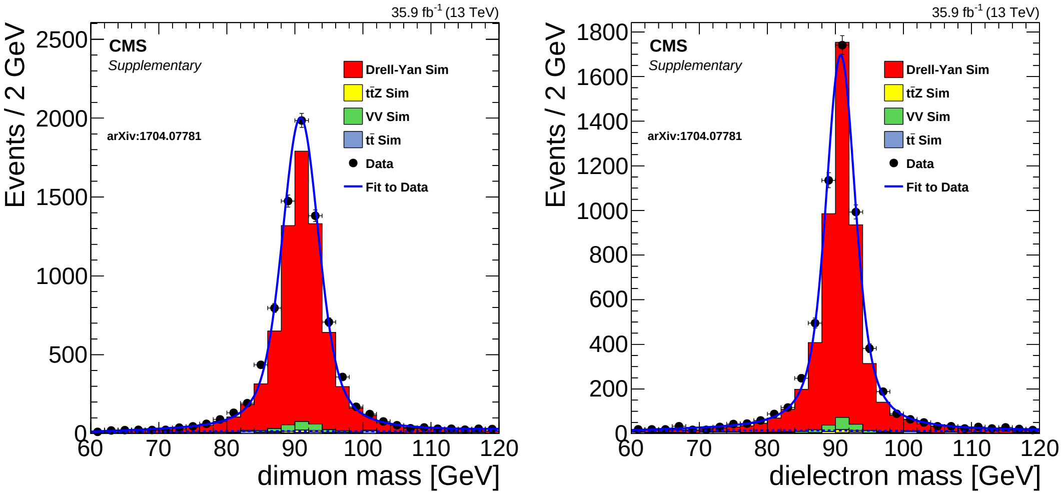

Figure 8.5: The dimuon (left) and dielectron (right) invariant mass distributions in the dilepton control regions. The fit shapes are obtained from a data sample with only the baseline selection applied. These shapes are then fixed and fit to a selection in $N_{b\text{-jet}}$ to extract the purity. For comparison, we show the colored histograms representing the Drell-Yan (red), $t\bar{t}Z$ (yellow), diboson (green), and $t\bar{t}$ (blue) contributions, determined from simulated samples scaled to 35.9 fb^{-1}.

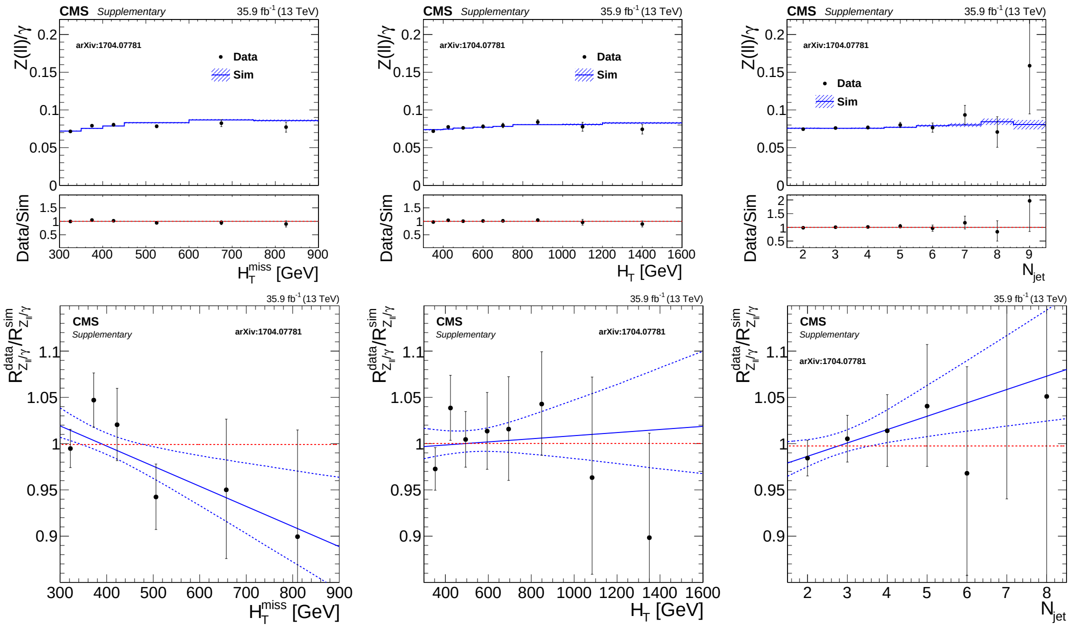

Figure 8.6: Above, from left-to-right: $\mathcal{R}_{Z\rightarrow\ell^+\ell^-/\gamma}$ ratio as a function of H_T^{miss}, H_T, and N_{jet} after baseline selection in data (black) and simulation (blue). The ratio transfer factor is computed using simulated events and we check in one dimensional projections that data agree with simulation. Below, from left-to-right: zoomed-in view of the double ratio ρ ratio as a function of H_T^{miss}, H_T, and N_{jet}. The solid blue line shows the straight-line fit, with the uncertainties propagated as blue dashed lines.

determined in the dilepton control sample:

$$\left(N^{\text{pred}}_{Z\rightarrow\nu\bar{\nu}}\right)_{j,b,k} = \left(N^{\text{pred}}_{Z\rightarrow\nu\bar{\nu}}\right)_{j,0,k}\mathcal{F}_{j,b} \tag{8.36}$$

In the above expression, j, b, and k are bin indices (numbered from zero) for the N_{jet}, $N_{b\text{-jet}}$, and kinematic (i.e., H_T and H_T^{miss}) variables, respectively. For example, $j = 0$ corresponds to $N_{\text{jet}} = 2$, $b = 1$ to $N_{b\text{-jet}} = 1$, and $k = 9$ to kinematic interval 10 in Table 7.2 and Fig. 7.3.

For all bins with $N_{\text{jet}} < 9$ bin, corresponding to $j < 4$, the extrapolation factor $\mathcal{F}_{j,b}$ is obtained from a fit to the observed number of events in each $Z \rightarrow \ell^+\ell^-$ control bin:

$$\mathcal{F}_{j,b} = \left(N^{\text{data}}_{Z\rightarrow\ell^+\ell^-}\beta^{\text{data}}_{\ell\ell}\right)_{j,b} \Big/ \left(N^{\text{data}}_{Z\rightarrow\ell^+\ell^-}\beta^{\text{data}}_{\ell\ell}\right)_{j,0}, \tag{8.37}$$

where $j = 0, 1, 2, 3$ and $\beta^{\text{data}}_{\ell\ell}$ is a data-derived correction for the $N_{b\text{-jet}}$-dependent purity (i.e., $Z \rightarrow \ell^+\ell^-$ vs. $t\bar{t}$, etc). Note that the simulated samples used to compute the ratio include rare processes, such as $t\bar{t}Z$, which can contribute significantly to this background in the bins with the highest N_{jet} and $N_{b\text{-jet}}$ selection.

For the statistics-limited $N_{\text{jet}} \geq 9$ bins, we use the data-derived factor for $N_{\text{jet}} = 7{-}8$ ($j = 3$) multiplied by an additional $N_{b\text{-jet}}$ extrapolation factor obtained from simulation:

$$\mathcal{F}_{4,b} = \mathcal{F}_{3,b}\left(\mathcal{F}^{\text{sim}}_{4,b}/\mathcal{F}^{\text{sim}}_{3,b}\right). \tag{8.38}$$

8.1.3 Systematic uncertainties

A closure test of this extrapolation in $N_{b\text{-jet}}$ is performed on a simulated sample of $Z \rightarrow \nu\bar{\nu}$ events, as illustrated in Figure 8.7. The expected number of $Z \rightarrow \nu\bar{\nu}$ events in $N_{b\text{-jet}} = 0$ bins is scaled by translation factors derived from simulated samples of $Z \rightarrow \ell^+\ell^-$ events and the result is compared to the expected numbers of $Z \rightarrow \nu\bar{\nu}$ in each $N_{b\text{-jet}} > 0$ bin obtained directly from simulation. From this test, we extract a systematic uncertainty on the extrapolation in $N_{b\text{-jet}}$ of 7, 10, and 20% for $N_{b\text{-jet}} = 1$, 2, and $\geq$3, respectively. This uncertainty accounts for the assumption that the $\mathcal{F}_{j,b}$ terms are independent of H_T and H_T^{miss}.

We assign an additional uncertainty on the simulation-derived ratio $\mathcal{F}_{4,b}^{\text{sim}}/\mathcal{F}_{3,b}^{\text{sim}}$ from Equation (8.38) of 7 to 40%, depending on $N_{b\text{-jet}}$. The lower bound on this uncertainty is equal to 1.0 and the upper bound is determined using a binomial model described in Ref. [111]. We also apply a flat uncertainty of $\sim 50\%$, based on measurements performed in Ref. [112], on the contribution of rare processes to this ratio.

A variety of sources of small uncertainty, including the purity of the photon sample and the statistical precision of the MC simulation are also taken into account and summarized in 8.2. The largest uncertainty on this background prediction arises from low statistics in the control bins, especially the dilepton bins used to measure the double ratio.

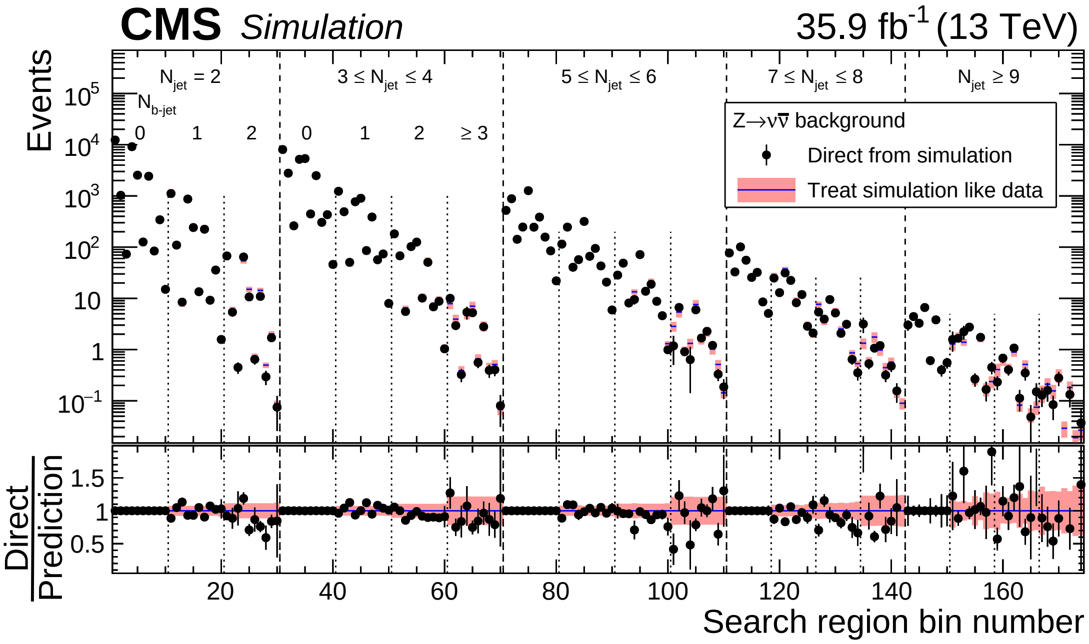

Figure 8.7: Closure test of the $Z \to \nu\bar{\nu}$ background estimation method performed on MC. The black points show the background as determined directly from Z+jets and $t\bar{t}Z$ MC and the histograms show the background measured by scaling the expected number of $Z \to \nu\bar{\nu}$ events in $N_{b\text{-jet}} = 0$ bins by translation factors derived from simulated samples of $Z \to \ell^+\ell^-$ events. The shaded uncertainty bands include both the systematic uncertainty associated with the dependence of $\mathcal{F}_{j,b}$ on the kinematic parameters H_T and H_T^{miss} and the statistical uncertainty of the simulated sample. For bins corresponding to $N_{b\text{-jet}} = 0$, the agreement is exact by construction.

Source	Approx Uncert. (%)	Correlation assumptions
γ CR stats	1–13	Corr. across $N_{b\text{-jet}}$
γ purity (β_γ)	0.4–1.4	Fully-corr. across bins
γ fragmentation factor ($\mathcal{F}_{\text{dir}}^{\text{sim}}$)	0.1–6	Uncorr. across bins
γ trigger efficiency	0.0–0.3	Corr. across H_T, N_{jet}, $N_{b\text{-jet}}$
γ ID/ISO SF	0	Uncorr. across bins
$Z \to \ell^+\ell^-$ ($N_{b\text{-jet}}$ =0) purity	0.8	Fully-corr. across bins
$Z \to \ell^+\ell^-$ trigger efficiency	0.4	Fully-corr. across bins
$Z \to \ell^+\ell^-$ ID/ISO SF	5	Fully-corr. across bins
MC closure	2-30	Uncorr. across bins
$< \rho >$	1.8	Fully-corr. across bins
$\rho(H_T^{\text{miss}}, H_T, N_{\text{jet}})$	1-12	Corr. across $N_{b\text{-jet}}$
$Z \to \ell^+\ell^-$ CR stats	5-50	Corr. across H_T^{miss} and H_T, also two highest N_{jet} intervals for $N_{b\text{-jet}} > 0$
$\mathcal{F}_{4,b}^{\text{sim}}/\mathcal{F}_{3,b}^{\text{sim}}$	10-40	Corr. across H_T^{miss} and H_T, also two highest N_{jet} intervals for $N_{b\text{-jet}} > 0$

Table 8.2: Summary of the sources of systematic uncertainty on the $Z \to \nu\bar{\nu}$ background estimation. For each systematic, an approximate range of values of the corresponding uncertainty us provided, along with the correlation structure of the systematic component across search bins.

8.2 Top quark and W+jets: lost lepton

Processes producing $W^\pm$ bosons that decay to a charged lepton and a neutrino, most notably W+jets and $t\bar{t}$ +jets production, can enter the zero-lepton search region if the lepton is an electron or muon that escapes the lepton and leptonic track vetoes, here called “lost lepton,” or if it is a tau that decays hadronically and escapes the hadronic track veto. The method used to estimate the former category of background events is described in Section 8.2. In Section 8.3, we detail the method used to estimate the latter. As the two methods partially share a data control sample and employ similar MC information to estimate control-to-search region translation factors, there are significant correlations between the uncertainties associated with each method. The treatment of these correlations is described in Section 8.3.3.

8.2.1 Control region

A sample enriched in the processes producing leptonically-decaying $W^{\pm}$ bosons is easily established by inverting the lepton veto requirement; that is, by selecting events with exactly one isolated electron or muon. There is a unique control region for every search region, defined by the same selection on the four search variables. There are several advantages to using this control sample to model the lost lepton background, the most important of which are listed below:

- The shapes of the kinematic distributions of the background processes in this sample are very similar to those in the search regions, as illustrated in Figure 8.8, which compares these shapes in simulation. Any differences in the shapes can be corrected with simulation-derived translation factors (see 8.2.2), but in general, the more similar the shapes, the less we depend on MC to model these distributions.

- The composition of the sample of background processes (i.e. the relative amount of W+jets events to $t\bar{t}$, single-t, etc. events) in this region is very similar to the composition of these backgrounds in the search region. This similarity reduces our dependence on knowledge of the cross sections for complicated production modes of these processes (e.g., $qg \to W + 9$ jets).

- The sample is almost entirely (99+%) free of contamination from multijet processes with misidentified leptons or fake-H_T^{miss}.

No requirement on the number of isolated tracks is applied in this sample. We place an upper bound on the transverse mass of the lepton-E_T^{miss} system, $m_T < 100$ GeV to reduce potential signal contamination from models with leptonic final states (e.g., T1tttt). All other selection applied in the search region is applied in the control sample.

8.2.2 Translation factor

The information needed to translate from an observed number of events in each control region to a background prediction in the corresponding region is essentially the probability of a lepton being correctly identified, or equivalently, of the $W \to \ell\nu$ event landing in the "found" lepton control region. If we define this probability as an efficiency ϵ, the number of events in which such a lepton is found as N_{CR}, the number of events in which such a lepton is lost as N_{CR}, then in simplest terms

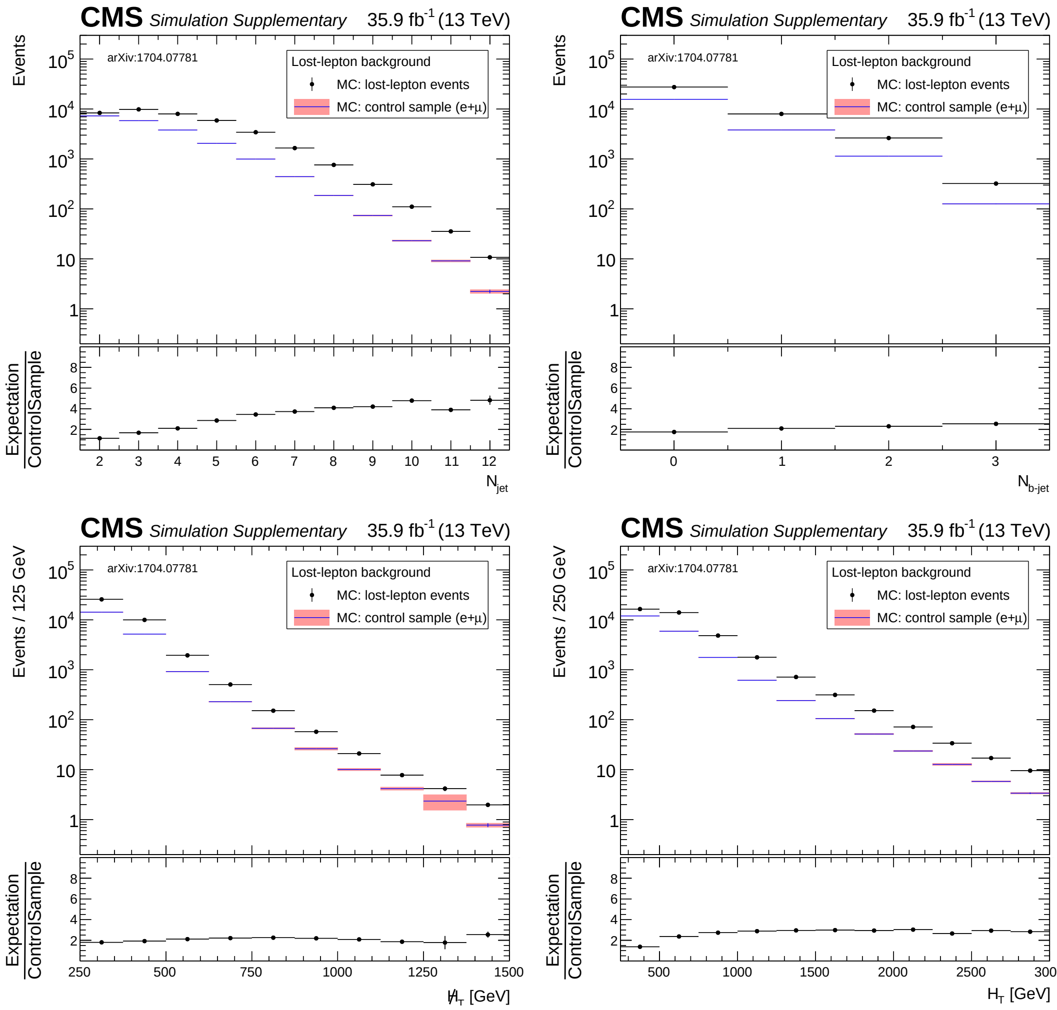

Figure 8.8: Comparison of the number of expected lost lepton background events in the zero (selected) lepton search region (points, with statistical uncertainties) and the sum of single electron and muon control sample events (histograms, with statistical uncertainties) as a function of the four kinematic search variables. The simulated samples include $t\bar{t}$, W+jets, tW, single-t, and rare processes, all normalized to either NLO or NNLO cross sections. Only statistical uncertainties are shown. The lower panel shows the ratio of the expected number of search region to control region events.

$$N_{CR} = N(W \to \ell\nu) \cdot \epsilon$$

$$N_{SR} = N(W \to \ell\nu) \cdot (1 - \epsilon)$$

$$N_{SR} = N_{CR} \cdot \frac{1 - \epsilon}{\epsilon}$$

where $N(W \to \ell\nu) = N(W \to \mu\nu) + N(W \to e\nu)$ is the total number of events with $W^{\pm}$ bosons, specifically those decaying to muons or electrons, that pass all selection other than the lepton requirements (i.e. lost+found). Separating the background into lost muon (μ) and lost electron (e) contributions, then the total lost lepton background is

$$N_{SR}^{\mathrm{LL}} = N_{CR}^{\mu} \cdot \frac{1 - \epsilon_{\mu}}{\epsilon_{\mu}} + N_{CR}^{e} \cdot \frac{1 - \epsilon_{e}}{\epsilon_{e}}$$

where $N_{CR}^{\mu(e)}$ is the number of single-muon (electron) events observed in the control sample and $\epsilon_{\mu(e)}$ is the efficiency for identifying a muon (electron).

To better understand and control the systematic uncertainties associated MC-derived efficiencies, we define the total lepton efficiency as the product of three separate efficiencies:

- $\epsilon_{\mathrm{ACC}}^{\mu(e)}$: the probability that a prompt muon (electron) is within the kinematic and geometric acceptance of the detector and our selection

- $\epsilon^{\mu(e)}_{\text{RECO}}$: the probability that the lepton is fully reconstructed and passes all quality-related selection criteria listed in Sections 5.2 -5.3.
- $\epsilon^{\mu(e)}_{\text{ISO}}$: the probability the that the lepton passes the isolation requirements described in Section 7.2

We define three exclusive categories of lost lepton events from these three efficiencies:

$$N^{\mu(e)}_{\text{ACC}} = N^{\mu(e)}_{CR} \cdot \frac{1}{\epsilon^{\mu(e)}_{\text{ISO}}} \cdot \frac{1}{\epsilon^{\mu(e)}_{\text{RECO}}} \cdot \frac{1 - \epsilon^{\mu(e)}_{\text{ACC}}}{\epsilon^{\mu(e)}_{\text{ACC}}} \tag{8.39}$$

which is the number of events with a prompt muon (electron) that is <u>not</u> within the kinematic and geometric acceptance of the detector and our selection,

$$N^{\mu(e)}_{\text{RECO}} = N^{\mu(e)}_{CR} \cdot \frac{1}{\epsilon^{\mu(e)}_{\text{ISO}}} \cdot \frac{1 - \epsilon^{\mu(e)}_{\text{RECO}}}{\epsilon^{\mu(e)}_{\text{RECO}}} \tag{8.40}$$

which is the number of events with a prompt muon (electron) that is in acceptance but is <u>not</u> fully reconstructed or identified, and

$$N^{\mu(e)}_{\text{ISO}} = N^{\mu(e)}_{CR} \cdot \frac{1 - \epsilon^{\mu(e)}_{\text{ISO}}}{\epsilon^{\mu(e)}_{\text{ISO}}} \tag{8.41}$$

which the number of events with a prompt muon (electron) that is in acceptance and is fully reconstructed and identified but does <u>not</u> pass the isolation cut.

In the above expressions, the contribution to the lost lepton background from each flavor is expressed in terms of the number of control region events with a lepton of that same flavor. One interesting feature of this measurement is that by lepton universality, $N(W \to \mu\nu) = N(W \to e\nu)$, so a control sample of single-electron events can provide an additional measurement of the lost-muon background and vice-versa:

$$
\begin{aligned}
N^{\mu}_{SR} &= N(W \to \mu\nu) \cdot (1 - \epsilon_{\mu}) \\
N^{\mu}_{SR} &= N(W \to e\nu) \cdot (1 - \epsilon_{\mu}) \\
N^{\mu}_{SR} &= N^{e}_{CR} \cdot \frac{1 - \epsilon_{\mu}}{\epsilon_{e}}
\end{aligned}
$$

and similarly

$$N^{e}_{SR} = N^{\mu}_{CR} \cdot \frac{1 - \epsilon_{e}}{\epsilon_{\mu}}$$

In terms of the separate categories' efficiencies, we can express these background from each flavor in terms of the opposite flavor's control region yields:

$$
\begin{aligned}
N^{\mu(e)}_{\mathrm{ACC}} &= N^{e(\mu)}_{CR} \cdot \frac{1}{\epsilon^{\mu(e)}_{\mathrm{ISO}}} \cdot \frac{1}{\epsilon^{\mu(e)}_{\mathrm{RECO}}} \cdot \frac{1-\epsilon^{e(\mu)}_{\mathrm{ACC}}}{\epsilon^{\mu(e)}_{\mathrm{ACC}}} \\
N^{\mu(e)}_{\mathrm{RECO}} &= N^{e(\mu)}_{CR} \cdot \frac{1}{\epsilon^{\mu(e)}_{\mathrm{ISO}}} \cdot \frac{1-\epsilon^{e(\mu)}_{\mathrm{RECO}}}{\epsilon^{\mu(e)}_{\mathrm{RECO}}} \cdot \frac{\epsilon^{e(\mu)}_{\mathrm{ACC}}}{\epsilon^{\mu(e)}_{\mathrm{ACC}}} \\
N^{\mu(e)}_{\mathrm{ISO}} &= N^{e(\mu)}_{CR} \cdot \frac{1-\epsilon^{e(\mu)}_{\mathrm{ISO}}}{\epsilon^{\mu(e)}_{\mathrm{ISO}}} \cdot \frac{\epsilon^{e(\mu)}_{\mathrm{RECO}}}{\epsilon^{\mu(e)}_{\mathrm{RECO}}} \cdot \frac{\epsilon^{e(\mu)}_{\mathrm{ACC}}}{\epsilon^{\mu(e)}_{\mathrm{ACC}}}
\end{aligned}
$$

With the lost lepton background expressed in terms of both the same-flavored and opposite-flavored control region yields, we use both the found muon and found electron control samples and their corresponding translation factors to measure each flavor's lost lepton background and take a weighted average of the two measurements.

Each of the above efficiencies is measured directly in a MC sample composed of all of the SM backgrounds passing our kinematic selection, including $t\bar{t}$, W+jets, tW, single-t, and rarer processes. To validate the modeling of ϵ^{RECO} and ϵ^{ISO}, an independent measurement of these efficiencies is performed on both MC and data samples of $Z \to \ell\ell$ events using a tag-and-probe method. No significant difference is observed between the efficiencies measured in the data and MC samples, so no correction is applied to the MC-derived efficiencies used to estimate the lost lepton background.

A small ($< 1\%$) component of the lost lepton background actually originates from events with two prompt leptons, both of which escape veto. This contribution can be calculated using the same single lepton control regions:

$$N^{\ell\ell}_{SR} = (N^{\mu}_{CR} + N^{e}_{CR}) \cdot (1 - f^{CR}_{SL}) \cdot \frac{1 - \epsilon_{\ell\ell}}{\epsilon_{\ell\ell}} \tag{8.42}$$

where $(1 - f^{CR}_{SL})$ is the fraction of true dilepton events in the single lepton control region and $(1 - \epsilon_{\ell\ell})/\epsilon_{\ell\ell}$ is the probability that both leptons are lost. Both of these quantities are obtained from MC.

Three additional correction factors from MC are needed to estimate the full lost lepton background,

- $\epsilon^{\mu(e)}_{m_T}$: the fraction of true single lepton events that pass the transverse mass cut and thus enter the control region ($\sim 90\%$ in most bins);
- f^{e}_{pur}: the fraction of events in the single electron control region with a true prompt electron ($\sim 95\%$, while the single muon sample is assumed to be 100% pure);
- and $\epsilon^{\mu,e}_{\text{tk}}$: the fraction true single lepton events that survive the isolated track veto,

$$\epsilon_{\text{tk}} = \frac{\text{Number of events surviving lepton veto that are rejected by track veto}}{\text{Number of events surviving lepton veto}} . \tag{8.43}$$

> The value of ϵ_{tk} is relatively flat as a function of the search variables, and has an average value of 68% and 60% for the lost-muon and lost-electron backgrounds, respectively.

The efficiencies and other correction factors, as well as their parameterizations and associated systematic uncertainties, are summarized in Table 8.3.

Putting everything together, the total lost lepton background (neglecting the averaging of measurements from same-flavored and opposite-flavored control regions) an be expressed as:

$$N_{SR}^{\text{LL}} = \epsilon_{\text{tk}}^{\mu,e} \cdot \sum_{\ell=\mu,e} \left\{ \frac{[f_{\text{pur}}^{e}]}{\epsilon_{m_T}^{\ell}} \cdot \left[f_{SL}^{CR} \cdot \left(N_{\text{ACC}}^{\ell} + N_{\text{RECO}}^{\ell} + N_{\text{ISO}}^{\ell} \right) + N_{SR}^{\ell\ell} \right] \right\} \tag{8.44}$$

A schematic illustration of the full lost lepton background estimation categories is provided in Figure 8.2.2.

8.2.3 Systematic uncertainties

To validate the parametrization of the lepton efficiencies and other variables in the translation factors, a closure test is performed by running the prediction on MC and comparing that prediction to the result obtained directly the MC. The same MC samples used to calculate the efficiencies are included in this test. The results of this test are presented in Figure 8.2.3 in one-dimensional projections of the search variables and in Figure 8.2.3 in each of the 174 search bins. There

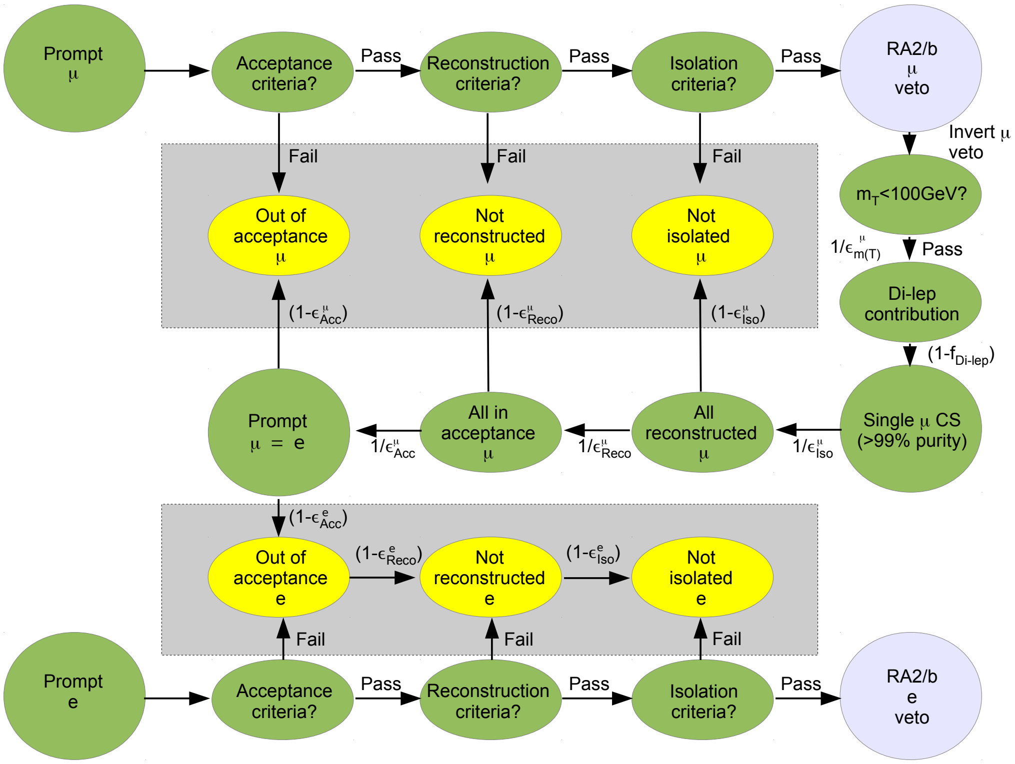

Figure 8.9: Schematic illustration of the three exclusive categories of lost lepton events.

does not appear to be any systematic non-closure across the search bins; any deviation between the direct MC prediction and the yield obtained from running the background estimation method on the MC is attributed to limited statistical prediction. For each bin, an uncertainty equal to the maximum of the deviation between the two MC predictions and statistical uncertainty on that deviation is assigned to the lost lepton prediction obtained from data.

The following sources of systematic uncertainty are also considered. For most systematics, one or more of the parameters taken from simulation is varied within its assumed uncertainty, and that variation is propagated to the final prediction. The statistical uncertainty of the MC simulation used to calculate the parameters is considered in each case. These uncertainties are summarized in Table 8.3.

Lepton isolation efficiency

The muon and electron isolation efficiencies are obtained from MC simulation. To directly validate these efficiencies in data, the efficiencies are calculated using a tag-and-probe method on samples of $Z \rightarrow e^+e^-$ and $Z \rightarrow \mu^+\mu^-$ events. The efficiency measured by tag-and-probe in data and MC are found to agree to high precision ($< 1\%$), so we apply no correction to the MC efficiencies used to estimate the background. We assign a small uncertainty on these efficiencies equal to

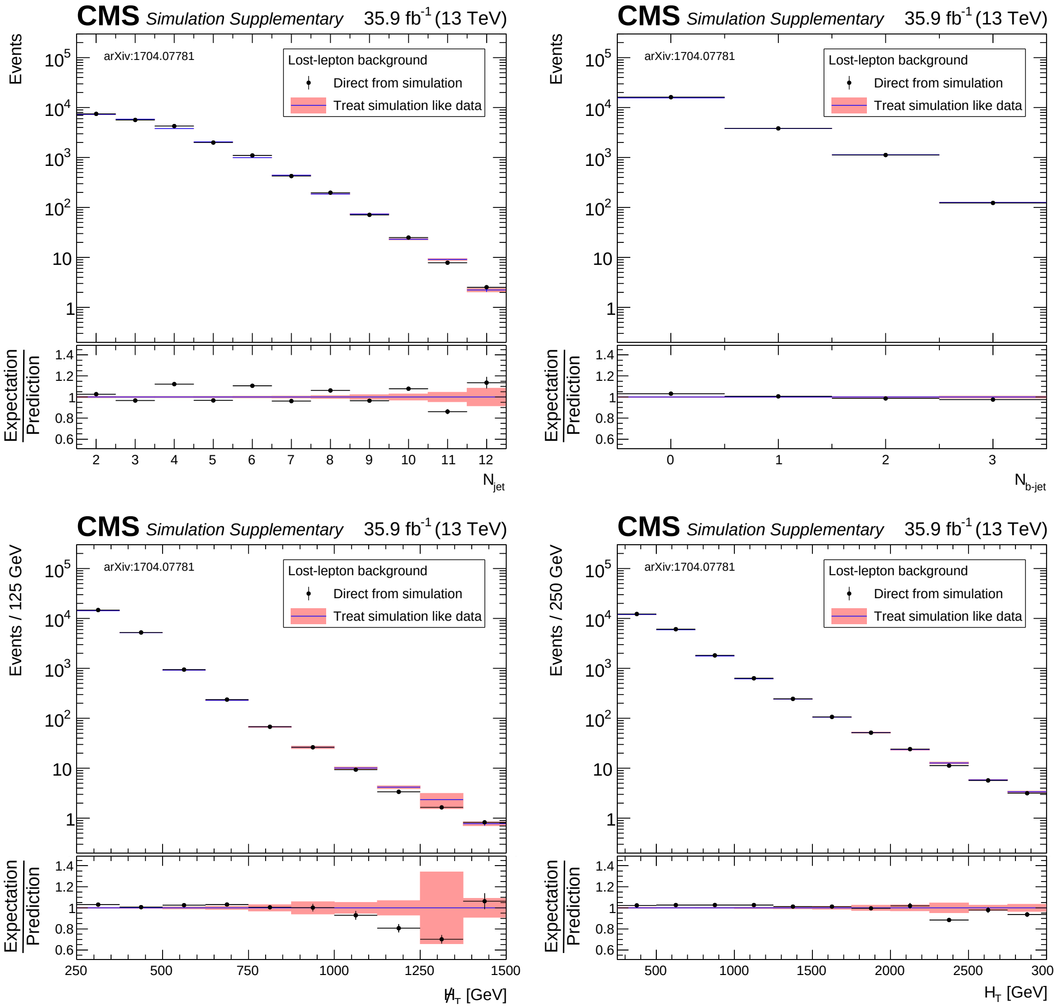

Figure 8.10: Closure test of the lost lepton background estimation method performed on MC, shown as a function of the four kinematic search variables. The black points show the background as determined directly from MC and the histograms show the background predicted by running the prediction on a simulated sample of single lepton events. The MC samples include $t\bar{t}$, W+jets, tW, single-t, and rare processes, all normalized to either NLO or NNLO cross sections. Only statistical uncertainties are shown. The results in the lower panel are obtained through bin-by-bin division of the results in the upper panel, including the uncertainties, by the central values of the "predicted" results.

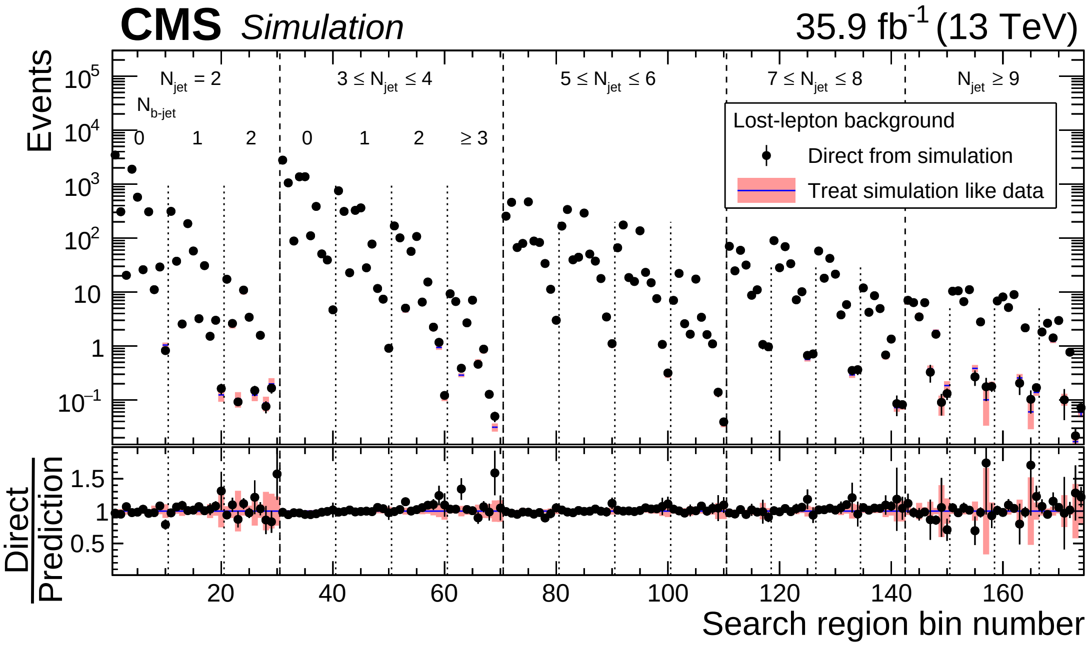

Figure 8.11: Closure test of the lost lepton background estimation method performed on MC. The black points show the background as determined directly from MC and the histograms show the background measured by running the prediction on a simulated sample of single lepton events. The MC samples include $t\bar{t}$, W+jets, tW, single-t, and rare processes, all normalized to either NLO or NNLO cross sections. Only statistical uncertainties are shown. The results in the lower panel are obtained through bin-by-bin division of the results in the upper panel, including the uncertainties, by the central values of the “predicted” results. The 10 results (8 results for $N_{\text{jet}} \geq 7$) within each region delineated by vertical dashed lines correspond sequentially to the 10 (8) kinematic intervals of H_T and H_T^{miss} indicated in Table 7.2 and Fig. 7.3.

the maximum of the fractional difference between the tag-and-probe efficiencies measured in data and MC and the uncertainty on this value.

Lepton reconstruction/ID efficiency

The muon and electron reconstruction and ID efficiencies are also obtained from simulated events. These efficiencies are also validated in data via a tag-and-probe measurement. As in the case of the isolation efficiencies, the tag-and-probe reconstruction and ID efficiencies measured in data and MC agree to high precision, and we assign an uncertainty equal to the maximum of the fractional difference between the tag-and-probe efficiencies measured in data and MC and the uncertainty on this value.

Lepton acceptance

The uncertainty on the lepton acceptance efficiency is determined by varying the PDF sets used to produce the MC samples within their uncertainties. The MC renormalization and factorization scales are also varied using a similar procedure.

Lepton purity

The purity is expected to be very high ($> 99\%$ for muons, $> 95\%$ for electrons) so we only apply a flat conservative uncertainty of 20% on the purity correction.

Dilepton correction

The contributions to the control region and search region from dileptonic processes are small (3% of the control region, 5% of the search region) so we assign a flat conservative uncertainty of 50% on both.

m_T cut efficiency

The momenta of the jets in simulated events are varied within the uncertainties on their energy corrections, and these variations are propagated to the reconstructed E_T^{miss} and m_T. The efficiency of the m_T is then recalculated.

Isolated track vetoes

The isolated-track vetoes reduce the expected lost lepton background by 30-40% in each search bin. An independent tag-and-probe study is performed to measure the efficiency of the charged track isolation cut used to define leptonic tracks in data and in MC. The efficiencies measured in data and MC are found to agree at percent level precision for most ranges of track p_T and η (Figure 8.12). To translate the track-by-track isolation efficiency uncertainties reported in Figure 8.12 to search-bin-by-search-bin uncertainties on the overall reduction of the lost lepton background due to the track veto ($\epsilon_{\text{tk}}^{\mu,e}$), we multiply the fraction of isolated tracks (passing isolation cut) in each $p_T - \eta$ bin in Figure 8.12 by the maximum of the deviation from one of the data/MC efficiency ratio and the statistical uncertainty on that ratio in that same $p_T - \eta$ bin and sum this product over all $p_T - \eta$ bins.

This procedure is performed for each of the 174 search bins, yielding an overall uncertainty on $\epsilon^{\mu,e}_{\text{tk}}$ of:

$$\delta(\epsilon^{\mu,e}_{\text{tk}}) = \sum_{\substack{i=p_T-\text{bin}\\ j=\eta-\text{bin}}} f^{\mu,e}_{ij} \cdot \delta^{(}\epsilon^{\mu,e}_{\text{ISO}})_{ij} \tag{8.45}$$

where, for a given search bin, $f^{\mu,e}_{ij}$ is the fraction of rejected events with a lepton in $p_T - \eta$ bin (i, j) and $\delta^{(}\epsilon^{\mu,e}_{\text{ISO}})_{ij}$ is the maximum of the deviation from one of the data/MC efficiency ratio and the statistical uncertainty in that $p_T - \eta$ bin.

This uncertainty varies most strongly as a function of N_{jet}, so we have parametrized it in five bins of N_{jet}, as shown in Figure 8.13.

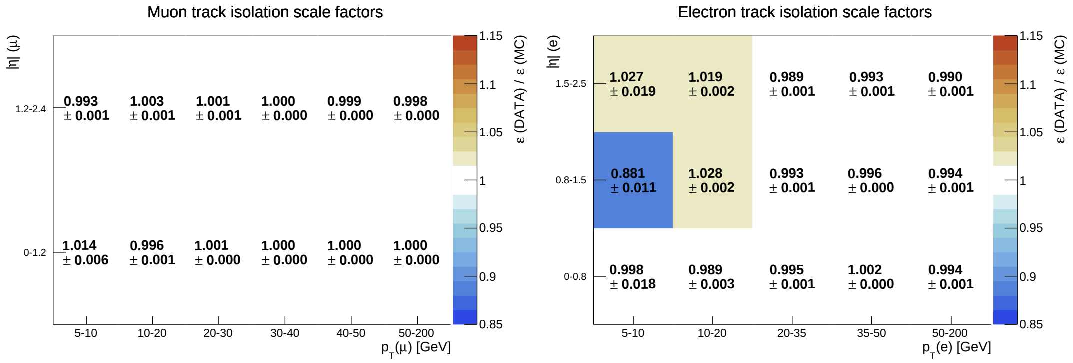

Figure 8.12: Scale factors (ratio of efficiency in data to efficiency in MC) for muon (left) and electron (right) track isolation.

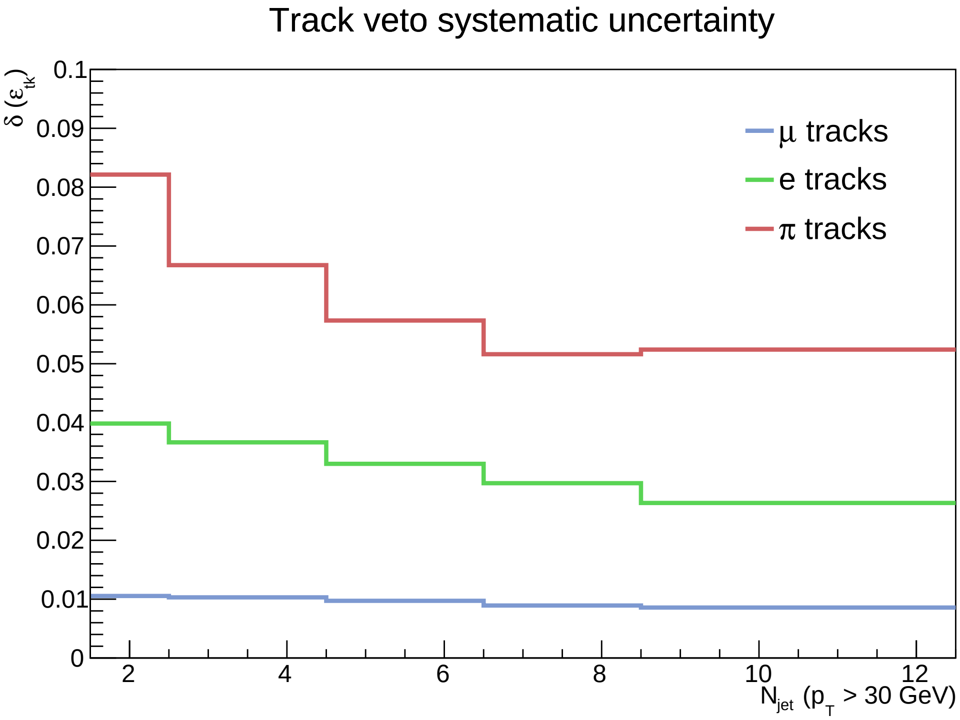

Figure 8.13: Systematic uncertainty on ϵ_{tk}, plotted as a function of N_{jet}. The uncertainties corresponding to the muon and electron track vetoes are calculated according to Equation 8.45 while the uncertainties corresponding to the hadronic (π) track veto are calculated according to Equation 8.48.

8.3 Top quark and W+jets: hadronic τ

8.3.1 Control region

The estimation of the background from standard model $W^{\pm}$ bosons decaying to tau leptons that decay hadronically begins with a control region partially overlapping with that of the lost lepton background estimation. Events are selected using the logical OR of three single muon triggers, one requiring a 15 GeV iso-

Source	Typical Stat. Uncert. (%)	Typical Syst. Uncert. (%)	Correlation assumptions
CR stats.	2-100+	–	Uncorrelated across bins
MC closure	2-30	–	Uncorrelated across bins
$\epsilon_{\rm tk}^{\mu,e}$	5-9	1-3	Fully-correlated across bins
$\epsilon_{\rm ACC}$	1-10	1-4	Uncorrelated across bins
$\epsilon_{\rm RECO}$	0.5-1.5	2-6	Fully-correlated across bins
$\epsilon_{\rm ISO}$	0.5-1.5	1-4	Fully-correlated across bins
ϵ_{m_T}	1-7	1-3	Uncorrelated across bins
Other	0.5-1	1-2	Varies

Table 8.3: Summary of the sources of systematic uncertainty on the lost lepton background estimation. For each systematic, a range of the typical values of the corresponding uncertainty, separated into statistical (i.e., the propagation of the statistical uncertainty from the MC efficiency maps) and systematic components, is provided, along with the correlation structure of the systematic component across search bins.

Table 8.4: Trigger efficiency for the single muon triggers used to select the control sample used in the hadronic τ background estimation. The first uncertainty is statistical and the second is systematic.

μ trig. ϵ [%]	$25 < p_T \leq 30$	$30 < p_T \leq 50$	$p_T > 50$
$300 < H_T < 500$	$78.7^{+0.3+3.0}_{-0.3+3.0}$	$84.3^{+0.2+2.0}_{-0.2+2.0}$	$90.8^{+0.1+1.0}_{-0.1+1.0}$
$H_T > 500$	$94.9^{+0.1+1.0}_{-0.1+1.0}$		

lated muon candidate and $H_T > 350$ GeV, one a 22 GeV isolated muon candidate and no H_T requirement, and one a 50 GeV muon with no isolation nor H_T requirements. Offline, the selected muons are required to have $p_T > 25$ GeV and $|\eta| < 2.1$, and to satisfy $m_T < 100$ GeV. The efficiency for the OR of these triggers is measured as a function of offline muon p_T and offline H_T and is reported in Table 8.4.

8.3.2 Translation factor

The translation factor used to extrapolate from the single muon CR to a hadronic tau background estimation in the SR shares many features with the lost lepton method's translation factor. The control region yield in each bin is corrected to account for:

- the muon reconstruction and identification efficiency ($\epsilon^{\mu}_{\mathrm{RECO}}$),
- the muon isolation efficiency ($\epsilon^{\mu}_{\mathrm{ISO}}$),
- the muon acceptance ($\epsilon^{\mu}_{\mathrm{ACC}}$),
- the efficiency of the m_T cut for single-muon CR events ($\epsilon^{\mu}_{m_T}$),
- and the dilepton event contamination of the CS ($f_{\ell\ell} \approx 0.02$).

The following corrections are also incorporated:

- the efficiency of the single muon triggers, $\epsilon^{\mu}_{\mathrm{TRIG}}$, reported in Table 8.4;
- the ratio of branching fractions $\mathcal{B}(W \to \tau_{\mathrm{h}}\nu)/\mathcal{B}(W \to \mu\nu) = 0.6476 \pm 0.0024$ [102];
- the contamination of the single-muon CR from $W \to \tau\nu_{\tau} \to \mu\nu_{\mu}\bar{\nu}_{\tau}\nu_{\tau}$ events, as opposed to direct decays of the W to a muon and one neutrino ($f_{\tau\to\mu}$, which is determined from simulation);

- and the fraction of hadronic tau events rejected in each bin by the isolated hadronic track veto ($\epsilon_{\mathrm{tk}}^{\mathrm{HAD}}$, which is determined from simulation).

The decay of a tau lepton to hadrons and a neutrino may produce an additional jet and additional H_T^{miss} in the detector. To account for the difference in detector response between the $\mathrm{W} \to \mu\nu$ and $\mathrm{W} \to \tau_{\mathrm{h}}\nu$ processes, the measured muon p_T in control region events is smeared according to a $\mathrm{W} \to \tau_{\mathrm{h}}\nu$ response function, or "template." This function is derived from a simulated sample of single $\mathrm{W} \to \tau_{\mathrm{h}}\nu$ and is defined as the ratio of the measured p_T of a tau jet to that of the generated τ . The jet is matched to the τ at generator level. The function is binned in the p_T of the generated τ, as shown in Figure 8.14. The specifics of the smearing are described as follows:

For each control region event, we

- sample from the appropriate response template and replace the measured muon p_T with the value of $p_T(\tau_{\mathrm{h}}^{\mathrm{visible}})$ corresponding to each template bin;
- subtract the original muon p_T and then add the corresponding $p_T(\tau_{\mathrm{h}}^{\mathrm{visible}})$ to the jet matched to the muon;
- for each values of $p_T(\tau_{\mathrm{h}}^{\mathrm{visible}})$, recalculate the kinematic variables N_{jet}, H_T, H_T^{miss}, as well as the $\Delta\phi(j_i,\ H_T^{\mathrm{miss}})$ variables;

- and determined a weight from the template for the event to contribute to each bin of the kinematic distributions and thus to each search bin.

We also include a weight to account for the small probability that a τ_{h} jet is mistagged as a b jet, $w^{\tau_{\mathrm{h}}}_{\mathrm{b-mis.}}$.

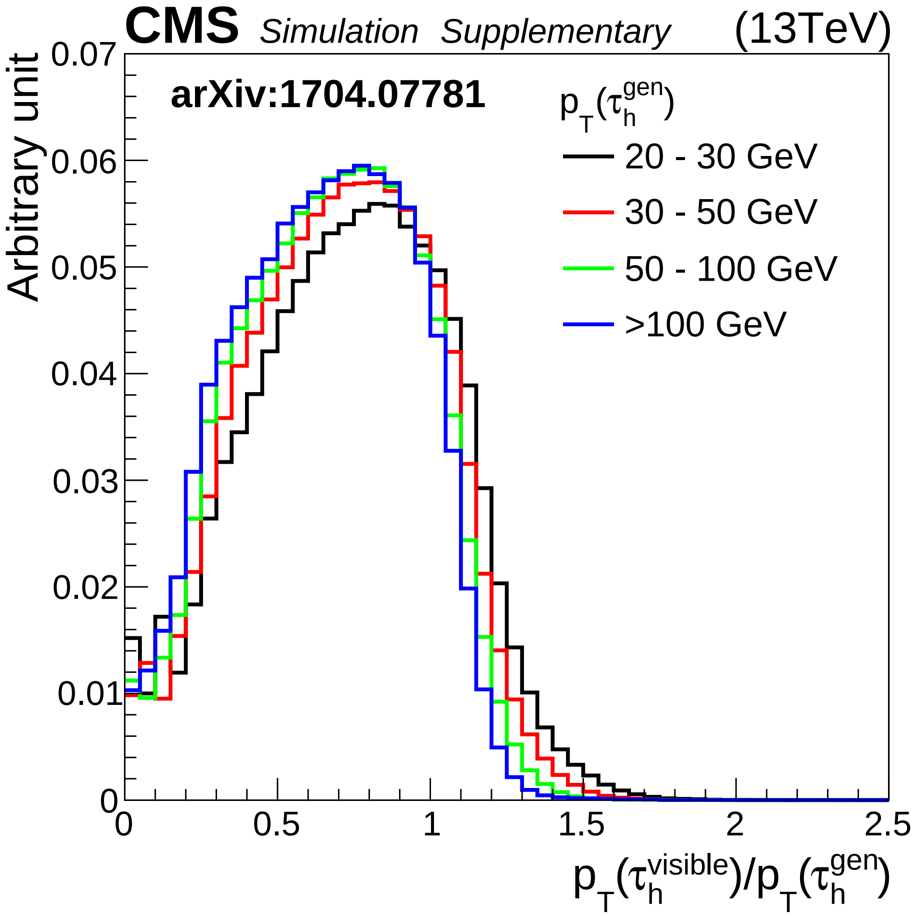

Figure 8.14: The hadronically-decaying τ lepton (τ_{h}) response templates: distributions of the ratio of τ_{h} visible-p_{T} to true-p_{T}, $p_{\mathrm{T}}(\tau_{\mathrm{h}}^{\mathrm{visible}})/p_{\mathrm{T}}(\tau_{\mathrm{h}}^{\mathrm{gen}})$, in intervals of $p_{\mathrm{T}}(\tau_{\mathrm{h}}^{\mathrm{gen}})$ as determined from a simulation of single $\mathrm{W} \to \tau_{\mathrm{h}}\nu_{\tau}$ decay events.

If we define the product of the muon efficiencies as

$$\epsilon^{\mu}_{\mathrm{FULL}} = \frac{1}{\epsilon^{\mu}_{\mathrm{Trig}}} \cdot \frac{1}{\epsilon^{\mu}_{\mathrm{ACC}}} \cdot \frac{1}{\epsilon^{\mu}_{\mathrm{RECO}}} \cdot \frac{1}{\epsilon^{\mu}_{\mathrm{ISO}}} \cdot \frac{1}{\epsilon^{\mu}_{m_T}}, \tag{8.46}$$

then the final τ_{h} background prediction for each of the 174 bins can be written somewhat compactly as

$$\eta_i = \sum_{j}^{\mathrm{temp.}} \left(P^{\mathrm{resp}}_{\tau_{\mathrm{h}}} \cdot w^{\tau_{\mathrm{h}}}_{\mathrm{b-mis.}}\right) \cdot \epsilon^{\mathrm{FULL}}_{\mu} \cdot (1 - f_{\tau\to\mu}) \cdot (1 - f_{\ell\ell}) \cdot \frac{\mathcal{B}(\mathrm{W} \to \tau_{\mathrm{h}}\nu)}{\mathcal{B}(\mathrm{W} \to \mu\nu)} \cdot \epsilon^{\mathrm{HAD}}_{\mathrm{tk}},$$

$$N^{\tau_{\mathrm{h}}}_{\mathrm{SR}} = \sum_{i}^{N^{\mu}_{\mathrm{CR}}} \eta_i, \tag{8.47}$$

In the above expressions, we calculate a quantity η_i for each control region event by summing over each bin j of the τ_{h} response template, $P^{\mathrm{resp}}_{\tau_{\mathrm{h}}}$, and multiplying by all of the correction factors described above. Within each control region, we then sum over all N^{μ}_{CR} events to get an estimated number of τ_{h} events in each search region, $N^{\tau_{\mathrm{h}}}_{\mathrm{SR}}$.

8.3.3 Systematic uncertainties

As in the case of the lost lepton background estimation, a closure test is performed by running the hadronic tau prediction on a simulated sample of background events and comparing that prediction to the result obtained directly from the simulated sample. The results of this test are shown in one-dimensional projections of the distributions of the four kinematic search variables in Figure 8.15.

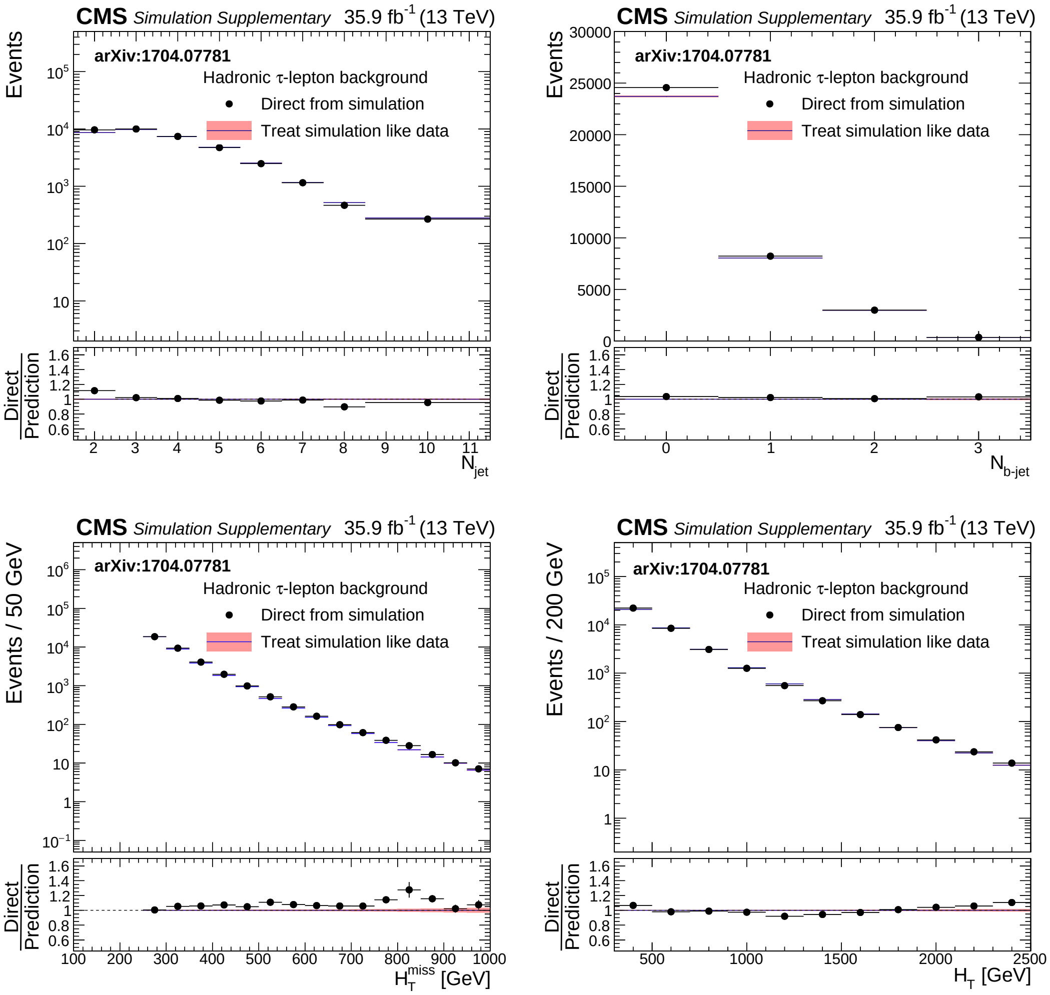

Figure 8.15: Closure test of the hadronic tau background estimation method performed on MC, shown as a function of the four kinematic search variables.. The black points show the background as determined directly from MC and the histograms show the background predicted by running the prediction on a simulated sample of single muon events. The MC samples include $t\bar{t}$, W+jets, tW, single-t, and rare processes, all normalized to either NLO or NNLO cross sections. Only statistical uncertainties are shown.

We see satisfactory agreement within statistical uncertainties between the shapes obtained directly and those obtained by running the prediction on simulation in the H_T^{miss} and H_T distributions. We observe some systematic non-closure, however, in the N_{jet} and $N_{b\text{-jet}}$ distributions. We derive a correction to the data-driven prediction from this non-closure, which we apply in two-dimensional bins of N_{jet} and $N_{b\text{-jet}}$, integrating over H_T^{miss} and H_T (Figure 8.16). These corrections are on the order of 1 to 10% for nearly all of the two-dimensional bins. A systematic uncertainty equal to one half of the correction is applied to the final data-driven prediction.

After applying this correction, we run a closure test on the background estimation in each of the 174 search bins. The prediction of the background, as determined from running the method on simulation, agrees within the background expectation determined directly from simulation to within 10% in most of the high-statistics search bins, as shown in Figure 8.17.

The following sources of systematic uncertainty are also considered. For most systematics, one or more of the parameters taken from simulation is varied within its assumed uncertainty, and that variation is propagated to the final prediction. These uncertainties are summarized in Table 8.5.

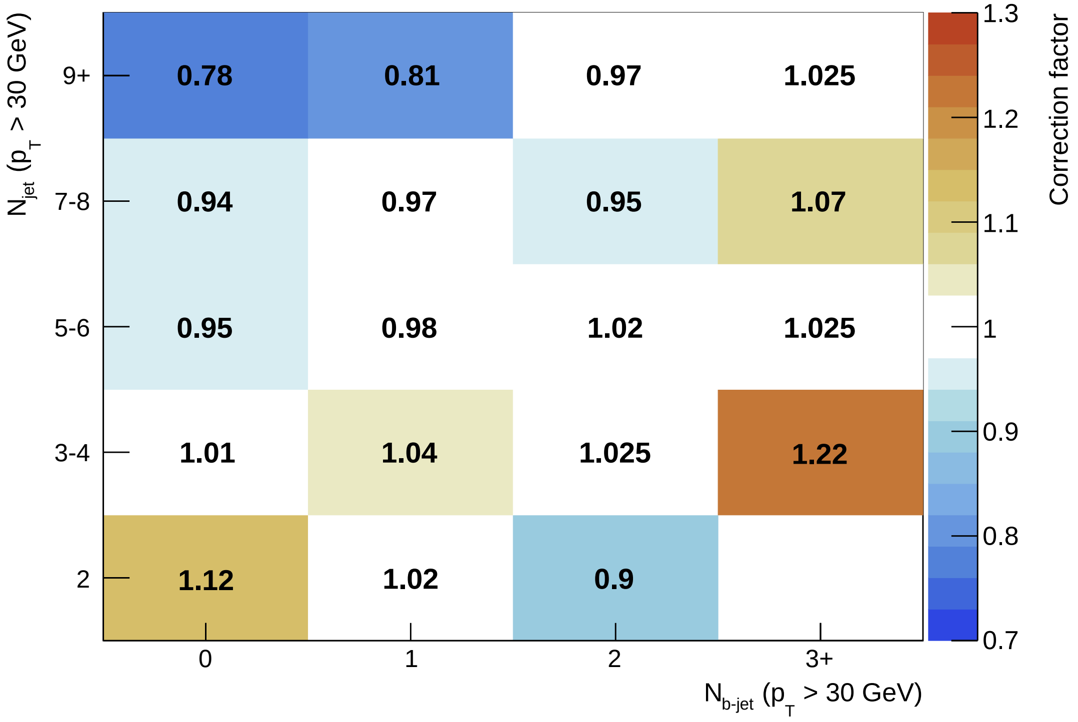

Figure 8.16: Multiplicative correction factors applied to the data-driven hadronic tau background prediction to correct for the small non-closure in these dimensions observed in Figure 8.15.

Hadronic tau response template

The hadronic tau jet energy scale is varied within its uncertainty, which is measured in Ref. [113].

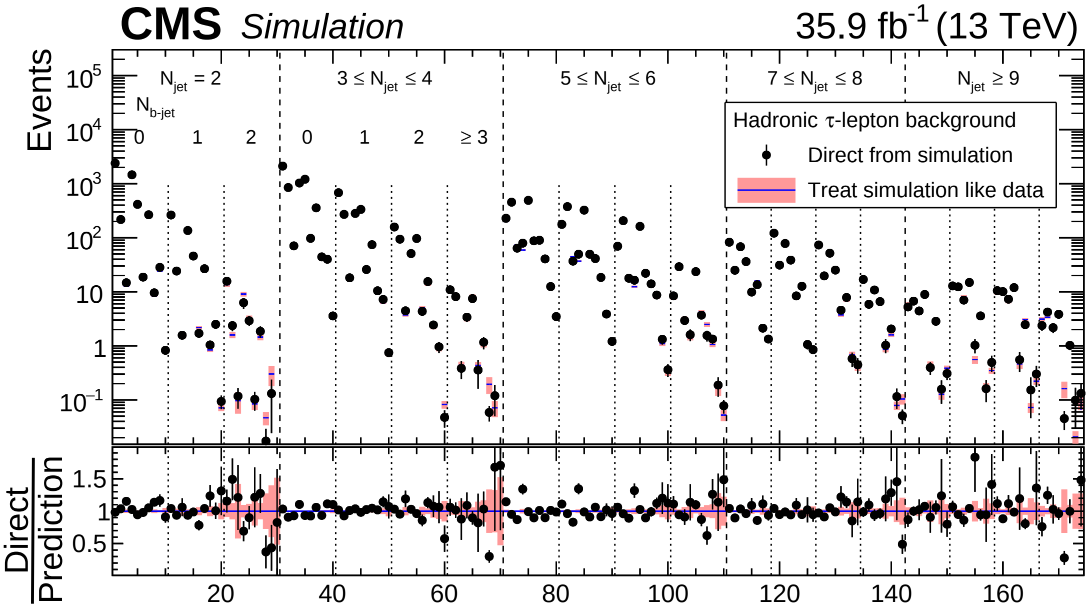

Figure 8.17: Closure test of the hadronic tau background estimation method performed on MC. The black points show the background as determined directly from MC and the histograms show the background predicted by running the prediction on a simulated sample of single muon events. The MC samples include $t\bar{t}$, W+jets, tW, single-t, and rare processes, all normalized to either NLO or NNLO cross sections. Only statistical uncertainties are shown. The labeling of the bin numbers is the same as in Fig. 8.2.3.

b-mistag rate

The probability of mistagging a τ jet as a b jet is varied up and down by a conservative 50%.

Muon reconstruction/ID/isolation efficiency

These efficiencies are varied within the uncertainties on the data/MC corrections derived from tag-and-probe studies as discussed in Section 8.2.3.

Acceptance

The PDFs are varied within their uncertainties and the renormalization and factorization scales up and down by factors of two. The statistical precision of the MC is also included in this uncertainty.

Dilepton correction

A flat uncertainty of 100% on the subtraction of the dilepton contamination, which is around 2% in the control region is considered.

m_T cut efficiency

The value of the E_T^{miss} is varied up and down by 30%. We also consider the statistical precision of the calculation of this efficiency in simulation.

Isolated track vetoes

The hadronic tau veto reduces the expected background by around 30% in most search bins. This background reduction factor ($\epsilon_{\mathrm{tk}}^{\mathrm{HAD}}$) is taken directly from simulation. We cannot validate the isolation efficiency directly for hadronic tracks; instead we must extrapolate the validation of the muon track efficiencies to the hadronic tracks. We justify the assumption that the track isolation efficiencies for muon tracks are an appropriate proxy for the track isolation efficiencies for hadronic tracks by arguing:

1. Most of the taus in the events rejected by the hadronic track veto undergo one-prong decays. According to simulation, 96% or more of the rejected events in most search bins have one-prong decays.

2. Since the the isolation is computed by summing over neighboring charged tracks, and no neutral candidates, the isolation distributions for muon tracks should be similar to those for pions from single-prong tau decays.

A comparison of the muon and pion (form one-prong tau decays) track isolation efficiencies in simulated background events, suggests that the pion track isolation efficiencies are lower than the muon track efficiencies by around 15% or less. This difference is believed to be due to neutral pions from tau decays that decay into photons, which convert to e^+e^- pairs in the tracker, thus potentially increasing the amount of charged activity around the candidate.

A conservative uncertainty of one half of the fractional difference between the muon and pion track efficiencies is added in quadrature with the tag-and-probe isolation efficiency. This extrapolation uncertainty is only applied to the 96+% of MC hadronic track events that have a single-prong tau. For the few multi-prong tau events expected to be rejected by the track veto, we apply a conservation 100% uncertainty on the isolation efficiency, yield the following expression for the uncertainty on $\epsilon_{\text{tk}}^{\text{HAD}}$:

$$\delta(\epsilon_{\text{tk}}^{\text{HAD}}) = (1 - f_{1\pi^{\pm}}) + f_{1\pi^{\pm}} \cdot \sum_{\substack{i=p_T-\text{bin} \\ j=\eta-\text{bin}}} f_{ij}^{\pi} \cdot \delta(\epsilon_{\text{ISO}}^{\pi/\mu})_{ij} \tag{8.48}$$

where, for a given search bin, $f_{1\pi^{\pm}}$ is the fraction of rejected hadronic tau events with a single-prong tau decay, f_{ij}^{π} is the fraction of rejected events with a charged pion from that decay in $p_T - \eta$ bin (i, j) and $\delta^{(}\epsilon_{\text{ISO}}^{\pi/\mu})_{ij}$ is the sum in quadrature of the muon track isolation and muon-pion extrapolation uncertainties corresponding to that $p_T - \eta$ bin. As is the case for the leptonic track veto, this uncertainty varies most strongly as a function of N_{jet}, so it is parametrized in five bins of N_{jet}, as shown in Figure 8.13.

Table 8.5: Summary of the sources of systematic uncertainty on the hadronic tau background estimation. For each systematic, a range of the typical values of the corresponding uncertainty, separated into statistical (i.e., the propagation of the statistical uncertainty from the MC efficiency maps) and systematic components, is provided, along with the correlation structure of the systematic component across search bins.

Source	Typical Stat. Uncert. (%)	Typical Syst. Uncert. (%)	Correlation assumptions
CR stats.	2-100+	–	Uncorrelated across bins
MC closure	2-100	–	Uncorrelated across bins
Ad-hoc correction	–	1-20	Correlated across H_T and H_T^{miss}
$\epsilon_{\text{tk}}^{\text{HAD}}$	1-5	2-9	Correlated across $N_{b\text{-jet}}$
ϵ_{ACC}	1-6	1-4	Correlated across $N_{b\text{-jet}}$
ϵ_{RECO}	0.5-1.5	2-6	Fully-correlated across bins
ϵ_{ISO}	0.5-1.5	1-4	Fully-correlated across bins
ϵ_{m_T}	1-7	1-3	Correlated across $N_{b\text{-jet}}$
ϵ_{Trig}	–	2	Correlated across N_{jet} and $N_{b\text{-jet}}$
JEC	–	1-10	Fully-correlated across bins
b-mistag	–	1-5	Correlated across $N_{b\text{-jet}}$
$f_{\tau\to\mu}$	0.5-6	–	Correlated across $N_{b\text{-jet}}$
Other	0.5-1	1-2	Varies

Correlation of uncertainties between the lost lepton and hadronic τ estimation methods

The lost lepton and hadronic tau background estimations share a control region of single muon events. Though full control regions are not identical (lost lepton also uses single electron events and hadronic tau uses events with lower H_T^{miss}), we conservatively treat the systematic uncertainty from the poisson statistics of their control regions as fully correlated. This approximation has little impact on the sensitivity of the analysis to the signal models we consider. Other systematics that are fully correlated between the two methods include those related to the muon acceptance and efficiencies, the dilepton correction, and the m_T cut efficiency.

8.4 QCD multijets

The third and least prevalent SM background for the jets + H_T^{miss} final state comes from events produced exclusively through the strong interaction, known as QCD multijet events. These events usually enter the search region because of instrumental or reconstruction failures. Typically, the momenta of one or more jets are undermeasured by several hundred GeV. We sometimes describe these events as having "fake-H_T^{miss}." An apparent imbalance of jet momenta can also arise if one or more jets lie outside of kinematic ($p_T < 30$ GeV) or geometric ($|\eta| > 5$) detector acceptance and are not counted in the momentum vector sum. Yet another source of H_T^{miss} in QCD events comes from weak decays of strongly produced heavy flavor hadrons, e.g., $B^+ \to \ell^+\nu_\ell$. These decays may result in final states with neutrinos and genuine H_T^{miss}, though the momenta of these neutrinos are usually not large enough for the events to enter the search region without some fake H_T^{miss} as well.

While large instrumental and reconstruction failures are rare, the enormous QCD cross sections make this background a concern for most hadronic SUSY searches. These failures are difficult to simulate, so data-driven techniques are vital for estimating this background with manageable uncertainties. This analysis employs two complementary methods to estimate the background, both introduced in previous searches on CMS: the rebalance-and-smear (R&S) method [110, 104] and the low-$\Delta\phi$ extrapolation method [111, 104].

8.4.1 Rebalance-and-smear method

The central values of the QCD background prediction come from the first method, known as rebalance-and-smear (R&S). The control sample for this method is selected with prescaled triggers that only require minimal amounts of H_T, ranging from 250 to 800 GeV.

The method begins with a "rebalancing" step, in which the momenta of all jets in an event are modified to effectively undo the effects of detector response. Specifically, a prior probability distribution is derived from generator-level QCD jet simulation, and is given by

$$\pi(\vec{H}_T^{\text{miss}}, \vec{p}_{T,\,\text{j}_1}) = \mathcal{P}\left(H_T^{\text{miss}}\right)\, \mathcal{P}\left(\Delta\phi_{H_T^{\text{miss}},\text{j}_{1(b)}}\right), \tag{8.49}$$

where $\mathcal{P}(H_T^{\text{miss}})$ is the distribution of H_T^{miss}. In events with $N_{b\text{-jet}} = 0$, $\mathcal{P}(\Delta\phi_{H_T^{\text{miss}},\text{j}_{1(b)}})$ is the distribution of the azimuthal angle ϕ between $\vec{H}_T^{\text{miss}}$ and the leading jet in the event, while in events with $N_{b\text{-jet}} > 0$ it represents the angle between $\vec{H}_T^{\text{miss}}$ and the leading b-tagged jet. This prior is binned in $N_{b\text{-jet}}$ and H_T in order to take into account the magnitude and direction of any genuine H_T^{miss}, which, in QCD, appears most often in events with b-tagged jets, or of any apparent H_T^{miss} due to out-of-acceptance jets.

The momenta of the jets are rescaled to mimic the event at the particle (or generator jet) level according to the following expression of Bayes's theorem:

$$\mathcal{P}(\vec{J}_{\text{part}}|\vec{J}_{\text{meas}}) \sim \mathcal{P}(\vec{J}_{\text{meas}}|\vec{J}_{\text{part}})\,\pi(\vec{H}_T^{\text{miss}}, \vec{p}_{T,\,\text{j}_1}). \tag{8.50}$$

Above, $\mathcal{P}(\vec{J}_{\text{part}}|\vec{J}_{\text{meas}})$ represents the the posterior probability density for a set of particle-level jet momenta $\vec{J}_{\text{part}}$ given the measured set $\vec{J}_{\text{meas}}$. The $\mathcal{P}(\vec{J}_{\text{meas}}|\vec{J}_{\text{part}})$ term is a likelihood function, defined by the product of momentum response functions for all jets in the event:

$$\mathcal{P}(\vec{J}_{\text{meas}}|\vec{J}_{\text{part}}) = \prod_{i=1}^{N_{\text{jet}}} \mathcal{P}(p^{\mu}_{i,\text{meas}}|p^{\mu}_{i,\text{part}}) \tag{8.51}$$

These jet momentum response functions are derived from simulation and are essentially distributions of the ratio of reconstructed jet p_T values for a given generated p_T and η. The distributions are corrected with separate scale factors for the Gaussian cores and non-Gaussian tails to account for differences in jet energy resolution (JER) between simulation and data. The set of rescaled jet momenta that maximizes the posterior density $\mathcal{P}(\vec{J}_{\text{part}}|\vec{J}_{\text{meas}})$ defines the rebalanced event.

Next, in the "smear" phase of the method, the magnitudes of the jet momenta are rescaled, this time by random sampling from the response functions. To increase the statistical precision of the sample and ultimately the background measurement, this sampling is performed many times per event. The resulting sample of rebalanced events closely resembles the initial control sample, except contributions from electroweak processes, i.e., those producing genuine H_T^{miss}, are effectively removed. Finally, the same event selection described in Section 7.2–7.3 is performed on the sample. The number of events surviving this selection in each search bin represents the expected background contribution from QCD.

We are able to perform a powerful validation of this method by evaluating the QCD background in a sideband of events in data. This sideband is selected using the same triggers and offline criteria as the search region, except the $\Delta\phi$ cut is inverted, i.e., the events must fail the requirement described by Equations 7.30–7.31. This sideband is divided into 174 orthogonal sideband bins mirroring the binning of the search region. The electroweak background contribution in the low-$\Delta\phi$ sideband is estimated using the data-driven techniques described in Sections 8.1–8.3.3 and then subtracted from the observed number of events in each bin. The subtracted observation, or "expectation," in each bin is compared to the number of events predicted by the R&S method and the results are presented in Figure 8.18. The values predicted by R&S generally agree with the expected values withtin uncertainties. As in the case of the lost lepton and hadronic τ measurements, an uncertainty equal to the maximum of the deviation between the predicted and expected values and the uncertainty on that deviation is assigned to the R&S prediction.

The largest uncertainty on the R&S background prediction comes from the jet momentum response functions. This systematic is evaluated by varying the jet energy resolution scale factors within their uncertainties and propagating those variations through to the final prediction, resulting in uncertainties ranging from 20-80%, depending on the search region. Smaller systematic uncertainties associated with the trigger, the prior density π, and the statistics of the control sample are also evaluated and summarized in Table 8.6.

Table 8.6: Summary of the sources of systematic uncertainty on the QCD background estimation. For each systematic, a range of the typical values of the corresponding uncertainty is provided, along with the correlation structure of the systematic component across search bins.

Source	Typical Uncert. (%)	Correlation assumptions
CR stats.	1-100+	Uncorrelated across bins
Low-$\Delta\phi$ sideband closure	20	Uncorrelated across bins
JER Core SF	6-55	Fully-correlated across bins
JER Tail SF	32	Fully-correlated across bins
Extrap. in $N_{b\text{-jet}}$ ($N_{b\text{-jet}} \geq 3$ or $N_{\text{jet}} = N_{b\text{-jet}} = 2$)	100	Fully-correlated across bins
EWK contamination	0-5	Uncorrelated across bins
Prior	5	Uncorrelated across bins
Trigger eff.	0-3	Uncorrelated across bins

8.4.2 Low-$\Delta\phi$ extrapolation method

We perform yet another validation of the R&S method by cross-checking its predictions against those of the low-$\Delta\phi$ extrapolation method. As described

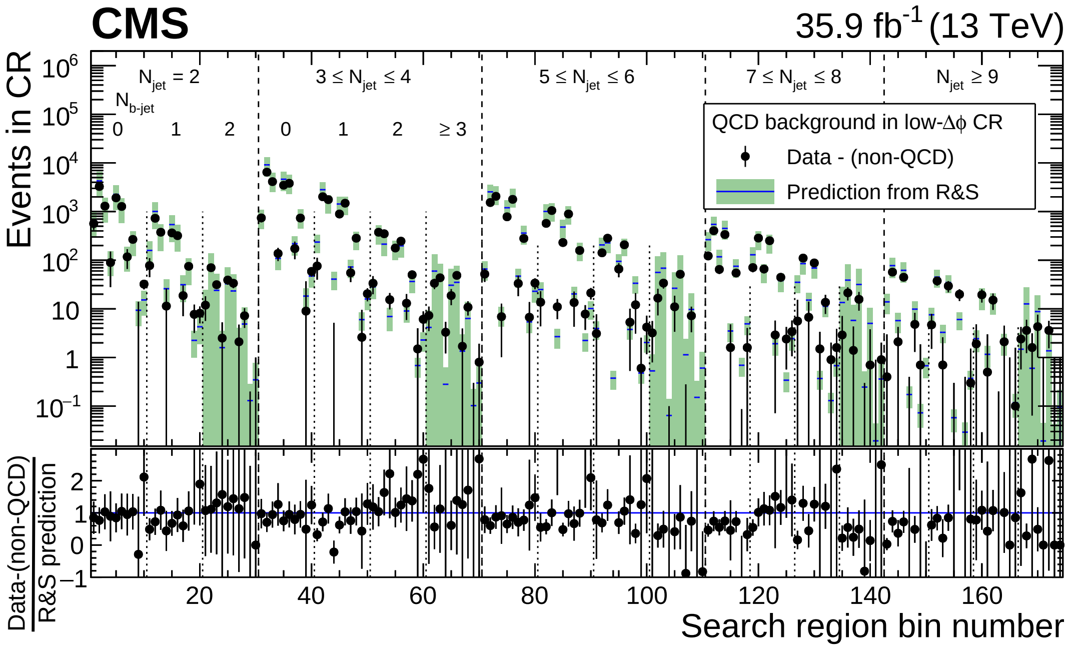

Figure 8.18: Closure test of the rebalance-and-smear method: comparison of the R&S method evaluated on data in the low-$\Delta\phi$ control region (histograms, with statistical and systematic uncertainties added in quadrature), compared to the corresponding observed data in that region, from which the expected contribution from electroweak processes (e.g., $t\bar{t}$, W+jets, and Z+jets events) has been subtracted (points, with statistical uncertainties). The lower panel shows the ratio of the measured to the predicted results and its propagated uncertainty. The labeling of the bin numbers is the same as in Fig. 8.2.3.

above, a control sample of QCD events is selected by inverting the $\Delta\phi$ selection described by Equations 7.30–7.31 and then subtracted the data-driven electroweak background contributions (W/top, $Z \to \nu\bar{\nu}$) in this region. The post-subtraction observed event yield in each control bin is scaled by by a translation factor R^{QCD} determined primarily from data:

$$N^{\text{QCD}}_{i,j,k,l}\,(\text{SR}) = R^{\text{QCD}}_{i,j,k} \cdot N^{\text{QCD}}_{i,j,k,l}\,(\text{CR}), \tag{8.52}$$

where i, j, k, and l are the H_T, N_{jet}, H_T^{miss}, and $N_{b\text{-jet}}$ bin indices, respectively, $N^{\text{QCD}}_{i,j,k,l}$ (SR) is the expected number of QCD events in a given search bin, and $N^{\text{QCD}}_{i,j,k,l}$ (CR) is the number of QCD events in the corresponding control bin. While there is a unique control bin for each search bin, R^{QCD} is empirically observed to have a negligible dependence on $N_{b\text{-jet}}$ for a given value of N_{jet}. Thus R^{QCD} is only binned H_T, H_T^{miss}, and N_{jet}.

The ratios $R^{\text{QCD}}_{i,j,k}$ are primarily determined in data in a low-H_T^{miss} sideband; that is, in a sample of events with $250 < H_T^{\text{miss}} < 300$ GeV (regions C1, C2, and C3 in Figure 7.3), we essentially calculate the ratio of the number of events passing the $\Delta\phi$ cut to the number failing the $\Delta\phi$ cut. This ratio, however, is not necessarily applicable in the high-H_T^{miss} (> 300 GeV) search region. The $\Delta\phi$ distributions show some dependence on H_T^{miss}; at higher values of H_T^{miss}, the the $\Delta\phi$ distribution has greater resolution (or a smaller spread). Consequently, we expect the $\Delta\phi$ selection's pass-to-fail ratio to be lower at high-H_T^{miss}.

We use a likelihood model to determine the ratios, carefully taking into account their dependence on H_T^{miss}. The model assumes that this dependence factorizes from the ratios' dependence on H_T and N_{jet}:

$$R_{i,j,k}^{\text{QCD}} = K_{H_T-N_{\text{jet}},\, ij}^{\text{QCD}} \cdot S_{H_T^{\text{miss}},\, ik}^{\text{QCD}} \;, \tag{8.53}$$

where $K_{H_T-N_{\text{jet}},\, ij}^{\text{QCD}}$ is the pass-to-fail ratio for H_T bin i and N_{jet} bin j in the low-H_T^{miss} sideband (250 to 300 GeV). The $S_{H_T^{\text{miss}},\, ik}^{\text{QCD}}$ term is a correction for H_T^{miss} bin k with respect to the low-H_T^{miss} sideband that also depends on H_T.

Practically speaking, the complete low-$\Delta\phi$ extrapolation method is summarized as follows:

1. The scaling of R^{QCD} with H_T^{miss} (the $S_{MHT,jk}^{QCD}$ parameters) is calculated directly from QCD MC.
2. The H_T and N_{jet} dependence of R^{QCD} ($K_{HT-Njet,ij}^{QCD}$ terms) is determined by a maximum likelihood fit to the data in the low-H_T^{miss} sideband.
3. The expected electroweak background contribution in each low-$\Delta\phi$ control bin is calculated and subtracted from the observed number of events.
4. The remaining yield ($N_{i,j,k,l}^{\text{QCD}}$ (CR)) in each control bin is scaled by the appropriate $\Delta\phi$ transfer factor $R_{i,j,k}^{QCD}$. The result is the expected number of QCD events in each search bin, $N_{i,j,k,l}^{\text{QCD}}$ (SR).

Systematic uncertainties associated with $K^{QCD}_{HT-Njet,ij}$ are determined from the covariance matrix of the fit. Uncertainties on the $S^{QCD}_{MHT,jk}$ terms, which come directly from QCD simulation, are estimated by studying the frequency of events in which the jet with the largest p_T mismeasurement is or is not amongst the jets considered in the $\Delta\phi$ selection. Based on these studies, uncertainties between 14 and 100% are assigned to the $S^{QCD}_{MHT,jk}$ terms to account for potential differences between data and simulation. The statistics of QCD simulation and of the control regions in data are taken into account, as are the uncertainties on the subtracted data-driven electroweak contributions in the control regions. Finally, we perform a closure test of the method in simulation and present the results in Figure 8.19. Based on the observed nonclosure, which appears to be mostly statistical, we assign an additional systematic uncertainty.

8.4.3 Comparing the two methods

We compare the predictions of the R&S and $\Delta\phi$ methods in Figure 8.20. The results are generally consistent; any differences are negligible compared to the overall uncertainties.

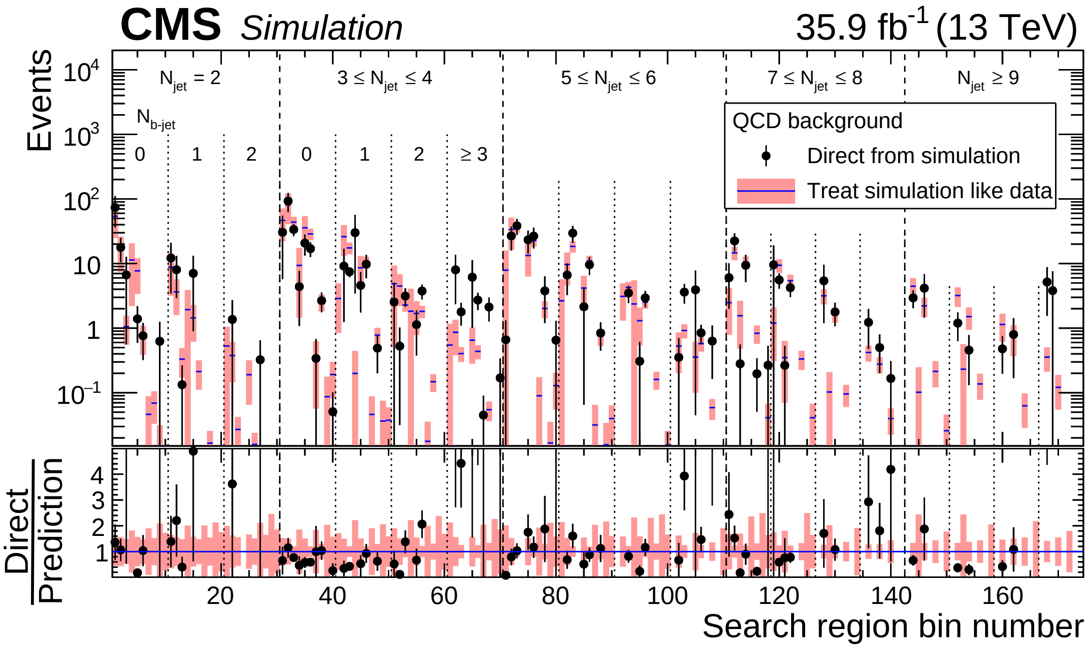

Figure 8.19: Closure test of the low-$\Delta\phi$ extrapolation method: comparison of the expected QCD background taken directly from simulation (points with error bars) with the results of the low-$\Delta\phi$ extrapolation run on a sample of simulated control region events (histogram with solid pink error bars). The uncertainties on the points are from QCD MC statistics, while those on the model include statistical and systematic uncertainties added in quadrature. The results in the lower panel are obtained through bin-by-bin division of the results in the upper panel, including the uncertainties, by the central values of the "predicted" results.

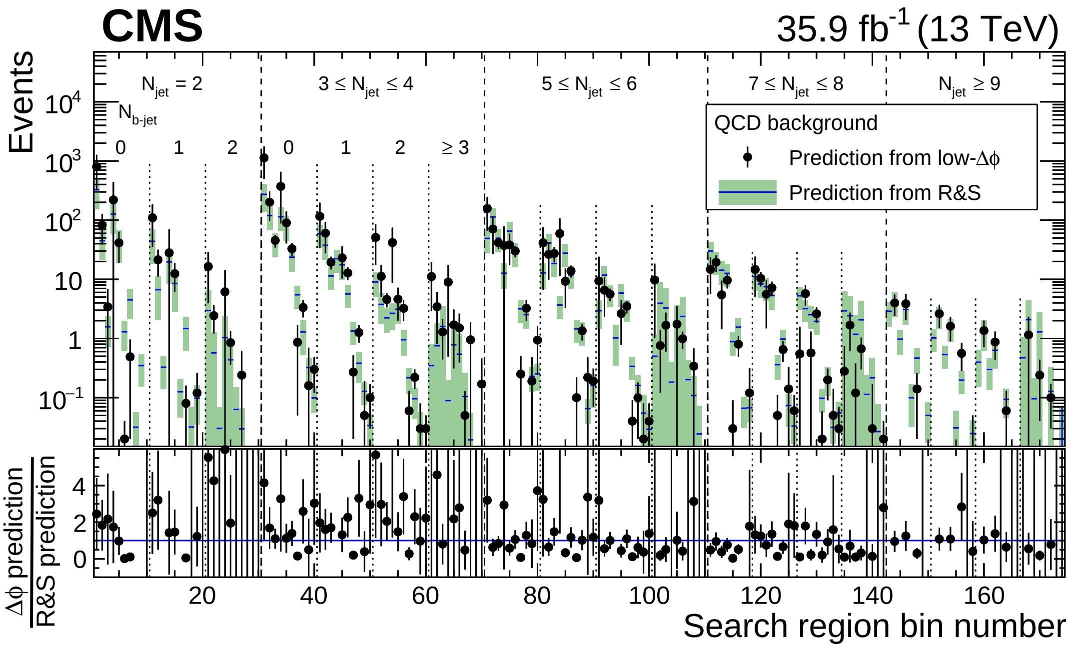

Figure 8.20: Comparison between the estimated number of QCD events in the 174 search regions as determined by the R&S (histograms) and low-$\Delta\phi$ extrapolation (points) methods. For both methods, the error bars indicate the combined statistical and systematic uncertainties. The lower panel shows the ratio of the low-$\Delta\phi$ extrapolation to the R&S result and its propagated uncertainty.

Chapter 9

Results and interpretation

In this chapter, we first present the results of the analysis obtained on the full 2016 dataset.

9.1 Pre-fit results

The observations in the signal regions are found to be in generally good agreement with the predicted backgrounds. For the 174 search bins, the observed data and the pre-fit predictions for each background component are shown in Fig. 9.1 and Tables 9.1–9.5. The observed data and pre-fit background predictions in the aggregate search regions discussed in Section 7.3.2 are reported in Figure 9.2 and Table 9.6. Additionally, Figure 9.3 presents one-dimensional projections of the results in H_T^{miss} or N_{jet}, and $N_{b\text{-jet}}$, integrated over each of the other three search variables.

Table 9.1: Observed numbers of events and prefit background predictions in the $N_{\text{jet}} = 2$ search regions. The first uncertainty is statistical and the second is systematic.

Bin	H_T^{miss} [GeV]	H_T [GeV]	N_{jet}	$N_{b\text{-jet}}$	Lost-e/μ	$\tau \rightarrow$ had.	$Z \rightarrow \nu\bar{\nu}$	QCD	Total pred.	Obs.
1	300–350	300–500	2	0	$4069^{+67+320}_{-67-320}$	$2744^{+37+510}_{-37-500}$	$13231^{+67+760}_{-66-740}$	$326^{+12+170}_{-12-120}$	$20370^{+120+980}_{-120-960}$	21626
2	300–350	500–1000	2	0	326^{+22+36}_{-22-36}	226^{+11+43}_{-11-42}	944^{+18+55}_{-18-54}	45^{+2+24}_{-2-17}	1541^{+37+82}_{-37-79}	1583
3	300–350	>1000	2	0	$15.2^{+5.8+2.3}_{-5.1-2.3}$	$8.7^{+2.1+2.1}_{-2.0-2.1}$	$50.9^{+4.5+4.4}_{-4.1-3.8}$	$1.57^{+0.16+0.84}_{-0.16-0.61}$	$76.3^{+9.1+5.5}_{-8.2-5.0}$	102
4	350–500	350–500	2	0	$2049^{+46+160}_{-46-160}$	$1553^{+27+290}_{-27-290}$	$9347^{+57+540}_{-57-520}$	126^{+4+67}_{-4-48}	$13076^{+93+630}_{-93-620}$	14019
5	350–500	500–1000	2	0	631^{+25+54}_{-25-54}	439^{+14+84}_{-14-84}	$2502^{+30+150}_{-30-140}$	43^{+7+22}_{-7-16}	$3615^{+49+180}_{-49-170}$	3730
6	350–500	>1000	2	0	$13.5^{+4.9+1.9}_{-4.3-1.9}$	$13.4^{+2.4+2.6}_{-2.3-2.6}$	$94.0^{+6.2+7.9}_{-5.8-6.9}$	$1.30^{+0.06+0.68}_{-0.06-0.49}$	$122.1^{+9.5+8.6}_{-8.8-7.6}$	139
7	500–750	500–1000	2	0	303^{+17+29}_{-17-29}	247^{+10+48}_{-10-47}	$2328^{+30+170}_{-29-160}$	$4.5^{+0.1+2.4}_{-0.1-1.7}$	$2883^{+40+180}_{-40-170}$	3018
8	500–750	>1000	2	0	$5.8^{+2.7+1.5}_{-2.2-1.5}$	$5.3^{+1.4+1.3}_{-1.3-1.3}$	$66.2^{+5.4+5.3}_{-5.0-5.1}$	$0.03^{+0.02+0.02}_{-0.02-0.01}$	$77.3^{+6.8+5.7}_{-6.1-5.4}$	96
9	>750	750–1500	2	0	$17.3^{+4.5+3.0}_{-4.1-3.0}$	$17.4^{+2.5+4.5}_{-2.4-4.5}$	295^{+11+41}_{-11-38}	$0.35^{+0.06+0.18}_{-0.06-0.13}$	330^{+13+42}_{-12-38}	272
10	>750	>1500	2	0	$0.0^{+1.8+0.0}_{-0.0-0.0}$	$0.38^{+0.54+0.09}_{-0.29-0.09}$	$12.6^{+3.0+2.1}_{-2.4-1.9}$	$0.01^{+0.01+0.00}_{-0.01-0.00}$	$13.0^{+3.8+2.1}_{-2.5-1.9}$	12
11	300–350	300–500	2	1	370^{+21+31}_{-21-31}	288^{+11+63}_{-11-63}	1361^{+7+140}_{-7-140}	44^{+6+25}_{-6-17}	$2063^{+33+160}_{-33-160}$	1904
12	300–350	500–1000	2	1	51^{+10+7}_{-10-7}	$31.6^{+4.2+7.2}_{-4.2-7.2}$	97^{+2+10}_{-2-10}	$6.7^{+2.7+3.7}_{-2.7-2.5}$	186^{+15+15}_{-14-14}	186
13	300–350	>1000	2	1	$1.1^{+2.3+0.2}_{-1.1-0.0}$	$2.0^{+1.1+0.5}_{-1.0-0.5}$	$5.23^{+0.46+0.63}_{-0.42-0.59}$	$0.33^{+0.02+0.18}_{-0.02-0.13}$	$8.7^{+3.4+0.9}_{-2.1-0.8}$	13
14	350–500	350–500	2	1	215^{+16+19}_{-16-19}	179^{+9+39}_{-9-39}	962^{+6+99}_{-6-98}	20^{+2+11}_{-2-8}	$1376^{+26+110}_{-26-110}$	1212
15	350–500	500–1000	2	1	$69.8^{+9.9+7.5}_{-9.8-7.5}$	$43.3^{+4.4+9.7}_{-4.4-9.6}$	257^{+3+27}_{-3-26}	$8.5^{+3.0+4.8}_{-3.0-3.2}$	379^{+15+30}_{-15-29}	409
16	350–500	>1000	2	1	$3.7^{+2.5+0.7}_{-1.9-0.7}$	$3.1^{+1.1+0.9}_{-1.0-0.9}$	$9.7^{+0.6+1.2}_{-0.6-1.1}$	$0.13^{+0.04+0.07}_{-0.04-0.05}$	$16.6^{+3.7+1.6}_{-3.0-1.6}$	27
17	500–750	500–1000	2	1	$28.9^{+5.8+3.3}_{-5.6-3.3}$	$26.0^{+2.9+5.8}_{-2.9-5.8}$	240^{+3+27}_{-3-26}	$1.48^{+0.18+0.83}_{-0.18-0.56}$	296^{+9+28}_{-9-27}	321
18	500–750	>1000	2	1	$5.1^{+6.2+1.6}_{-4.1-1.6}$	$0.36^{+0.55+0.12}_{-0.30-0.12}$	$6.81^{+0.56+0.80}_{-0.52-0.78}$	$0.03^{+0.03+0.02}_{-0.03-0.00}$	$12.3^{+6.8+1.8}_{-4.5-1.7}$	14
19	>750	750–1500	2	1	$3.8^{+2.2+0.8}_{-1.7-0.8}$	$4.1^{+1.5+1.1}_{-1.4-1.1}$	$30.4^{+1.1+5.0}_{-1.1-4.7}$	$0.10^{+0.03+0.06}_{-0.03-0.04}$	$38.4^{+3.9+5.1}_{-3.3-4.8}$	31
20	>750	>1500	2	1	$0.0^{+1.4+0.0}_{-0.0-0.0}$	$0.34^{+0.51+0.13}_{-0.22-0.13}$	$1.29^{+0.31+0.24}_{-0.25-0.23}$	$0.00^{+0.01+0.00}_{-0.00-0.00}$	$1.6^{+2.0+0.3}_{-0.3-0.3}$	1
21	300–350	300–500	2	2	$14.1^{+4.5+2.6}_{-4.0-2.6}$	$12.9^{+2.3+2.8}_{-2.2-2.8}$	49^{+0+17}_{-0-17}	$3.0^{+0.8+3.6}_{-0.8-2.1}$	79^{+7+18}_{-6-18}	122
22	300–350	500–1000	2	2	$2.8^{+2.4+0.9}_{-1.7-0.9}$	$2.0^{+1.1+1.0}_{-0.9-1.0}$	$3.5^{+0.1+1.2}_{-0.1-1.2}$	$0.57^{+0.17+0.69}_{-0.17-0.40}$	$8.9^{+3.5+2.0}_{-2.6-1.9}$	11
23	300–350	>1000	2	2	$0.0^{+2.2+0.0}_{-0.0-0.0}$	$0.00^{+0.46+0.00}_{-0.00-0.00}$	$0.19^{+0.02+0.07}_{-0.01-0.07}$	$0.03^{+0.01+0.04}_{-0.01-0.02}$	$0.2^{+2.6+0.1}_{-0.0-0.1}$	0
24	350–500	350–500	2	2	$11.4^{+4.5+2.5}_{-3.9-2.5}$	$6.3^{+1.7+2.1}_{-1.6-2.1}$	35^{+0+12}_{-0-12}	$1.0^{+0.5+1.2}_{-0.5-0.6}$	53^{+6+13}_{-6-13}	84
25	350–500	500–1000	2	2	$6.1^{+2.9+1.5}_{-2.4-1.5}$	$2.9^{+1.2+0.8}_{-1.1-0.8}$	$9.3^{+0.1+3.3}_{-0.1-3.3}$	$0.44^{+0.05+0.52}_{-0.05-0.39}$	$18.7^{+4.1+3.8}_{-3.5-3.7}$	23
26	350–500	>1000	2	2	$0.0^{+1.1+0.0}_{-0.0-0.0}$	$0.00^{+0.46+0.00}_{-0.00-0.00}$	$0.35^{+0.02+0.13}_{-0.02-0.13}$	$0.06^{+0.04+0.08}_{-0.04-0.02}$	$0.4^{+1.5+0.1}_{-0.0-0.1}$	2
27	500–750	500–1000	2	2	$1.4^{+2.9+0.4}_{-1.4-0.0}$	$2.03^{+0.84+0.61}_{-0.70-0.61}$	$8.6^{+0.1+3.1}_{-0.1-3.1}$	$0.03^{+0.01+0.04}_{-0.01-0.03}$	$12.1^{+3.7+3.2}_{-2.1-3.2}$	16
28	500–750	>1000	2	2	$0.0^{+2.2+0.0}_{-0.0-0.0}$	$0.00^{+0.46+0.00}_{-0.00-0.00}$	$0.24^{+0.02+0.09}_{-0.02-0.09}$	$0.00^{+0.01+0.00}_{-0.00-0.00}$	$0.2^{+2.7+0.1}_{-0.0-0.1}$	0
29	>750	750–1500	2	2	$0.0^{+1.6+0.0}_{-0.0-0.0}$	$0.07^{+0.46+0.07}_{-0.04-0.06}$	$1.09^{+0.04+0.41}_{-0.04-0.41}$	$0.01^{+0.01+0.01}_{-0.01-0.00}$	$1.2^{+2.1+0.4}_{-0.1-0.4}$	4
30	>750	>1500	2	2	$0.0^{+2.0+0.0}_{-0.0-0.0}$	$0.00^{+0.46+0.00}_{-0.00-0.00}$	$0.05^{+0.01+0.02}_{-0.01-0.02}$	$0.00^{+0.01+0.00}_{-0.00-0.00}$	$0.0^{+2.5+0.0}_{-0.0-0.0}$	0

Table 9.2: Observed numbers of events and prefit background predictions in the $3 \leq N_{\text{jet}} \leq 4$ search regions. The first uncertainty is statistical and the second is systematic.

Bin	H_T^{miss} [GeV]	H_T [GeV]	N_{jet}	$N_{b\text{-jet}}$	Lost-e/μ	$\tau \to$ had.	$Z \to \nu\bar{\nu}$	QCD	Total pred.	Obs.
31	300–350	300–500	3–4	0	$2830^{+45+200}_{-45-200}$	$2152^{+29+160}_{-29-150}$	$8353^{+52+480}_{-52-470}$	$273^{+68+120}_{-68-100}$	$13608^{+110+560}_{-110-540}$	14520
32	300–350	500–1000	3–4	0	$1125^{+25+120}_{-25-120}$	$909^{+18+100}_{-18-100}$	$2487^{+29+140}_{-28-140}$	119^{+8+51}_{-8-45}	$4640^{+52+220}_{-52-210}$	4799
33	300–350	>1000	3–4	0	$72.7^{+7.1+6.1}_{-7.1-6.1}$	$65.3^{+5.2+6.4}_{-5.2-6.3}$	176^{+8+14}_{-8-12}	41^{+2+18}_{-2-16}	356^{+15+24}_{-15-22}	354
34	350–500	350–500	3–4	0	$1439^{+37+110}_{-37-110}$	$930^{+19+120}_{-19-110}$	$5014^{+41+280}_{-41-280}$	114^{+6+48}_{-6-43}	$7496^{+70+330}_{-69-320}$	7973
35	350–500	500–1000	3–4	0	$1402^{+27+140}_{-27-140}$	$1253^{+22+120}_{-22-120}$	$4811^{+40+270}_{-40-260}$	80^{+9+34}_{-9-31}	$7547^{+65+330}_{-64-320}$	7735
36	350–500	>1000	3–4	0	103^{+8+11}_{-8-11}	$77.0^{+5.9+7.6}_{-5.9-7.5}$	303^{+11+24}_{-10-21}	24^{+1+10}_{-1-9}	506^{+18+30}_{-17-26}	490
37	500–750	500–1000	3–4	0	339^{+15+33}_{-15-33}	297^{+10+26}_{-10-26}	$2143^{+28+150}_{-28-140}$	$5.5^{+0.2+2.3}_{-0.2-2.1}$	$2785^{+37+160}_{-37-150}$	2938
38	500–750	>1000	3–4	0	$33.8^{+4.4+3.6}_{-4.3-3.6}$	$30.5^{+3.4+2.9}_{-3.4-2.9}$	219^{+10+16}_{-9-15}	$1.29^{+0.53+0.55}_{-0.53-0.49}$	284^{+12+17}_{-12-16}	303
39	>750	750–1500	3–4	0	$28.2^{+4.4+3.7}_{-4.3-3.7}$	$26.0^{+2.9+3.4}_{-2.9-3.4}$	319^{+11+44}_{-11-40}	$0.32^{+0.03+0.14}_{-0.03-0.12}$	373^{+14+44}_{-13-41}	334
40	>750	>1500	3–4	0	$2.9^{+2.0+0.7}_{-1.5-0.7}$	$1.38^{+0.66+0.17}_{-0.48-0.17}$	$27.8^{+3.9+4.1}_{-3.5-3.8}$	$0.10^{+0.01+0.04}_{-0.01-0.04}$	$32.2^{+4.8+4.2}_{-4.0-3.9}$	46
41	300–350	300–500	3–4	1	746^{+25+55}_{-25-55}	627^{+15+48}_{-15-47}	1235^{+8+130}_{-8-120}	59^{+4+24}_{-4-22}	$2667^{+41+150}_{-41-150}$	2677
42	300–350	500–1000	3–4	1	296^{+15+25}_{-15-25}	262^{+9+27}_{-9-27}	385^{+4+39}_{-4-39}	38^{+4+15}_{-4-14}	981^{+24+56}_{-24-56}	1048
43	300–350	>1000	3–4	1	$20.8^{+4.1+2.1}_{-4.0-2.1}$	$19.0^{+2.6+1.8}_{-2.5-1.8}$	$27.6^{+1.3+3.2}_{-1.2-3.0}$	$11.4^{+0.8+4.7}_{-0.8-4.4}$	$78.8^{+6.9+6.3}_{-6.6-6.0}$	92
44	350–500	350–500	3–4	1	321^{+17+25}_{-17-25}	263^{+10+22}_{-10-21}	738^{+6+74}_{-6-74}	$22.3^{+1.4+9.1}_{-1.4-8.5}$	1343^{+28+82}_{-28-81}	1332
45	350–500	500–1000	3–4	1	329^{+14+26}_{-14-26}	324^{+11+26}_{-11-26}	737^{+6+74}_{-6-74}	$17.6^{+3.4+7.2}_{-3.4-6.7}$	1407^{+26+83}_{-26-83}	1515
46	350–500	>1000	3–4	1	$20.4^{+4.0+2.0}_{-3.8-2.0}$	$19.9^{+2.9+1.8}_{-2.9-1.7}$	$47.5^{+1.7+5.5}_{-1.6-5.1}$	$5.7^{+0.5+2.3}_{-0.5-2.2}$	$93.4^{+7.1+6.5}_{-6.9-6.2}$	113
47	500–750	500–1000	3–4	1	$69.7^{+7.4+6.6}_{-7.3-6.6}$	$56.0^{+4.1+5.0}_{-4.1-4.9}$	322^{+4+35}_{-4-35}	$1.34^{+0.10+0.55}_{-0.10-0.51}$	449^{+12+36}_{-12-36}	472
48	500–750	>1000	3–4	1	$15.3^{+3.4+1.9}_{-3.3-1.9}$	$7.0^{+1.4+0.7}_{-1.4-0.7}$	$34.4^{+1.5+3.8}_{-1.4-3.8}$	$0.38^{+0.14+0.16}_{-0.14-0.15}$	$57.0^{+5.1+4.4}_{-4.9-4.3}$	57
49	>750	750–1500	3–4	1	$3.3^{+1.5+0.5}_{-1.3-0.5}$	$4.8^{+1.3+0.8}_{-1.2-0.8}$	$48.5^{+1.7+7.9}_{-1.7-7.3}$	$0.13^{+0.01+0.05}_{-0.01-0.05}$	$56.8^{+3.3+7.9}_{-3.0-7.4}$	61
50	>750	>1500	3–4	1	$1.0^{+1.2+0.3}_{-0.7-0.3}$	$0.77^{+0.75+0.16}_{-0.59-0.16}$	$4.40^{+0.62+0.75}_{-0.55-0.71}$	$0.03^{+0.01+0.01}_{-0.01-0.01}$	$6.2^{+2.0+0.8}_{-1.4-0.8}$	8
51	300–350	300–500	3–4	2	137^{+11+11}_{-11-11}	133^{+7+11}_{-7-11}	145^{+1+26}_{-1-26}	$9.0^{+1.1+3.9}_{-1.1-3.4}$	424^{+18+31}_{-17-31}	464
52	300–350	500–1000	3–4	2	$92.3^{+9.1+9.5}_{-9.0-9.5}$	$85.6^{+5.7+7.5}_{-5.7-7.4}$	$53.0^{+0.6+9.6}_{-0.6-9.6}$	$3.8^{+1.2+1.6}_{-1.2-1.4}$	235^{+15+16}_{-15-15}	227
53	300–350	>1000	3–4	2	$3.4^{+2.2+0.8}_{-1.7-0.8}$	$2.41^{+0.91+0.50}_{-0.78-0.50}$	$3.95^{+0.18+0.75}_{-0.17-0.73}$	$2.23^{+0.18+0.96}_{-0.18-0.86}$	$12.0^{+3.1+1.6}_{-2.5-1.5}$	17
54	350–500	350–500	3–4	2	$39.6^{+6.1+3.8}_{-5.9-3.8}$	$39.8^{+3.9+3.8}_{-3.8-3.8}$	84^{+1+15}_{-1-15}	$2.7^{+0.6+1.1}_{-0.6-1.0}$	166^{+10+16}_{-10-16}	208
55	350–500	500–1000	3–4	2	$83.9^{+8.2+7.8}_{-8.1-7.8}$	$69.4^{+4.9+5.9}_{-4.9-5.8}$	97^{+1+18}_{-1-17}	$3.1^{+0.2+1.3}_{-0.2-1.2}$	254^{+13+20}_{-13-20}	286
56	350–500	>1000	3–4	2	$6.2^{+4.0+1.0}_{-3.6-1.0}$	$3.8^{+1.1+0.6}_{-1.0-0.6}$	$6.8^{+0.2+1.3}_{-0.2-1.3}$	$0.95^{+0.16+0.41}_{-0.16-0.36}$	$17.7^{+5.2+1.8}_{-4.6-1.8}$	25
57	500–750	500–1000	3–4	2	$11.8^{+3.3+2.0}_{-3.1-2.0}$	$10.5^{+1.8+1.6}_{-1.7-1.6}$	$39.7^{+0.5+7.4}_{-0.5-7.3}$	$0.22^{+0.04+0.09}_{-0.04-0.08}$	$62.1^{+5.1+7.8}_{-4.8-7.7}$	64
58	500–750	>1000	3–4	2	$2.6^{+2.3+0.6}_{-1.6-0.6}$	$2.9^{+1.5+0.6}_{-1.5-0.6}$	$4.90^{+0.21+0.92}_{-0.21-0.91}$	$0.10^{+0.03+0.04}_{-0.03-0.04}$	$10.5^{+3.8+1.2}_{-3.1-1.2}$	13
59	>750	750–1500	3–4	2	$0.0^{+1.1+0.0}_{-0.0-0.0}$	$0.32^{+0.48+0.09}_{-0.13-0.09}$	$6.3^{+0.2+1.4}_{-0.2-1.3}$	$0.03^{+0.02+0.01}_{-0.02-0.01}$	$6.6^{+1.6+1.4}_{-0.3-1.3}$	4
60	>750	>1500	3–4	2	$0.0^{+1.1+0.0}_{-0.0-0.0}$	$0.03^{+0.46+0.01}_{-0.02-0.01}$	$0.65^{+0.09+0.15}_{-0.08-0.14}$	$0.01^{+0.01+0.01}_{-0.01-0.00}$	$0.7^{+1.6+0.1}_{-0.1-0.1}$	1
61	300–350	300–500	3–4	≥3	$6.4^{+2.8+0.7}_{-2.3-0.7}$	$10.3^{+1.9+2.7}_{-1.9-2.7}$	$5.0^{+0.0+2.8}_{-0.0-2.8}$	$0.35^{+0.18+0.42}_{-0.18-0.16}$	$22.0^{+4.7+3.9}_{-4.2-3.9}$	27
62	300–350	500–1000	3–4	≥3	$4.9^{+2.7+0.6}_{-2.2-0.6}$	$6.2^{+1.4+1.7}_{-1.3-1.7}$	$2.5^{+0.0+1.4}_{-0.0-1.4}$	$0.75^{+0.52+0.90}_{-0.52-0.24}$	$14.4^{+4.2+2.4}_{-3.6-2.2}$	20
63	300–350	>1000	3–4	≥3	$0.0^{+1.1+0.0}_{-0.0-0.0}$	$0.94^{+0.87+0.44}_{-0.74-0.44}$	$0.21^{+0.01+0.12}_{-0.01-0.12}$	$1.6^{+0.2+1.9}_{-0.2-1.4}$	$2.7^{+2.0+2.0}_{-0.8-1.5}$	4
64	350–500	350–500	3–4	≥3	$0.6^{+1.2+0.1}_{-0.6-0.0}$	$4.2^{+1.5+1.3}_{-1.4-1.3}$	$2.5^{+0.0+1.4}_{-0.0-1.4}$	$0.09^{+0.04+0.11}_{-0.04-0.05}$	$7.4^{+2.6+1.9}_{-1.9-1.9}$	8
65	350–500	500–1000	3–4	≥3	$10.2^{+6.3+2.1}_{-5.7-2.1}$	$7.0^{+1.5+1.9}_{-1.5-1.9}$	$4.3^{+0.0+2.4}_{-0.0-2.4}$	$0.78^{+0.18+0.94}_{-0.18-0.60}$	$22.3^{+7.9+3.8}_{-7.2-3.7}$	26
66	350–500	>1000	3–4	≥3	$0.0^{+1.1+0.0}_{-0.0-0.0}$	$0.21^{+0.49+0.13}_{-0.16-0.13}$	$0.36^{+0.01+0.20}_{-0.01-0.20}$	$0.54^{+0.15+0.65}_{-0.15-0.39}$	$1.1^{+1.6+0.7}_{-0.2-0.5}$	5
67	500–750	500–1000	3–4	≥3	$1.4^{+2.9+0.4}_{-1.4-0.0}$	$1.13^{+0.74+0.45}_{-0.58-0.45}$	$1.50^{+0.02+0.83}_{-0.02-0.83}$	$0.10^{+0.10+0.13}_{-0.10-0.00}$	$4.1^{+3.6+1.0}_{-2.0-0.9}$	0
68	500–750	>1000	3–4	≥3	$0.00^{+0.95+0.00}_{-0.00-0.00}$	$0.12^{+0.46+0.09}_{-0.06-0.09}$	$0.26^{+0.01+0.15}_{-0.01-0.15}$	$0.02^{+0.03+0.02}_{-0.02-0.00}$	$0.4^{+1.4+0.2}_{-0.1-0.2}$	2
69	>750	750–1500	3–4	≥3	$0.00^{+0.97+0.00}_{-0.00-0.00}$	$0.00^{+0.46+0.00}_{-0.00-0.00}$	$0.29^{+0.01+0.16}_{-0.01-0.16}$	$0.01^{+0.02+0.01}_{-0.01-0.00}$	$0.3^{+1.4+0.2}_{-0.0-0.2}$	1
70	>750	>1500	3–4	≥3	$0.0^{+1.4+0.0}_{-0.0-0.0}$	$0.00^{+0.46+0.00}_{-0.00-0.00}$	$0.04^{+0.01+0.02}_{-0.00-0.02}$	$0.01^{+0.03+0.02}_{-0.01-0.00}$	$0.0^{+1.8+0.0}_{-0.0-0.0}$	0

Table 9.3: Observed numbers of events and prefit background predictions in the $5 \leq N_{\text{jet}} \leq 6$ search regions. The first uncertainty is statistical and the second is systematic.

Bin	H_T^{miss} [GeV]	H_T [GeV]	N_{jet}	$N_{b\text{-jet}}$	Lost-e/μ	$\tau \to$ had.	$Z \to \nu\bar{\nu}$	QCD	Total pred.	Obs.
71	300–350	300–500	5–6	0	217^{+11+22}_{-11-22}	166^{+6+27}_{-6-27}	489^{+12+42}_{-12-39}	49^{+5+21}_{-5-19}	922^{+21+58}_{-21-56}	1015
72	300–350	500–1000	5–6	0	397^{+13+37}_{-13-37}	403^{+9+36}_{-9-36}	772^{+16+61}_{-15-57}	113^{+4+47}_{-4-43}	1686^{+27+93}_{-27-88}	1673
73	300–350	>1000	5–6	0	$49.6^{+4.5+5.4}_{-4.5-5.4}$	$55.1^{+3.8+8.3}_{-3.8-8.3}$	$100.0^{+6.4+8.2}_{-6.0-7.1}$	49^{+1+21}_{-1-19}	254^{+11+24}_{-10-22}	226
74	350–500	350–500	5–6	0	71^{+7+11}_{-6-11}	47^{+3+16}_{-3-16}	242^{+9+20}_{-9-19}	$12.7^{+2.3+5.3}_{-2.3-4.8}$	372^{+13+29}_{-13-28}	464
75	350–500	500–1000	5–6	0	384^{+12+33}_{-12-33}	412^{+11+32}_{-11-32}	1110^{+19+84}_{-19-78}	65^{+2+27}_{-2-25}	1971^{+30+99}_{-29-93}	2018
76	350–500	>1000	5–6	0	$76.9^{+6.4+8.9}_{-6.4-8.9}$	$72.4^{+4.8+9.3}_{-4.8-9.3}$	170^{+8+14}_{-8-12}	28^{+1+12}_{-1-11}	347^{+14+22}_{-14-21}	320
77	500–750	500–1000	5–6	0	$66.7^{+5.1+7.3}_{-5.0-7.3}$	$70.1^{+4.3+6.1}_{-4.2-6.0}$	302^{+10+23}_{-10-22}	$3.2^{+0.1+1.3}_{-0.1-1.2}$	442^{+14+25}_{-14-24}	460
78	500–750	>1000	5–6	0	$23.9^{+2.9+4.5}_{-2.9-4.5}$	$31.2^{+3.1+4.0}_{-3.1-4.0}$	$123.5^{+7.3+9.4}_{-6.9-8.9}$	$2.5^{+0.1+1.1}_{-0.1-1.0}$	181^{+10+11}_{-9-11}	170
79	>750	750–1500	5–6	0	$4.0^{+1.2+0.7}_{-1.1-0.7}$	$4.90^{+0.89+0.52}_{-0.76-0.52}$	$52.2^{+4.6+7.5}_{-4.2-6.8}$	$0.23^{+0.04+0.10}_{-0.04-0.09}$	$61.3^{+5.0+7.5}_{-4.6-6.9}$	74
80	>750	>1500	5–6	0	$0.90^{+0.61+0.19}_{-0.45-0.19}$	$1.46^{+0.67+0.16}_{-0.49-0.16}$	$16.5^{+2.9+2.7}_{-2.5-2.5}$	$0.25^{+0.06+0.11}_{-0.06-0.10}$	$19.1^{+3.2+2.7}_{-2.7-2.5}$	19
81	300–350	300–500	5–6	1	130^{+8+11}_{-8-11}	131^{+6+17}_{-6-17}	133^{+3+19}_{-3-19}	$12.8^{+2.8+5.2}_{-2.8-4.9}$	407^{+15+29}_{-15-28}	450
82	300–350	500–1000	5–6	1	290^{+11+25}_{-11-25}	302^{+8+25}_{-8-25}	218^{+4+31}_{-4-30}	41^{+4+17}_{-4-16}	851^{+20+50}_{-20-49}	781
83	300–350	>1000	5–6	1	$25.8^{+3.4+2.5}_{-3.4-2.5}$	$31.6^{+2.9+5.9}_{-2.9-5.9}$	$29.0^{+1.8+4.1}_{-1.7-4.0}$	$18.4^{+0.8+7.5}_{-0.8-7.1}$	105^{+7+11}_{-6-10}	100
84	350–500	350–500	5–6	1	$45.4^{+5.5+5.4}_{-5.4-5.4}$	32^{+3+11}_{-3-11}	$65.1^{+2.4+9.3}_{-2.3-9.1}$	$3.7^{+0.5+1.5}_{-0.5-1.4}$	146^{+9+16}_{-8-16}	160
85	350–500	500–1000	5–6	1	228^{+10+20}_{-10-20}	269^{+8+21}_{-8-21}	310^{+5+43}_{-5-42}	28^{+3+11}_{-3-11}	834^{+19+53}_{-19-52}	801
86	350–500	>1000	5–6	1	$40.5^{+5.5+4.2}_{-5.4-4.2}$	$36.0^{+3.3+4.3}_{-3.3-4.2}$	$49.4^{+2.3+7.0}_{-2.2-6.7}$	$11.9^{+0.7+4.8}_{-0.7-4.5}$	138^{+9+10}_{-9-10}	138
87	500–750	500–1000	5–6	1	$23.4^{+3.5+2.6}_{-3.4-2.6}$	$32.1^{+2.8+3.3}_{-2.8-3.3}$	84^{+3+12}_{-3-12}	$1.45^{+0.11+0.59}_{-0.11-0.55}$	141^{+7+13}_{-7-12}	135
88	500–750	>1000	5–6	1	$8.5^{+1.8+1.1}_{-1.7-1.1}$	$13.0^{+1.8+1.5}_{-1.7-1.5}$	$35.3^{+2.1+4.9}_{-2.0-4.8}$	$1.33^{+0.17+0.54}_{-0.17-0.51}$	$58.0^{+4.1+5.3}_{-3.9-5.2}$	49
89	>750	750–1500	5–6	1	$3.7^{+1.4+0.7}_{-1.2-0.7}$	$2.9^{+1.0+0.4}_{-0.9-0.4}$	$14.9^{+1.3+2.8}_{-1.2-2.6}$	$0.07^{+0.01+0.03}_{-0.01-0.03}$	$21.6^{+2.8+2.9}_{-2.5-2.7}$	16
90	>750	>1500	5–6	1	$1.06^{+0.74+0.26}_{-0.56-0.26}$	$1.16^{+0.73+0.18}_{-0.57-0.18}$	$4.79^{+0.85+0.96}_{-0.73-0.92}$	$0.16^{+0.07+0.07}_{-0.07-0.06}$	$7.2^{+1.7+1.0}_{-1.3-1.0}$	6
91	300–350	300–500	5–6	2	$60.1^{+7.1+6.0}_{-7.0-6.0}$	$50.2^{+3.3+4.9}_{-3.3-4.9}$	$23.8^{+0.6+7.1}_{-0.6-7.1}$	$2.9^{+0.9+1.1}_{-0.9-1.1}$	137^{+10+11}_{-10-11}	143
92	300–350	500–1000	5–6	2	137^{+9+13}_{-9-13}	160^{+6+14}_{-6-14}	39^{+1+12}_{-1-11}	$11.8^{+1.8+4.6}_{-1.8-4.5}$	347^{+15+22}_{-15-22}	332
93	300–350	>1000	5–6	2	$16.9^{+3.8+2.0}_{-3.7-2.0}$	$15.9^{+2.1+2.1}_{-2.1-2.1}$	$5.1^{+0.3+1.5}_{-0.3-1.5}$	$5.6^{+0.4+2.2}_{-0.4-2.2}$	$43.5^{+5.9+3.9}_{-5.8-3.9}$	36
94	350–500	350–500	5–6	2	$13.3^{+3.1+1.9}_{-2.9-1.9}$	$7.0^{+1.1+2.3}_{-1.0-2.3}$	$11.7^{+0.4+3.5}_{-0.4-3.5}$	$1.02^{+0.54+0.40}_{-0.54-0.39}$	$32.9^{+4.3+4.6}_{-4.0-4.6}$	28
95	350–500	500–1000	5–6	2	$107.5^{+7.6+9.6}_{-7.6-9.6}$	$121.2^{+5.8+9.9}_{-5.8-9.8}$	55^{+1+16}_{-1-16}	$5.9^{+1.0+2.3}_{-1.0-2.2}$	290^{+14+22}_{-13-21}	288
96	350–500	>1000	5–6	2	$14.2^{+2.8+1.8}_{-2.7-1.8}$	$15.7^{+2.2+2.0}_{-2.1-2.0}$	$8.7^{+0.4+2.6}_{-0.4-2.6}$	$3.2^{+0.1+1.2}_{-0.1-1.2}$	$41.8^{+5.0+4.0}_{-4.8-3.9}$	44
97	500–750	500–1000	5–6	2	$8.4^{+2.3+1.1}_{-2.2-1.1}$	$8.3^{+1.3+1.0}_{-1.2-1.0}$	$15.0^{+0.5+4.4}_{-0.5-4.4}$	$0.34^{+0.05+0.13}_{-0.05-0.13}$	$32.1^{+3.7+4.7}_{-3.4-4.7}$	35
98	500–750	>1000	5–6	2	$2.1^{+1.3+0.3}_{-1.0-0.3}$	$4.0^{+1.1+0.6}_{-1.0-0.6}$	$6.2^{+0.4+1.9}_{-0.3-1.8}$	$0.16^{+0.05+0.06}_{-0.05-0.06}$	$12.5^{+2.4+2.0}_{-2.0-2.0}$	18
99	>750	750–1500	5–6	2	$0.74^{+0.87+0.22}_{-0.53-0.22}$	$0.68^{+0.64+0.16}_{-0.45-0.16}$	$2.64^{+0.23+0.85}_{-0.21-0.83}$	$0.05^{+0.05+0.02}_{-0.05-0.00}$	$4.1^{+1.5+0.9}_{-1.0-0.9}$	8
100	>750	>1500	5–6	2	$0.77^{+0.65+0.24}_{-0.45-0.24}$	$1.07^{+0.72+0.33}_{-0.56-0.33}$	$0.84^{+0.15+0.28}_{-0.13-0.27}$	$0.03^{+0.03+0.01}_{-0.03-0.00}$	$2.7^{+1.4+0.5}_{-1.0-0.5}$	3
101	300–350	300–500	5–6	≥3	$2.8^{+1.5+0.3}_{-1.2-0.3}$	$5.1^{+1.0+0.8}_{-0.9-0.8}$	$2.0^{+0.0+1.1}_{-0.0-1.1}$	$0.50^{+0.37+0.57}_{-0.37-0.13}$	$10.4^{+2.5+1.5}_{-2.1-1.4}$	18
102	300–350	500–1000	5–6	≥3	$17.0^{+3.2+1.6}_{-3.1-1.6}$	$23.5^{+2.4+3.2}_{-2.3-3.2}$	$4.2^{+0.1+2.3}_{-0.1-2.3}$	$3.9^{+2.3+4.5}_{-2.3-1.6}$	$48.7^{+6.0+6.2}_{-5.9-4.5}$	44
103	300–350	>1000	5–6	≥3	$4.4^{+2.1+0.6}_{-1.8-0.6}$	$2.50^{+0.86+0.47}_{-0.73-0.47}$	$0.65^{+0.04+0.35}_{-0.04-0.35}$	$3.3^{+0.4+3.7}_{-0.4-2.8}$	$10.8^{+3.0+3.8}_{-2.6-3.0}$	6
104	350–500	350–500	5–6	≥3	$0.8^{+1.7+0.2}_{-0.8-0.0}$	$1.14^{+0.75+0.33}_{-0.59-0.33}$	$0.87^{+0.03+0.47}_{-0.03-0.47}$	$0.18^{+0.08+0.21}_{-0.08-0.10}$	$3.0^{+2.4+0.6}_{-1.4-0.6}$	4
105	350–500	500–1000	5–6	≥3	$15.2^{+2.6+1.5}_{-2.6-1.5}$	$17.6^{+2.2+2.7}_{-2.1-2.7}$	$5.7^{+0.1+3.1}_{-0.1-3.1}$	$1.7^{+0.1+1.9}_{-0.1-1.6}$	$40.2^{+4.8+4.8}_{-4.7-4.6}$	34
106	350–500	>1000	5–6	≥3	$1.9^{+1.1+0.3}_{-0.8-0.3}$	$3.8^{+1.1+0.7}_{-1.0-0.7}$	$1.14^{+0.05+0.62}_{-0.05-0.62}$	$2.4^{+0.3+2.7}_{-0.3-2.1}$	$9.2^{+2.2+2.8}_{-1.9-2.3}$	8
107	500–750	500–1000	5–6	≥3	$1.8^{+1.1+0.3}_{-0.8-0.3}$	$1.71^{+0.77+0.67}_{-0.61-0.67}$	$1.48^{+0.05+0.81}_{-0.05-0.80}$	$0.20^{+0.04+0.23}_{-0.04-0.17}$	$5.2^{+1.8+1.1}_{-1.5-1.1}$	4
108	500–750	>1000	5–6	≥3	$1.13^{+0.96+0.25}_{-0.66-0.25}$	$0.94^{+0.67+0.27}_{-0.49-0.27}$	$0.73^{+0.04+0.40}_{-0.04-0.40}$	$0.11^{+0.03+0.12}_{-0.03-0.08}$	$2.9^{+1.6+0.6}_{-1.1-0.6}$	2
109	>750	750–1500	5–6	≥3	$0.00^{+0.72+0.00}_{-0.00-0.00}$	$0.07^{+0.46+0.04}_{-0.06-0.04}$	$0.31^{+0.03+0.17}_{-0.03-0.17}$	$0.02^{+0.04+0.03}_{-0.02-0.00}$	$0.4^{+1.2+0.2}_{-0.1-0.2}$	0
110	>750	>1500	5–6	≥3	$0.00^{+0.63+0.00}_{-0.00-0.00}$	$0.03^{+0.46+0.01}_{-0.02-0.01}$	$0.11^{+0.02+0.06}_{-0.02-0.06}$	$0.00^{+0.02+0.01}_{-0.00-0.00}$	$0.1^{+1.1+0.1}_{-0.0-0.1}$	1

Table 9.4: Observed numbers of events and prefit background predictions in the $7 \leq N_{\text{jet}} \leq 8$ search regions. The first uncertainty is statistical and the second is systematic.

Bin	H_T^{miss} [GeV]	H_T [GeV]	N_{jet}	$N_{b\text{-jet}}$	Lost-e/μ	$\tau \to$ had.	$Z \to \nu\bar{\nu}$	QCD	Total pred.	Obs.
111	300–350	500–1000	7–8	0	$48.0^{+3.9+5.4}_{-3.8-5.4}$	$60.8^{+3.4+6.0}_{-3.4-6.0}$	76^{+5+11}_{-5-10}	30^{+2+12}_{-2-11}	215^{+9+18}_{-9-17}	218
112	300–350	>1000	7–8	0	$21.2^{+2.9+2.3}_{-2.9-2.3}$	$20.3^{+2.2+2.8}_{-2.1-2.8}$	$23.9^{+3.3+2.8}_{-2.9-2.5}$	$20.5^{+0.5+8.5}_{-0.5-7.8}$	$85.9^{+6.1+9.6}_{-5.8-9.0}$	85
113	350–500	500–1000	7–8	0	$43.2^{+3.9+4.9}_{-3.9-4.9}$	$54.2^{+3.6+5.7}_{-3.5-5.7}$	89^{+6+11}_{-5-10}	$14.3^{+1.9+5.9}_{-1.9-5.4}$	201^{+10+14}_{-9-14}	215
114	350–500	>1000	7–8	0	$22.5^{+2.8+2.7}_{-2.7-2.7}$	$23.3^{+2.5+2.3}_{-2.4-2.3}$	$48.3^{+4.7+5.4}_{-4.3-4.8}$	$12.6^{+0.7+5.2}_{-0.7-4.8}$	$106.7^{+7.1+8.3}_{-6.7-7.7}$	75
115	500–750	500–1000	7–8	0	$6.9^{+1.8+1.4}_{-1.7-1.4}$	$4.96^{+0.95+0.77}_{-0.84-0.77}$	$26.5^{+3.6+3.3}_{-3.2-3.0}$	$0.88^{+0.10+0.36}_{-0.10-0.34}$	$39.2^{+4.5+3.7}_{-4.1-3.5}$	34
116	500–750	>1000	7–8	0	$5.4^{+1.1+0.9}_{-1.0-0.9}$	$9.9^{+1.6+1.7}_{-1.5-1.7}$	$27.2^{+3.7+3.1}_{-3.2-2.8}$	$1.56^{+0.12+0.64}_{-0.12-0.59}$	$44.1^{+4.5+3.7}_{-4.1-3.5}$	38
117	>750	750–1500	7–8	0	$1.26^{+0.70+0.50}_{-0.58-0.50}$	$1.44^{+0.74+0.24}_{-0.57-0.24}$	$3.6^{+1.4+0.7}_{-1.0-0.6}$	$0.07^{+0.02+0.03}_{-0.02-0.03}$	$6.4^{+2.0+0.9}_{-1.5-0.8}$	5
118	>750	>1500	7–8	0	$0.69^{+0.47+0.16}_{-0.35-0.16}$	$1.03^{+0.69+0.15}_{-0.51-0.15}$	$1.5^{+1.2+0.3}_{-0.7-0.3}$	$0.07^{+0.01+0.03}_{-0.01-0.03}$	$3.3^{+1.7+0.4}_{-1.1-0.4}$	5
119	300–350	500–1000	7–8	1	$64.7^{+5.1+6.4}_{-5.1-6.4}$	$77.0^{+3.9+7.5}_{-3.8-7.4}$	$31.7^{+2.1+8.6}_{-1.9-8.4}$	$11.2^{+0.5+4.7}_{-0.5-4.3}$	184^{+9+14}_{-9-14}	146
120	300–350	>1000	7–8	1	$16.3^{+2.4+1.7}_{-2.4-1.7}$	$19.9^{+2.2+2.1}_{-2.1-2.1}$	$10.3^{+1.4+2.7}_{-1.2-2.6}$	$8.3^{+0.2+3.5}_{-0.2-3.2}$	$54.8^{+4.8+5.2}_{-4.7-5.0}$	68
121	350–500	500–1000	7–8	1	$46.9^{+4.4+5.0}_{-4.4-5.0}$	$58.6^{+3.7+5.7}_{-3.7-5.7}$	$37.0^{+2.4+9.7}_{-2.2-9.5}$	$7.5^{+0.4+3.2}_{-0.4-2.9}$	150^{+8+13}_{-8-12}	113
122	350–500	>1000	7–8	1	$19.5^{+2.5+2.1}_{-2.4-2.1}$	$19.5^{+2.3+2.0}_{-2.3-2.0}$	$21.0^{+2.0+5.4}_{-1.9-5.3}$	$5.3^{+0.5+2.2}_{-0.5-2.0}$	$65.3^{+5.2+6.5}_{-5.1-6.4}$	67
123	500–750	500–1000	7–8	1	$7.6^{+2.0+1.4}_{-1.9-1.4}$	$5.5^{+1.1+0.8}_{-1.1-0.8}$	$11.5^{+1.6+3.0}_{-1.4-3.0}$	$0.36^{+0.04+0.15}_{-0.04-0.14}$	$24.9^{+3.5+3.4}_{-3.3-3.4}$	19
124	500–750	>1000	7–8	1	$9.3^{+2.1+1.3}_{-2.0-1.3}$	$7.5^{+1.5+0.8}_{-1.4-0.8}$	$11.4^{+1.5+3.0}_{-1.4-2.9}$	$0.98^{+0.12+0.41}_{-0.12-0.37}$	$29.2^{+3.9+3.3}_{-3.7-3.3}$	22
125	>750	750–1500	7–8	1	$0.14^{+0.30+0.05}_{-0.14-0.00}$	$0.44^{+0.51+0.10}_{-0.22-0.10}$	$1.48^{+0.56+0.44}_{-0.42-0.43}$	$0.07^{+0.03+0.03}_{-0.03-0.03}$	$2.14^{+0.99+0.46}_{-0.56-0.45}$	4
126	>750	>1500	7–8	1	$0.00^{+0.47+0.00}_{-0.00-0.00}$	$0.14^{+0.47+0.02}_{-0.08-0.02}$	$0.70^{+0.55+0.22}_{-0.34-0.21}$	$0.03^{+0.01+0.01}_{-0.01-0.01}$	$0.9^{+1.1+0.2}_{-0.3-0.2}$	6
127	300–350	500–1000	7–8	2	$34.7^{+3.5+3.6}_{-3.5-3.6}$	$47.7^{+3.0+4.4}_{-3.0-4.4}$	$8.1^{+0.5+3.6}_{-0.5-3.5}$	$5.3^{+0.5+2.1}_{-0.5-2.1}$	$95.8^{+6.6+7.1}_{-6.5-7.0}$	95
128	300–350	>1000	7–8	2	$9.0^{+2.1+1.2}_{-2.1-1.2}$	$10.8^{+1.4+1.3}_{-1.4-1.3}$	$2.4^{+0.3+1.0}_{-0.3-1.0}$	$3.2^{+0.1+1.3}_{-0.1-1.3}$	$25.4^{+3.6+2.4}_{-3.4-2.4}$	26
129	350–500	500–1000	7–8	2	$26.2^{+3.0+2.9}_{-3.0-2.9}$	$31.0^{+2.5+3.3}_{-2.5-3.2}$	$9.6^{+0.6+4.1}_{-0.6-4.1}$	$2.5^{+0.2+1.0}_{-0.2-1.0}$	$69.3^{+5.6+6.1}_{-5.5-6.1}$	84
130	350–500	>1000	7–8	2	$13.3^{+2.5+1.5}_{-2.4-1.5}$	$13.3^{+1.8+1.3}_{-1.7-1.3}$	$4.7^{+0.5+2.0}_{-0.4-2.0}$	$1.95^{+0.13+0.78}_{-0.13-0.75}$	$33.3^{+4.3+3.0}_{-4.2-2.9}$	35
131	500–750	500–1000	7–8	2	$2.5^{+1.4+0.5}_{-1.2-0.5}$	$0.86^{+0.50+0.21}_{-0.18-0.21}$	$2.6^{+0.3+1.1}_{-0.3-1.1}$	$0.10^{+0.01+0.04}_{-0.01-0.04}$	$6.0^{+1.9+1.3}_{-1.4-1.3}$	7
132	500–750	>1000	7–8	2	$6.0^{+2.3+1.0}_{-2.2-1.0}$	$3.3^{+1.0+0.6}_{-0.9-0.6}$	$2.9^{+0.4+1.2}_{-0.3-1.2}$	$0.22^{+0.06+0.09}_{-0.06-0.08}$	$12.4^{+3.4+1.7}_{-3.1-1.7}$	12
133	>750	750–1500	7–8	2	$0.16^{+0.34+0.08}_{-0.16-0.00}$	$0.44^{+0.56+0.15}_{-0.32-0.15}$	$0.39^{+0.15+0.18}_{-0.11-0.18}$	$0.03^{+0.01+0.01}_{-0.01-0.01}$	$1.03^{+0.91+0.25}_{-0.49-0.23}$	2
134	>750	>1500	7–8	2	$0.53^{+0.62+0.20}_{-0.38-0.20}$	$0.61^{+0.57+0.22}_{-0.33-0.22}$	$0.13^{+0.10+0.06}_{-0.06-0.06}$	$0.06^{+0.02+0.02}_{-0.02-0.02}$	$1.3^{+1.2+0.3}_{-0.7-0.3}$	2
135	300–350	500–1000	7–8	≥3	$8.1^{+1.8+1.0}_{-1.7-1.0}$	$9.4^{+1.4+1.3}_{-1.3-1.3}$	$4.1^{+0.3+2.3}_{-0.2-2.3}$	$2.9^{+0.6+3.3}_{-0.6-2.3}$	$24.6^{+3.2+4.3}_{-3.1-3.7}$	12
136	300–350	>1000	7–8	≥3	$4.7^{+2.0+0.7}_{-1.8-0.7}$	$5.4^{+1.2+0.8}_{-1.1-0.8}$	$1.51^{+0.21+0.85}_{-0.18-0.84}$	$2.4^{+0.3+2.7}_{-0.3-2.1}$	$13.9^{+3.2+3.0}_{-2.9-2.5}$	8
137	350–500	500–1000	7–8	≥3	$5.9^{+1.9+0.8}_{-1.7-0.8}$	$7.4^{+1.4+1.2}_{-1.3-1.2}$	$4.7^{+0.3+2.7}_{-0.3-2.7}$	$1.2^{+0.1+1.3}_{-0.1-1.1}$	$19.2^{+3.2+3.3}_{-3.1-3.2}$	16
138	350–500	>1000	7–8	≥3	$2.6^{+1.1+0.3}_{-1.0-0.3}$	$4.8^{+1.3+0.7}_{-1.2-0.7}$	$3.1^{+0.3+1.8}_{-0.3-1.8}$	$2.1^{+0.3+2.3}_{-0.3-1.8}$	$12.6^{+2.5+3.0}_{-2.2-2.6}$	8
139	500–750	500–1000	7–8	≥3	$0.23^{+0.48+0.08}_{-0.23-0.00}$	$0.30^{+0.48+0.10}_{-0.13-0.10}$	$1.70^{+0.23+0.96}_{-0.20-0.96}$	$0.11^{+0.04+0.12}_{-0.04-0.08}$	$2.34^{+0.99+0.98}_{-0.41-0.96}$	3
140	500–750	>1000	7–8	≥3	$3.4^{+2.4+0.7}_{-2.1-0.7}$	$1.59^{+0.83+0.49}_{-0.69-0.49}$	$1.51^{+0.20+0.85}_{-0.18-0.85}$	$0.22^{+0.08+0.24}_{-0.08-0.14}$	$6.7^{+3.2+1.2}_{-2.7-1.2}$	4
141	>750	750–1500	7–8	≥3	$0.00^{+0.56+0.00}_{-0.00-0.00}$	$0.05^{+0.46+0.02}_{-0.03-0.02}$	$0.19^{+0.07+0.11}_{-0.05-0.11}$	$0.03^{+0.04+0.03}_{-0.03-0.00}$	$0.3^{+1.0+0.1}_{-0.1-0.1}$	0
142	>750	>1500	7–8	≥3	$0.00^{+0.72+0.00}_{-0.00-0.00}$	$0.04^{+0.46+0.02}_{-0.02-0.02}$	$0.12^{+0.10+0.07}_{-0.06-0.07}$	$0.01^{+0.03+0.01}_{-0.01-0.00}$	$0.2^{+1.2+0.1}_{-0.1-0.1}$	0

Table 9.5: Observed numbers of events and prefit background predictions in the $N_{\text{jet}} \geq 9$ search regions. The first uncertainty is statistical and the second is systematic.

Bin	H_T^{miss} [GeV]	H_T [GeV]	N_{jet}	$N_{b\text{-jet}}$	Lost-e/μ	$\tau \to$ had.	$Z \to \nu\bar{\nu}$	QCD	Total pred.	Obs.
143	300–350	500–1000	≥9	0	$6.2^{+2.7+1.7}_{-2.6-1.7}$	$3.46^{+0.89+0.59}_{-0.77-0.59}$	$2.6^{+1.2+0.7}_{-0.9-0.7}$	$2.9^{+0.3+1.3}_{-0.3-1.1}$	$15.1^{+3.8+2.3}_{-3.5-2.2}$	7
144	300–350	>1000	≥9	0	$3.5^{+1.2+0.6}_{-1.1-0.6}$	$4.6^{+1.0+0.6}_{-0.9-0.6}$	$3.0^{+1.4+0.6}_{-1.0-0.6}$	$4.2^{+0.3+1.9}_{-0.3-1.6}$	$15.2^{+2.7+2.1}_{-2.3-1.9}$	12
145	350–500	500–1000	≥9	0	$2.39^{+0.99+0.69}_{-0.89-0.69}$	$2.39^{+0.86+0.48}_{-0.73-0.48}$	$2.9^{+1.3+0.7}_{-0.9-0.6}$	$0.97^{+0.08+0.43}_{-0.08-0.37}$	$8.6^{+2.3+1.2}_{-1.9-1.1}$	6
146	350–500	>1000	≥9	0	$3.7^{+1.1+0.6}_{-1.1-0.6}$	$4.6^{+1.0+0.6}_{-0.9-0.6}$	$5.5^{+1.9+1.0}_{-1.5-0.9}$	$3.1^{+0.2+1.4}_{-0.2-1.2}$	$17.0^{+2.9+1.9}_{-2.5-1.7}$	13
147	500–750	500–1000	≥9	0	$0.15^{+0.32+0.10}_{-0.15-0.00}$	$0.35^{+0.55+0.12}_{-0.30-0.12}$	$1.0^{+1.3+0.4}_{-0.7-0.4}$	$0.10^{+0.05+0.04}_{-0.05-0.04}$	$1.6^{+1.6+0.5}_{-0.8-0.4}$	2
148	500–750	>1000	≥9	0	$0.98^{+0.50+0.26}_{-0.41-0.26}$	$1.98^{+0.74+0.30}_{-0.58-0.30}$	$3.5^{+1.6+0.7}_{-1.1-0.7}$	$0.47^{+0.05+0.21}_{-0.05-0.18}$	$6.9^{+2.0+0.8}_{-1.5-0.8}$	11
149	>750	750–1500	≥9	0	$0.00^{+0.44+0.00}_{-0.00-0.00}$	$0.00^{+0.46+0.00}_{-0.00-0.00}$	$0.00^{+0.64+0.00}_{-0.00-0.00}$	$0.01^{+0.02+0.00}_{-0.01-0.00}$	$0.0^{+1.1+0.0}_{-0.0-0.0}$	0
150	>750	>1500	≥9	0	$0.23^{+0.27+0.16}_{-0.17-0.16}$	$0.28^{+0.50+0.08}_{-0.21-0.08}$	$0.00^{+0.82+0.00}_{-0.00-0.00}$	$0.05^{+0.03+0.02}_{-0.03-0.02}$	$0.6^{+1.1+0.2}_{-0.4-0.2}$	1
151	300–350	500–1000	≥9	1	$6.5^{+1.8+1.1}_{-1.7-1.1}$	$4.57^{+0.93+0.77}_{-0.81-0.77}$	$1.83^{+0.84+0.68}_{-0.60-0.74}$	$1.02^{+0.06+0.42}_{-0.06-0.40}$	$13.9^{+2.8+1.5}_{-2.6-1.6}$	25
152	300–350	>1000	≥9	1	$5.7^{+1.6+0.7}_{-1.5-0.7}$	$7.3^{+1.3+1.1}_{-1.2-1.1}$	$2.08^{+0.95+0.69}_{-0.68-0.77}$	$2.43^{+0.06+0.99}_{-0.06-0.94}$	$17.5^{+3.0+1.8}_{-2.8-1.8}$	20
153	350–500	500–1000	≥9	1	$2.92^{+0.94+0.57}_{-0.84-0.57}$	$2.96^{+0.77+0.60}_{-0.61-0.60}$	$2.00^{+0.91+0.71}_{-0.65-0.78}$	$0.53^{+0.05+0.22}_{-0.05-0.21}$	$8.4^{+1.9+1.1}_{-1.6-1.2}$	8
154	350–500	>1000	≥9	1	$5.4^{+1.4+0.7}_{-1.3-0.7}$	$7.7^{+1.4+1.1}_{-1.3-1.1}$	$3.9^{+1.3+1.3}_{-1.0-1.4}$	$1.48^{+0.05+0.60}_{-0.05-0.57}$	$18.4^{+3.1+1.9}_{-2.8-2.0}$	14
155	500–750	500–1000	≥9	1	$0.14^{+0.30+0.08}_{-0.14-0.00}$	$0.24^{+0.49+0.21}_{-0.18-0.16}$	$0.71^{+0.94+0.35}_{-0.46-0.36}$	$0.03^{+0.03+0.01}_{-0.03-0.00}$	$1.1^{+1.2+0.4}_{-0.6-0.4}$	1
156	500–750	>1000	≥9	1	$0.68^{+0.58+0.12}_{-0.41-0.12}$	$1.20^{+0.64+0.21}_{-0.44-0.21}$	$2.4^{+1.1+0.8}_{-0.8-0.9}$	$0.20^{+0.02+0.08}_{-0.02-0.07}$	$4.5^{+1.6+0.8}_{-1.2-0.9}$	4
157	>750	750–1500	≥9	1	$0.00^{+0.73+0.00}_{-0.00-0.00}$	$0.04^{+0.46+0.02}_{-0.04-0.00}$	$0.00^{+0.45+0.00}_{-0.00-0.00}$	$0.01^{+0.01+0.00}_{-0.01-0.00}$	$0.1^{+1.3+0.0}_{-0.0-0.0}$	0
158	>750	>1500	≥9	1	$0.13^{+0.27+0.06}_{-0.13-0.00}$	$0.03^{+0.46+0.01}_{-0.02-0.01}$	$0.00^{+0.57+0.00}_{-0.00-0.00}$	$0.02^{+0.01+0.01}_{-0.01-0.01}$	$0.18^{+0.93+0.06}_{-0.15-0.01}$	0
159	300–350	500–1000	≥9	2	$4.1^{+1.3+0.7}_{-1.2-0.7}$	$4.68^{+0.92+0.85}_{-0.80-0.85}$	$0.64^{+0.29+0.34}_{-0.21-0.36}$	$0.40^{+0.06+0.24}_{-0.06-0.21}$	$9.8^{+2.2+1.2}_{-2.0-1.2}$	13
160	300–350	>1000	≥9	2	$5.2^{+1.6+0.7}_{-1.5-0.7}$	$5.5^{+1.2+1.0}_{-1.1-1.0}$	$0.73^{+0.33+0.37}_{-0.24-0.39}$	$1.32^{+0.15+0.68}_{-0.15-0.58}$	$12.7^{+2.8+1.4}_{-2.6-1.4}$	10
161	350–500	500–1000	≥9	2	$3.01^{+0.91+0.63}_{-0.82-0.63}$	$4.7^{+1.1+0.9}_{-1.0-0.9}$	$0.70^{+0.32+0.36}_{-0.23-0.39}$	$0.30^{+0.08+0.14}_{-0.08-0.12}$	$8.7^{+2.0+1.1}_{-1.8-1.1}$	4
162	350–500	>1000	≥9	2	$4.4^{+1.1+0.6}_{-1.1-0.6}$	$6.3^{+1.4+0.8}_{-1.3-0.8}$	$1.35^{+0.47+0.67}_{-0.36-0.72}$	$0.63^{+0.03+0.32}_{-0.03-0.27}$	$12.7^{+2.6+1.3}_{-2.4-1.3}$	12
163	500–750	500–1000	≥9	2	$0.00^{+0.39+0.00}_{-0.00-0.00}$	$0.35^{+0.49+0.17}_{-0.18-0.17}$	$0.25^{+0.33+0.15}_{-0.16-0.16}$	$0.01^{+0.01+0.01}_{-0.01-0.00}$	$0.61^{+0.95+0.23}_{-0.24-0.23}$	0
164	500–750	>1000	≥9	2	$2.0^{+1.1+0.4}_{-0.9-0.4}$	$1.95^{+0.87+0.45}_{-0.73-0.45}$	$0.84^{+0.39+0.43}_{-0.28-0.46}$	$0.09^{+0.02+0.04}_{-0.02-0.04}$	$4.9^{+2.0+0.7}_{-1.7-0.7}$	7
165	>750	750–1500	≥9	2	$0.00^{+0.60+0.00}_{-0.00-0.00}$	$0.01^{+0.46+0.01}_{-0.00-0.00}$	$0.00^{+0.16+0.00}_{-0.00-0.00}$	$0.00^{+0.01+0.00}_{-0.00-0.00}$	$0.0^{+1.1+0.0}_{-0.0-0.0}$	0
166	>750	>1500	≥9	2	$0.00^{+0.38+0.00}_{-0.00-0.00}$	$0.00^{+0.46+0.00}_{-0.00-0.00}$	$0.00^{+0.20+0.00}_{-0.00-0.00}$	$0.01^{+0.02+0.00}_{-0.01-0.00}$	$0.01^{+0.87+0.00}_{-0.01-0.00}$	0
167	300–350	500–1000	≥9	≥3	$1.06^{+0.63+0.27}_{-0.50-0.27}$	$1.06^{+0.57+0.29}_{-0.34-0.29}$	$0.37^{+0.17+0.26}_{-0.12-0.28}$	$0.47^{+0.13+0.56}_{-0.13-0.34}$	$3.0^{+1.2+0.7}_{-0.9-0.6}$	1
168	300–350	>1000	≥9	≥3	$3.5^{+1.7+0.5}_{-1.5-0.5}$	$2.6^{+1.0+0.7}_{-0.9-0.7}$	$0.42^{+0.19+0.29}_{-0.14-0.31}$	$2.1^{+0.3+2.4}_{-0.3-1.8}$	$8.6^{+2.7+2.6}_{-2.4-2.0}$	4
169	350–500	500–1000	≥9	≥3	$1.03^{+0.60+0.30}_{-0.47-0.30}$	$1.58^{+0.71+0.43}_{-0.55-0.43}$	$0.40^{+0.18+0.28}_{-0.13-0.31}$	$0.10^{+0.03+0.11}_{-0.03-0.07}$	$3.1^{+1.3+0.6}_{-1.0-0.6}$	3
170	350–500	>1000	≥9	≥3	$0.81^{+0.56+0.14}_{-0.41-0.14}$	$0.96^{+0.54+0.16}_{-0.27-0.16}$	$0.77^{+0.27+0.53}_{-0.20-0.58}$	$1.3^{+0.2+1.5}_{-0.2-1.1}$	$3.8^{+1.1+1.6}_{-0.7-1.3}$	2
171	500–750	500–1000	≥9	≥3	$0.00^{+0.43+0.00}_{-0.00-0.00}$	$0.03^{+0.46+0.03}_{-0.02-0.03}$	$0.14^{+0.19+0.11}_{-0.09-0.11}$	$0.01^{+0.02+0.01}_{-0.01-0.00}$	$0.18^{+0.91+0.11}_{-0.09-0.11}$	0
172	500–750	>1000	≥9	≥3	$0.00^{+0.48+0.00}_{-0.00-0.00}$	$0.53^{+0.56+0.13}_{-0.31-0.13}$	$0.48^{+0.22+0.33}_{-0.16-0.37}$	$0.13^{+0.14+0.15}_{-0.13-0.00}$	$1.1^{+1.1+0.4}_{-0.4-0.4}$	3
173	>750	750–1500	≥9	≥3	$0.00^{+0.50+0.00}_{-0.00-0.00}$	$0.00^{+0.46+0.00}_{-0.00-0.00}$	$0.00^{+0.09+0.00}_{-0.00-0.00}$	$0.01^{+0.05+0.02}_{-0.01-0.00}$	$0.01^{+0.97+0.02}_{-0.01-0.00}$	0
174	>750	>1500	≥9	≥3	$0.00^{+0.42+0.00}_{-0.00-0.00}$	$0.00^{+0.46+0.00}_{-0.00-0.00}$	$0.00^{+0.11+0.00}_{-0.00-0.00}$	$0.02^{+0.05+0.02}_{-0.02-0.00}$	$0.02^{+0.89+0.02}_{-0.02-0.00}$	0

Table 9.6: Observed numbers of events and pre-fit background predictions in the aggregate search regions. The first uncertainty is statistical and the second is systematic.

Bin	H_T^{miss} [GeV]	H_T [GeV]	N_{jet}	$N_{b\text{-jet}}$	Lost-e/μ	$\tau \to$ had.	$Z \to \nu\bar{\nu}$	QCD	Total pred.	Obs.
1	>500	>500	≥2	0	842^{+25+48}_{-25-46}	753^{+16+65}_{-16-65}	$5968^{+48+360}_{-47-350}$	$21.4^{+0.6+8.5}_{-0.6-7.1}$	$7584^{+63+370}_{-62-360}$	7838
2	>750	>1500	≥3	0	$4.8^{+2.2+0.6}_{-1.6-0.6}$	$4.2^{+1.3+0.3}_{-0.9-0.3}$	$45.8^{+5.1+5.2}_{-4.3-4.9}$	$0.47^{+0.06+0.18}_{-0.06-0.16}$	$55.2^{+6.2+5.3}_{-5.0-4.9}$	71
3	>500	>500	≥5	0	$111.0^{+6.4+8.3}_{-6.3-7.9}$	$127.6^{+5.9+8.5}_{-5.7-8.6}$	558^{+15+36}_{-14-34}	$9.4^{+0.2+3.5}_{-0.2-3.1}$	806^{+19+38}_{-18-37}	819
4	>750	>1500	≥5	0	$1.82^{+0.82+0.26}_{-0.59-0.21}$	$2.8^{+1.1+0.2}_{-0.7-0.2}$	$18.1^{+3.3+2.7}_{-2.6-2.6}$	$0.37^{+0.06+0.15}_{-0.06-0.13}$	$23.0^{+3.8+2.7}_{-2.9-2.6}$	25
5	>750	>1500	≥9	0	$0.23^{+0.27+0.14}_{-0.17-0.07}$	$0.28^{+0.50+0.08}_{-0.21-0.07}$	$0.00^{+0.82+0.00}_{-0.00-0.00}$	$0.05^{+0.03+0.02}_{-0.03-0.02}$	$0.6^{+1.1+0.2}_{-0.4-0.1}$	1
6	>500	>500	≥2	≥2	$46.9^{+8.9+3.1}_{-5.9-3.0}$	$44.0^{+4.4+3.2}_{-3.4-3.2}$	102^{+2+14}_{-1-14}	$2.5^{+0.3+1.5}_{-0.2-1.3}$	196^{+13+15}_{-9-15}	216
7	>750	>750	≥3	≥1	$11.5^{+4.1+1.0}_{-2.2-0.9}$	$13.7^{+3.0+1.2}_{-2.0-1.2}$	87^{+3+10}_{-3-10}	$0.87^{+0.15+0.34}_{-0.11-0.31}$	113^{+8+10}_{-5-10}	123
8	>500	>500	≥5	≥3	$6.6^{+3.3+0.6}_{-2.3-0.6}$	$5.3^{+1.9+0.9}_{-1.1-0.9}$	$6.8^{+0.5+2.8}_{-0.3-2.8}$	$0.87^{+0.20+0.96}_{-0.17-0.70}$	$19.5^{+5.2+3.2}_{-3.4-3.1}$	17
9	>750	>1500	≥5	≥2	$1.3^{+1.4+0.2}_{-0.6-0.2}$	$1.8^{+1.3+0.4}_{-0.7-0.4}$	$1.20^{+0.41+0.33}_{-0.19-0.33}$	$0.13^{+0.07+0.06}_{-0.04-0.05}$	$4.4^{+2.8+0.6}_{-1.3-0.6}$	6
10	>750	>750	≥9	≥3	$0.00^{+0.66+0.00}_{-0.00-0.00}$	$0.00^{+0.65+0.00}_{-0.00-0.00}$	$0.00^{+0.15+0.00}_{-0.00-0.00}$	$0.03^{+0.07+0.04}_{-0.02-0.01}$	$0.0^{+1.3+0.0}_{-0.0-0.0}$	0
11	>300	>300	≥7	≥1	328^{+12+21}_{-12-20}	380^{+10+22}_{-9-22}	193^{+8+38}_{-6-38}	69^{+1+29}_{-1-26}	969^{+23+57}_{-22-55}	890
12	>750	>750	≥5	≥1	$7.2^{+2.8+0.8}_{-1.6-0.7}$	$7.7^{+2.4+0.8}_{-1.4-0.8}$	$26.6^{+2.4+3.9}_{-1.8-3.7}$	$0.65^{+0.14+0.26}_{-0.11-0.23}$	$42.2^{+5.7+4.0}_{-3.5-3.9}$	48

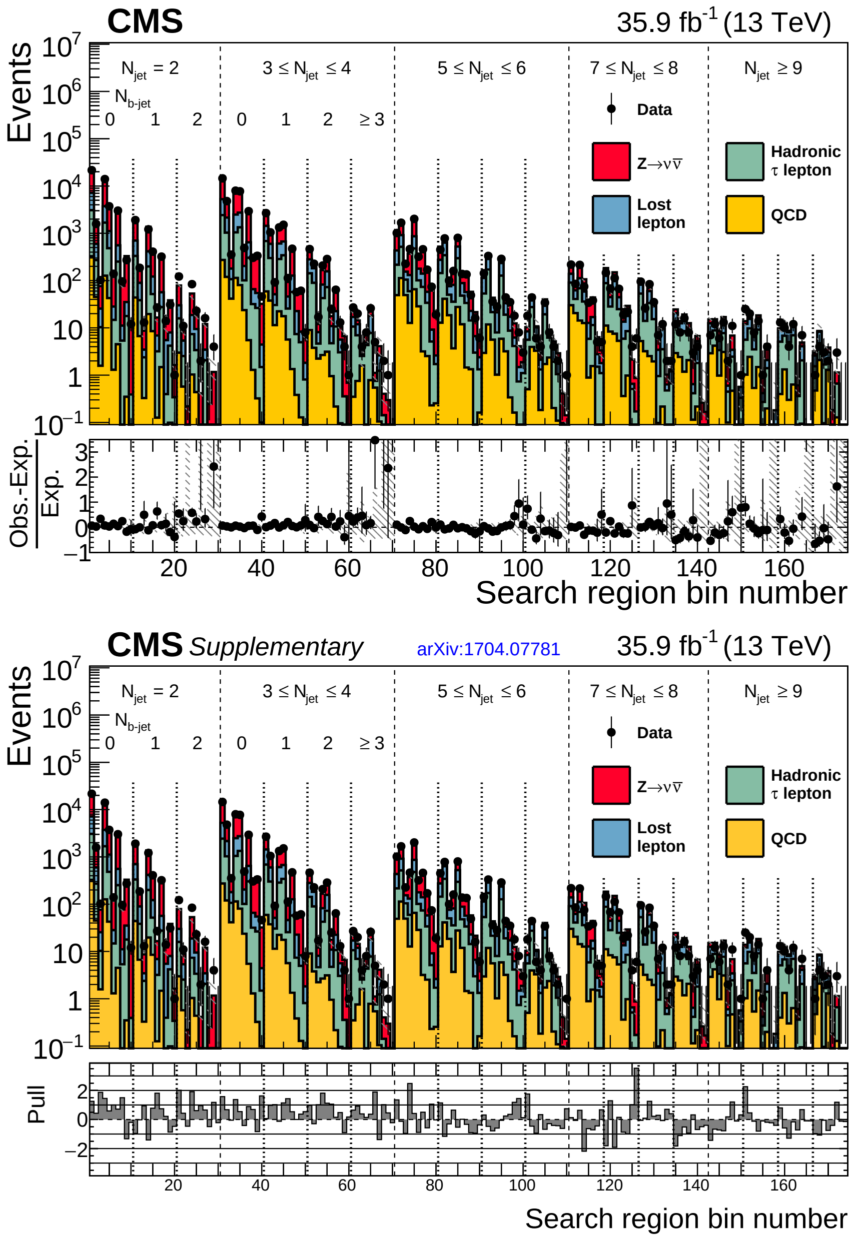

Figure 9.1: Observed number of events and pre-fit background predictions in all search bins. The lower panel of the top plot shows the relative difference between the observed data and estimated background, while the lower panel of the bottom plot shows the pull, defined as $(N_{\mathrm{Obs.}} - N_{\mathrm{Pred.}})/\sqrt{N_{\mathrm{Pred.}} + (\delta N_{\mathrm{Pred.}})^2}$, where $\delta N_{\mathrm{Pred.}}$ is the total (STAT+SYST) uncertainty on the background prediction, for each bin.

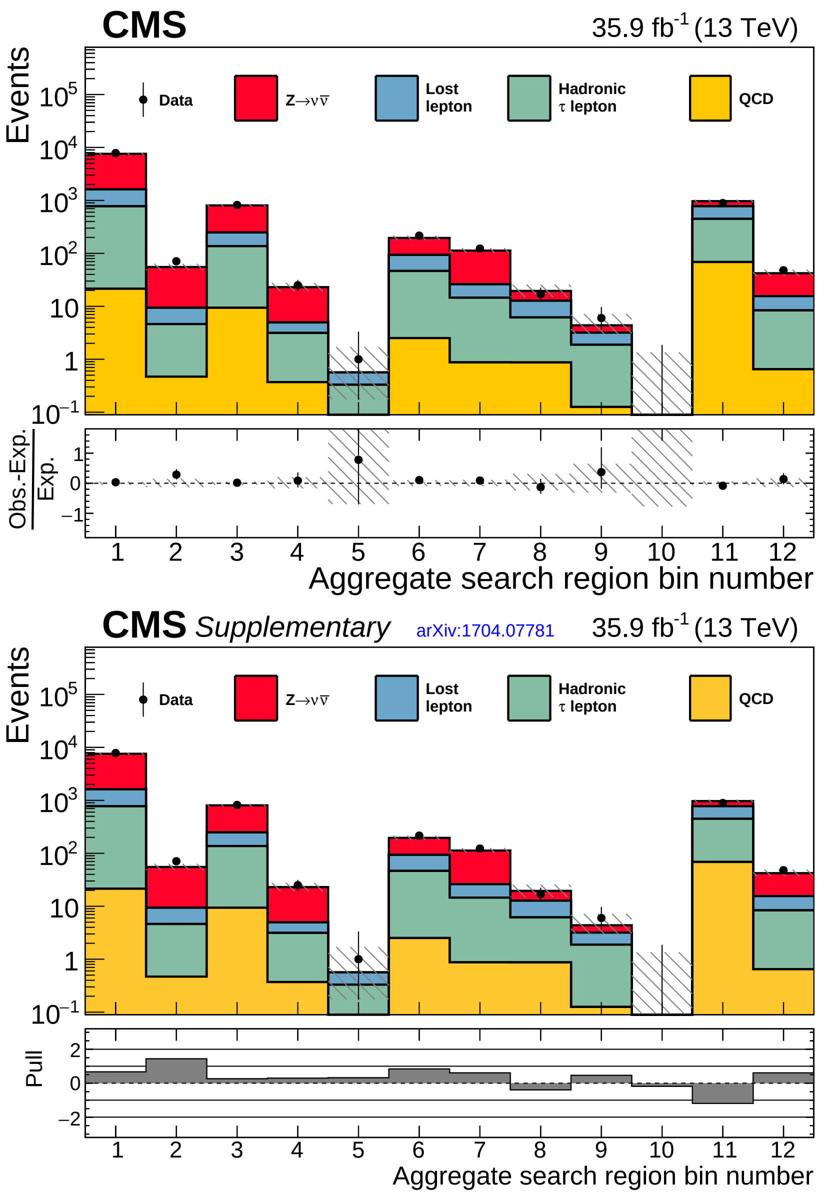

Figure 9.2: Observed number of events and pre-fit background predictions in the aggregate search regions. The lower panel of the top plot shows the relative difference between the observed data and estimated background, while the lower panel of the bottom plot shows the pull, defined as $(N_{\text{Obs.}} - N_{\text{Pred.}})/\sqrt{N_{\text{Pred.}} + (\delta N_{\text{Pred.}})^2}$, where $\delta N_{\text{Pred.}}$ is the total (STAT+SYST) uncertainty on the background prediction, for each bin. The selection, background predictions, and observed yields in each of these regions are summarized in Table 9.6.

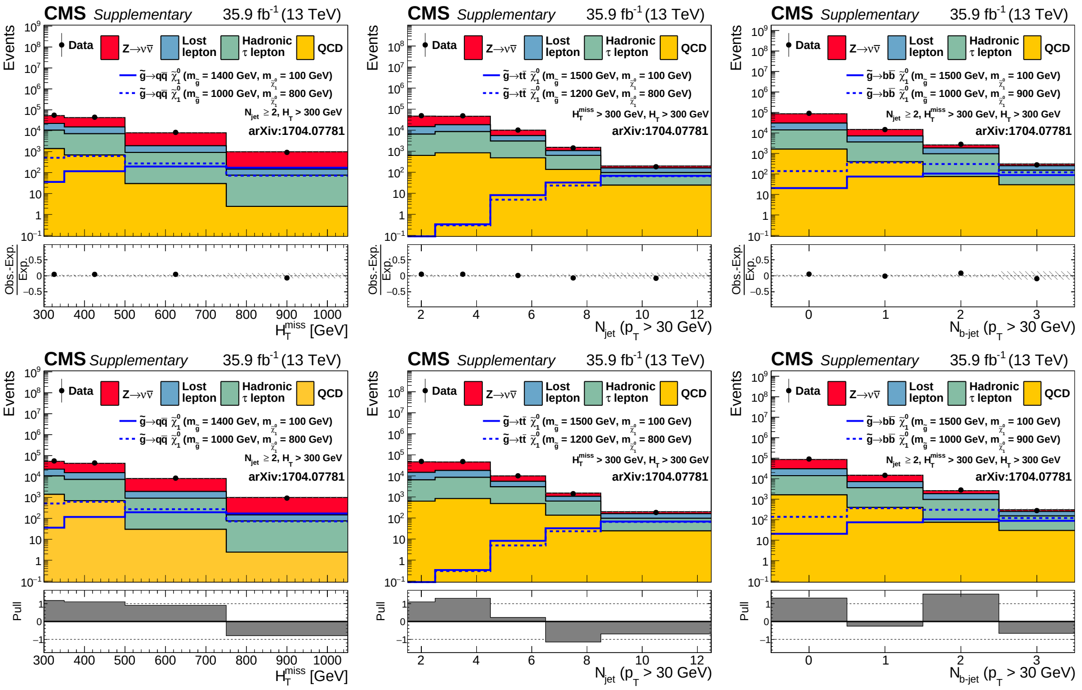

Figure 9.3: Top: from left-to-right, one-dimensional projections of observed number of events and pre-fit background predictions in the search region in H_T^{miss}, N_{jet}, and $N_{b\text{-jet}}$. The events in each distribution are integrated over the other three search variables. The bin contents are reported in Tables 9.7–9.9. Bottom: the same distributions, with the pull for each bin shown in the lower panel of each plot.

Figure 9.4 presents one-dimensional projections of the results in H_T^{miss}, N_{jet}, or $N_{b\text{-jet}}$ after criteria are imposed, as indicated in the legends. These criteria are chosen to select intervals of the search region parameter space particularly sensitive to the T1bbbb, T1tttt, T1qqqq, T2bb, T2tt, or T2qq scenario. In each case, example distributions are shown for two signal scenarios. These scenarios, one with $m_{\tilde{g}}$ or $m_{\tilde{q}} \gg m_{\tilde{\chi}_1^0}$ and one with $m_{\tilde{\chi}_1^0} \sim m_{\tilde{g}}$ or $m_{\tilde{q}}$, lie well within the parameter space excluded by the present analysis (see below).

Table 9.7: Observed number of events and pre-fit background predictions as a function of H_T^{miss}, integrating over all other search variables.

Bin	H_T^{miss} [GeV]	H_T [GeV]	N_{jet}	$N_{b\text{-jet}}$	Lost-e/μ	$\tau \to$ had	$Z \to \nu\bar{\nu}$	QCD	Total Pred.	Obs.
1	300-350	> 300	2+	all	$11776^{+100+560}_{-100-530}$	$9218^{+60+690}_{-60-700}$	$30601^{+110+1700}_{-110-1700}$	$1396^{+71+560}_{-71-460}$	$52992^{+210+2000}_{-210-2000}$	55370
2	350-500	> 350	2+	all	$7957^{+81+390}_{-81-370}$	$6509^{+51+490}_{-50-490}$	$27325^{+100+1500}_{-100-1500}$	$691^{+16+280}_{-16-230}$	$42482^{+170+1700}_{-170-1600}$	44343
3	500-750	> 500	2+	all	999^{+28+56}_{-27-53}	888^{+17+67}_{-17-68}	$6076^{+52+370}_{-51-360}$	30^{+1+12}_{-1-10}	$7994^{+69+380}_{-67-370}$	8354
4	> 750	> 750	2+	all	$70.9^{+8.9+5.0}_{-6.9-4.8}$	$72.5^{+5.5+6.8}_{-4.7-6.8}$	847^{+21+79}_{-19-74}	$2.43^{+0.18+0.96}_{-0.16-0.80}$	993^{+25+80}_{-23-74}	927

Table 9.8: Observed number of events and pre-fit background predictions as a function of N_{jet}, integrating over all other search variables.

Bin	N_{jet}	H_T^{miss} [GeV]	H_T [GeV]	$N_{b\text{-jet}}$	Lost-e/μ	$\tau \to$ had	$Z \to \nu\bar{\nu}$	QCD	Total Pred.	Obs.
1	2	> 300	> 300	all	$8215^{+96+400}_{-95-370}$	$5859^{+53+970}_{-53-970}$	$31948^{+110+1800}_{-110-1800}$	$634^{+17+320}_{-17-220}$	$46656^{+190+2100}_{-180-2100}$	48977
2	3-4	> 300	> 300	all	$9599^{+84+460}_{-83-440}$	$7703^{+54+420}_{-54-430}$	$27889^{+100+1500}_{-100-1500}$	$840^{+70+320}_{-70-280}$	$46030^{+190+1700}_{-190-1700}$	48269
3	5-6	> 300	> 300	all	$2494^{+34+140}_{-34-130}$	$2553^{+25+140}_{-25-140}$	$4506^{+45+290}_{-44-280}$	$486^{+10+180}_{-10-160}$	$10039^{+76+390}_{-75-380}$	10131
4	7-8	> 300	> 300	all	431^{+13+27}_{-13-26}	502^{+11+29}_{-10-30}	469^{+17+47}_{-16-46}	136^{+3+51}_{-3-45}	1537^{+30+80}_{-28-76}	1434
5	9+	> 300	> 300	all	$63.6^{+5.9+4.6}_{-5.2-4.4}$	$72.0^{+4.6+5.4}_{-3.8-5.4}$	$38.5^{+7.8+6.5}_{-5.3-7.6}$	24^{+1+11}_{-1-9}	198^{+13+14}_{-10-14}	183

Table 9.9: Observed number of events and pre-fit background predictions as a function of $N_{b\text{-jet}}$, integrating over all other search variables.

Bin	$N_{b\text{-jet}}$	H_T^{miss} [GeV]	H_T [GeV]	N_{jet}	Lost-e/μ	$\tau \to$ had	$Z \to \nu\bar{\nu}$	QCD	Total Pred.	Obs.
1	0	> 300	> 300	2+	$16264^{+120+750}_{-120-710}$	$12453^{+72+1100}_{-72-1100}$	$56415^{+140+3100}_{-140-3100}$	$1622^{+71+660}_{-71-530}$	$86753^{+250+3400}_{-240-3400}$	91255
2	1	> 300	> 300	2+	$3554^{+54+180}_{-53-170}$	$3223^{+33+200}_{-32-200}$	$7631^{+20+510}_{-20-510}$	$394^{+12+150}_{-12-130}$	$14802^{+90+590}_{-89-590}$	14646
3	2	> 300	> 300	2+	886^{+26+48}_{-25-46}	889^{+16+44}_{-16-45}	751^{+3+100}_{-3-100}	74^{+3+27}_{-3-25}	$2600^{+43+120}_{-41-120}$	2815
4	3+	> 300	> 300	2+	100^{+11+6}_{-9-6}	122^{+6+10}_{-6-10}	54^{+1+17}_{-1-17}	30^{+3+33}_{-3-27}	305^{+18+39}_{-15-34}	278

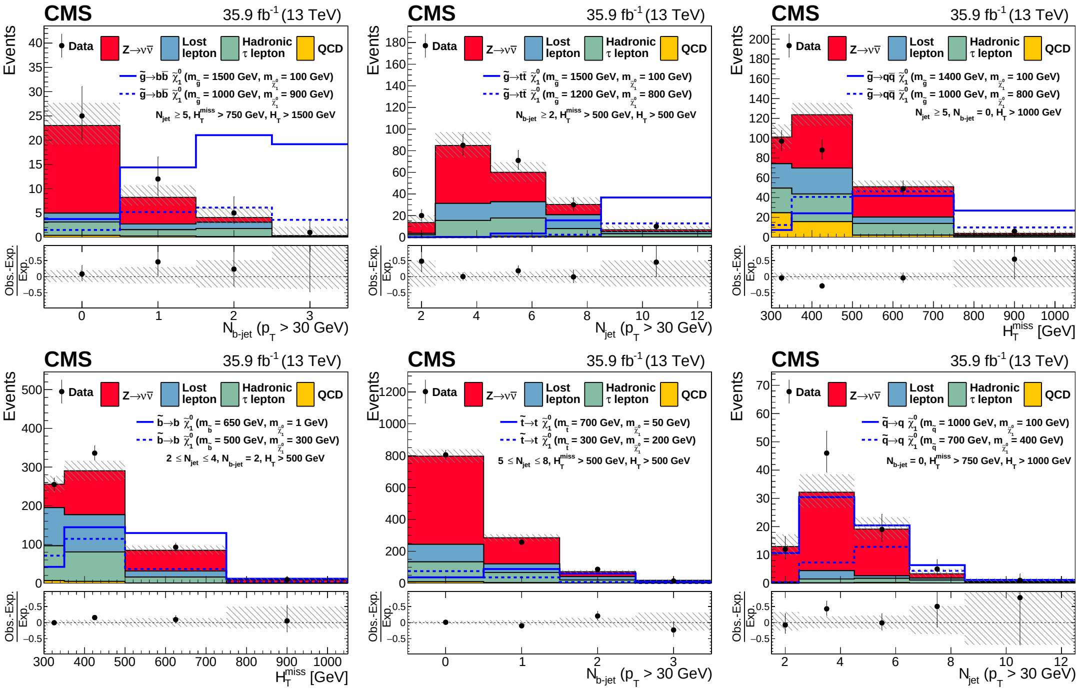

Figure 9.4: Observed numbers of events and corresponding SM background predictions for intervals of the search region parameter space particularly sensitive to the (upper left) T1bbbb, (upper center) T1tttt, (upper right) T1qqqq, (lower left) T2bb, (lower middle) T2tt, and (lower right) T2qq scenarios. The selection requirements are given in the figure legends. The hatched regions indicate the total uncertainties in the background predictions. The (unstacked) results for two example signal scenarios are shown in each instance, one with $m_{\tilde{g}}$ or $m_{\tilde{q}} \gg m_{\tilde{\chi}_1^0}$ and the other with $m_{\tilde{\chi}_1^0} \sim m_{\tilde{g}}$ or $m_{\tilde{q}}$.

9.2 Statistical interpretation

In the absence of significant evidence for new physics, we proceed to set limits on the production cross sections for each of the models considered using a procedure established by the LHC Higgs Combination Group in 2011. A modified frequentist approach, called CL_s, is employed to evaluate and compare the background-only (SM-only) and signal+background hypotheses [114]. This approach and limit-setting procedure is summarized here in the context of this search. For simplicity, the procedure will first be summarized excluding treatment of systematic uncertainties.

To combine information from all signal regions, and thus provide the most complete test of each hypothesis, a likelihood function is constructed as the product of Poisson probabilities for all signal regions as follows:

$$\begin{aligned}\mathcal{L} &= \mathrm{Poisson}(n|\lambda) \\ &= \prod_{i=1}^{N_{\mathrm{SR}}} \frac{\lambda_i^{n_i}}{n_i!} e^{-\lambda_i}\end{aligned}$$

Here i is an index for the search region that ranges from 1 to 174 in the 2015 analysis. The Poisson mean term λ_i is the best estimate of the number of events in each search region and n_i is the number of events observed in data in each region. We further define λ_i as the sum of the signal and background contribution in each region:

$$\lambda_i = \mu s_i + \sum_{j=1}^{4} b_{ij} \tag{9.54}$$

where the index j runs over the four individually-measured SM backgrounds, b_{ij} is the data-driven background estimate for background j in search region i and s_i is the expected signal yield in search region i. The expected signal yield is modified by the parameter μ, sometimes called the "signal strength" or "signal strength modifier," which is allowed to vary in order to test values for the signal production cross section. Under the background-only hypothesis, $\mu = 0$. If the signal exists and is produced at the reference theoretical cross section, then $\mu = 1$.

To incorporate the effects of systematic uncertainties on the expected signal and background yields, we introduce the nuisance parameters θ for N_{sys} different sources of uncertainty on the signal and background. These sources of uncertainty are either treated as fully-correlated across all search regions (e.g., for the luminosity uncertainty on the signal yields), fully-uncorrelated across all search regions (e.g., the statistical precision of the MC closure tests of the background estimation methods in each search region), or, in the case of partially-correlated uncertainties, separated into components that can be treated as either fully-correlated or fully-uncorrelated all across search regions (e.g., the lepton acceptance, which is correlated across the $N_{b\text{-jet}}$ dimension at high-N_{jet}). The treatment of these correlations is summarized in Sections 8.1–8.4 for uncertainties on the background estimation and in Section 6.2.2 for uncertainties on the signal efficiency.

With these nuisance parameters, the likelihood function can be written as:

$$\mathcal{L}(n|\mu, \theta) = \text{Poisson}(n|\mu s(\theta) + b(\theta)) \times p(\tilde{\theta}|\theta) \tag{9.55}$$

where $p(\tilde{\theta}|\theta)$ represents a product of the probability density functions (pdfs) for each uncertainty. These pdfs can be understood as a frequentist's re-imagining of a systematic error pdf as a Bayesian posterior for some auxiliary measurement $\tilde{\theta}$. Note that two different sets of uncertainties, and thus two different products of pdfs, apply to the signal and background terms. For most sources of uncertainty, the nuisance pdfs are represented by log-normal distributions,

$$p(\tilde{\theta}|\theta) = \frac{1}{\sqrt{2\pi}\ln\kappa} \exp\left(-\frac{(\ln(\theta/\tilde{\theta})^2}{2(\ln\kappa)^2}\right)\frac{1}{\theta} \tag{9.56}$$

where $\tilde{\theta}$ represents the best measurement of the nuisance parameter (e.g., mean, peak-value) and κ is the width of the log-normal distribution.

To evaluate the compatibility of the data with the background-only and signal+background hypotheses, we construct the test statistic

$$q_\mu = -2\ln\left[\frac{\mathcal{L}(n|\mu, \hat{\theta}_\mu)}{\mathcal{L}(n|\hat{\mu}, \hat{\theta})}\right], \qquad 0 \leq \hat{\mu} \leq \mu \tag{9.57}$$

In the numerator, the signal strength is fixed and the likelihood is maximized for the nuisance parameters. The values of the nuisance parameters yielding the maximum likelihood are represented by $\hat{\theta}_\mu$. In the denominator, the likelihood is maximized allowing both the signal strength and nuisance parameters to vary. The values of the signal strength and nuisance parameters yielding the maximum likelihood are represented by $\hat{\mu}$ and $\hat{\theta}$, respectively. Note that $\hat{\mu}$ is constrained to be non-negative, since signal cannot be negative. It is also constrained to a one-sided confidence integral ($\hat{\mu} \leq \mu$), so that upward fluctuations in the data ($n > \mu s + b$) cannot be interpreted as evidence against the signal+background hypothesis. When n represents the observed numbers of events in data, $q_\mu = q_\mu^{\text{data}}$.

Limits are set by calculating the probability to observe an outcome as "signal-like" as the one observed for the background only and signal+background hypotheses:

$$\mathrm{CL}_b = P(q_\mu \geq q_\mu^{\text{data}} | b)$$

$$\mathrm{CL}_{s+b} = P(q_\mu \geq q_\mu^{\text{data}} | \mu s + b)$$

The ratio of these two probabilities,

$$\mathrm{CL}_s = \frac{\mathrm{CL}_{s+b}}{\mathrm{CL}_b} \qquad (9.58)$$

determines whether or not a signal can be excluded at a given confidence level. For the commonly-used 95% confidence level exclusion,

$$\mathrm{CL}_s \leq 0.05 \tag{9.59}$$

While the most accurate estimates of the probabilities CL_b and CL_{s+b} are obtained by running a series of pseudo-experiments to generate a pdf of q_μ, this procedure is restrictively time-consuming to run on hundreds of signal models, so asymptotic results for q_μ are computed using approximations detailed in Refs. [114, 115].

9.3 Limits on SMS models

We proceed to set upper limits on the production cross section (times branching ratio) for each of the SMS SUSY scenarios. A fraction of events in the T1tttt, T5qqqqVV, and T2tt scenarios may have final states with one or more leptons emerging from the decay of a W or Z boson. These events can contaminate the single-lepton control regions, which may induce a over-measurement of the lost lepton and hadronic tau background contributions in the search region. To take into account this potential bias and resulting loss of signal sensitivity, the number of events in each CR is corrected to include the predicted number of signal events in the context of the model being examined. The total effective number of background events predicted in each search region is determined from these corrected control region yields, and this quantity is used to calculate the limits.

Figure 9.5 shows the observed and expected 95% CL upper limits on cross section times branching ratio for the T1tttt, T1bbbb, T1qqqq, and T5qqqqVV SUSY scenarios. Gluinos with masses below around 1940, 1970, 1820, and 1800 GeV are excluded for the T1tttt, T1bbbb, T1qqqq, and T5qqqqVV scenarios, respectively. These results extend those we obtained in Run I by over 500 GeV.

Figure 9.7 shows the observed and expected 95% CL upper limits on cross section times branching ratio for the T2tt, T2bb, and T2qq SUSY scenarios, respectively. For a massless LSP, we exclude squarks with masses below around 970, 1040, and 1450 GeV for the T2tt, T2bb, and T2qq scenarios, respectively.

For a massless LSP, we exclude squarks with masses below around 830, 780, and 1150 GeV for the T2tt, T2bb, and T2qq scenarios, respectively, while gluinos with masses below around 1620, 1750, 1680, and 1620 GeV are excluded, again respectively, for the T1tttt, T1bbbb, T1qqqq, and T5qqqqVV scenarios. These results extend those we obtained in Run I by over 300 GeV.

We also consider a T2qq scenario in which there is no mass degeneracy between four squark flavors and and two chirality states. In this scenario, where only one of these eight states ("one light $\tilde{q}$," in Figure 9.7) are accessible at the LHC, the upper limit on the squark mass is reduced to around 1050 GeV.

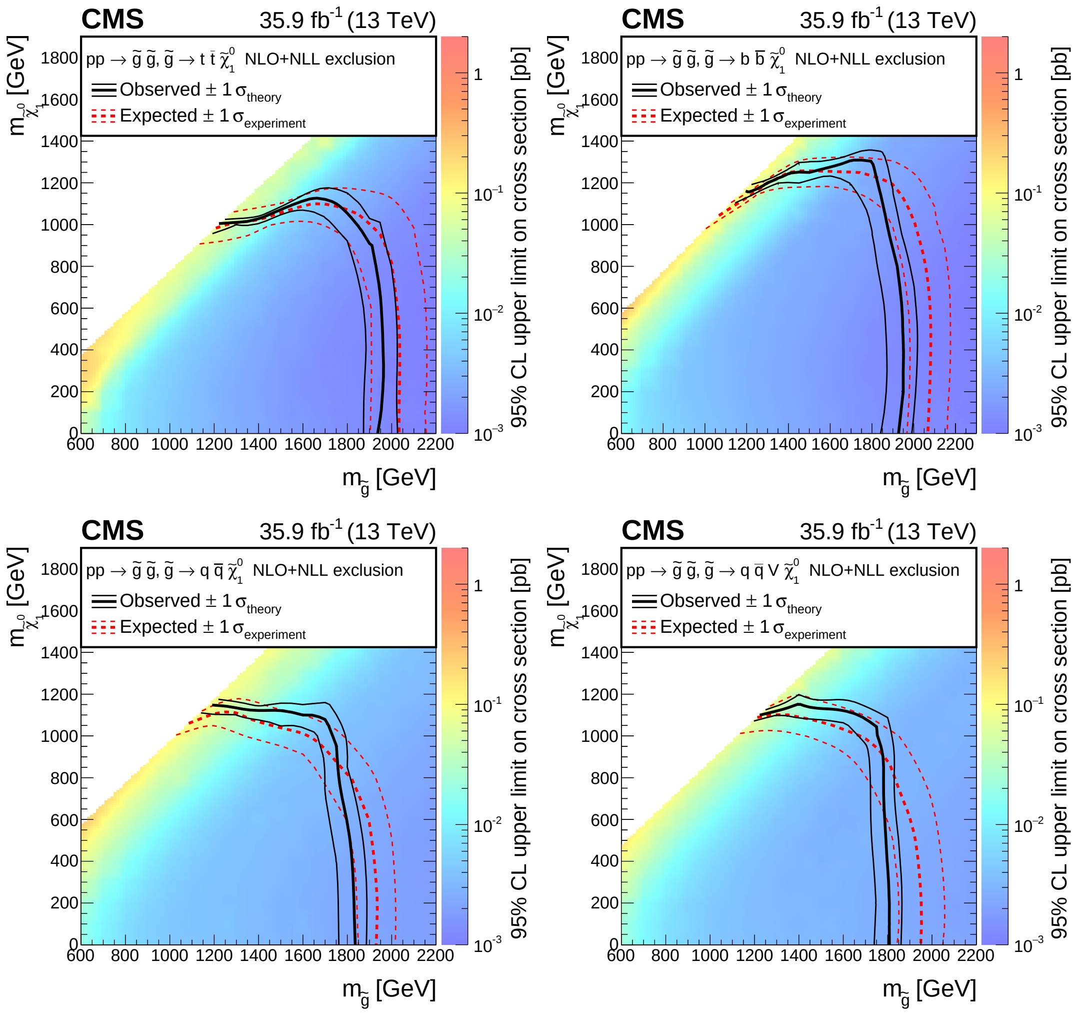

Figure 9.5: Clockwise from the top-left: observed and expected upper limit exclusion at 95% CL for the T1tttt, T1bbbb, T5qqqqVV, and T1qqqq simplified models. The black curves show the observed exclusion contours assuming the NLO+NLL cross sections times branching ratio [92, 93, 94, 95, 96], with their corresponding ±1 standard deviation uncertainties [116]. The red curves show the expected limits with ±1 standard deviation experimental uncertainties. The dashed gray lines indicate the $m_{\tilde{g}} = m_{\tilde{\chi}_1^0}$ diagonal.

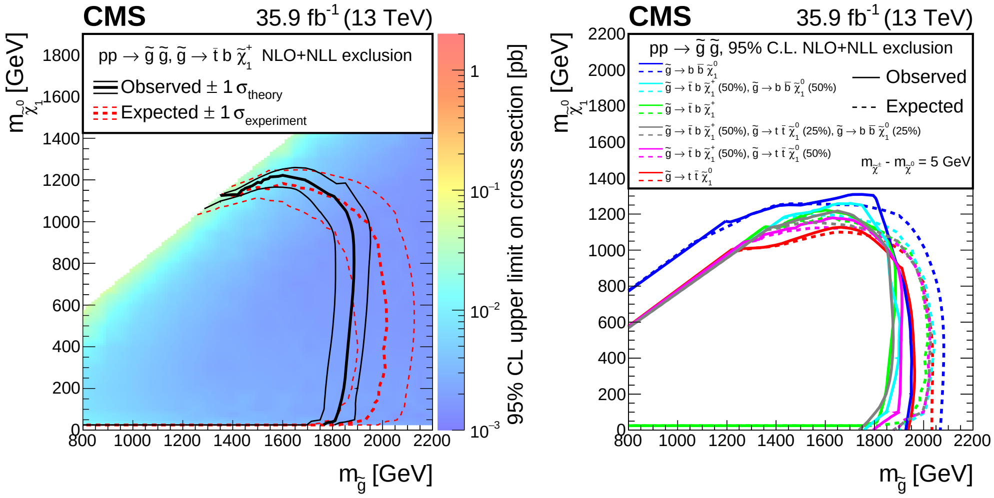

Figure 9.6: Left: observed and expected upper limit exclusion at 95% CL for the T1tbtb simplified model. Right: the corresponding 95% NLO+NLL exclusion curves for the mixed models of gluino decays to heavy squarks.

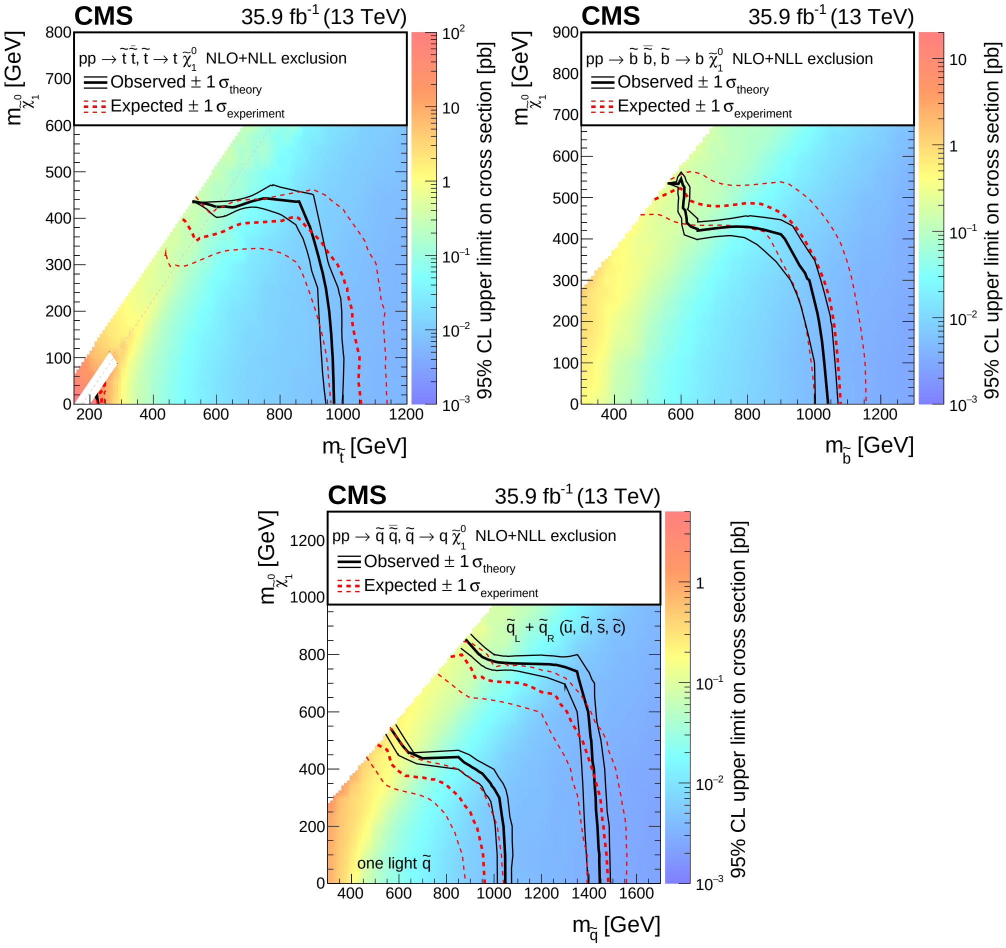

Figure 9.7: Clockwise from the top-left: observed and expected upper limit exclusion at 95% CL for the T2tt, T2bb, and T2qq simplified models. The black curves show the observed exclusion contours assuming the NLO+NLL cross sections times branching ratio [92, 93, 94, 95, 96], with their corresponding ±1 standard deviation uncertainties [116]. The red curves show the expected limits with ±1 standard deviation experimental uncertainties. The dashed gray lines indicate the $m_{\tilde{q}} = m_{\tilde{\chi}_1^0}$ diagonal.

Chapter 10

Conclusions

The limits set in this analysis are among the most stringent set by both CMS (Figure 10.1) and ATLAS [117] to date. The limits on gluino and third generation squark masses are approaching, if not exceeding, the naturalness benchmarks mentioned in Section 2.2.1 for SMS models with light LSPs. But is this sufficient evidence to rule out natural SUSY? Many would argue otherwise. Recall the key underlying assumptions of the simplified models:

- the gluinos and squarks have only one decay mode,
- beyond the two particles that characterize a simplified model, there are usually no other SUSY particles with masses in the TeV range, so the decay kinematics are relatively simple.

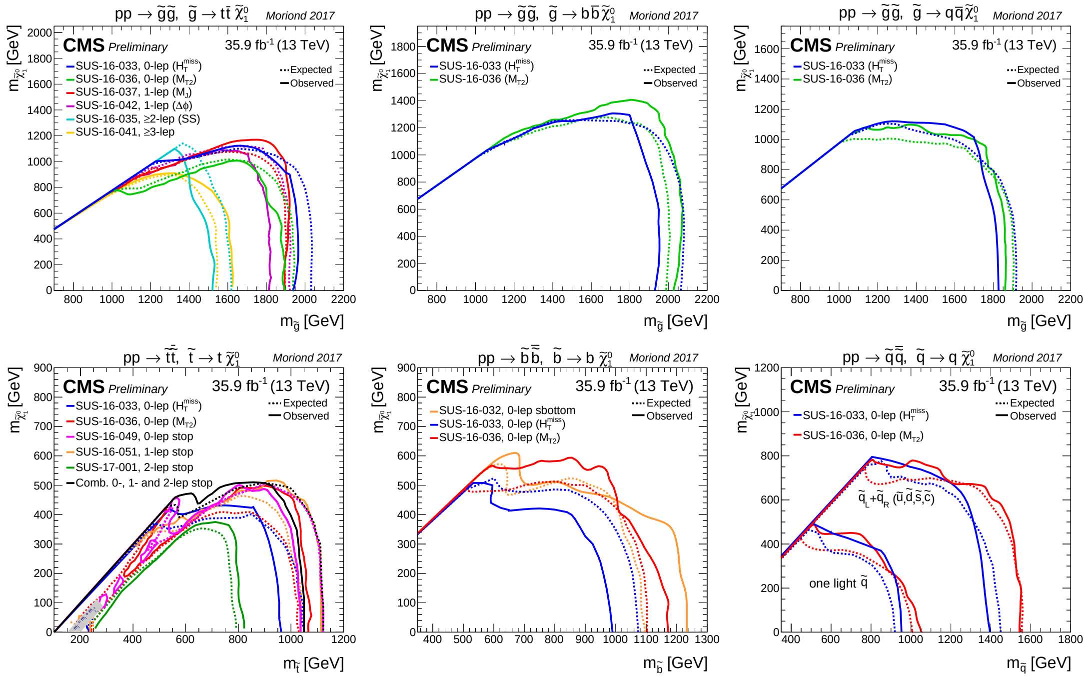

Figure 10.1: Clockwise from the top-left: observed and expected upper limit exclusion at 95% CL for the T1tttt, T1bbbb, T1qqqq, T2qq, T2bb, and T2tt simplified models, as set by various CMS analyses [118, 119, 120, 121, 122, 123, 124, 125, 126]. The solid curves show the observed exclusion contours assuming the NLO+NLL cross sections times branching ratio, with their corresponding ±1 standard deviation uncertainties. The dashed curves show the expected limits with ±1 standard deviation experimental uncertainties. The limits set by this analysis (SUS-16-033) are marked by the dark blue curves.

If the first assumption is violated, then the cross section times branching fractions for the SUSY processes will be lower than assumed. If the second assumption is violated, than the kinematic distributions of the signal models could be drastically changed. Several exampl es of this effect were found when the results of similar Run I analyses were reinterpreted in the in the framework of the phenomenological minimal supersymmetric standard model (pMSSM), a class of models with 19 free parameters and generally more complex decay chains [127, 128].

Others have suggested that SUSY can be natural even with stops and gluinos in the 3-4 TeV range, as long as the higgsinos are light. A scenario in which the only SUSY particles accessible at the LHC are $\mathcal{O}(100)$ GeV higgsinos would be very difficult to probe with a multijet + H_T^{miss} search, since the higgsinos would probably not have high-p_T decay products [129]. Such a scenario may require a more targeted approach.

Nevertheless, it is difficult to poke too many large holes in these results; so far, SUSY is not where we hoped it would be. Perhaps the most encouraging thought going forward is that the LHC is expected to deliver nearly 100 times the current data over the next two decades. We may not know exactly where to look next, but with that much data, new physics might be found in places too exotic to dream of exploring today.

Bibliography

[1] CMS Collaboration, "Observation of a new boson at a mass of 125 GeV with the CMS experiment at the LHC," *Phys. Lett.*, vol. B716, pp. 30–61, 2012.

[2] ATLAS Collaboration, "Observation of a new particle in the search for the Standard Model Higgs boson with the ATLAS detector at the LHC," *Phys. Lett.*, vol. B716, pp. 1–29, 2012.

[3] ATLAS Collaboration, "Measurement of Higgs boson production in the diphoton decay channel in pp collisions at center-of-mass energies of 7 and 8 TeV with the ATLAS detector," *Phys. Rev.*, vol. D90, no. 11, p. 112015, 2014.

[4] CMS Collaboration, "Measurement of the properties of a Higgs boson in the four-lepton final state," *Phys. Rev.*, vol. D89, no. 9, p. 092007, 2014.

[5] CMS Collaboration, "Search for supersymmetry in multijet events with missing transverse momentum in proton-proton collisions at 13 TeV," April 2017. Submitted to Phys. Rev. D.

[6] B. Odom, D. Hanneke, B. d'Urso, and G. Gabrielse, "New measurement of the electron magnetic moment using a one-electron quantum cyclotron," *Physical Review Letters*, vol. 97, no. 3, p. 030801, 2006.

[7] F. Halzen and A. D. Martin, *Quarks & Leptons: An Introductory Course In Modern Particle Physics.* John Wiley & Sons, 2008.

[8] M. Peskin and D. Schroeder, *An Introduction To Quantum Field Theory (Frontiers in Physics).* Westview Press, 1995.

[9] I. J. Aichison and A. J. Hey, *Gauge theories in particle physics: A practical introduction, Volume 2: Non-Abelian Gauge theories: QCD and the electroweak theory*, vol. 2. CRC Press, 2012.

[10] M. Srednicki, *Quantum Field Theory.* Cambridge University Press, 2007.

[11] Wikimedia Commons, "Standard Model of Elementary Particles," 2007.

[12] Planck Collaboration, "Planck 2013 results. I. Overview of products and scientific results," *Astronomy & Astrophysics*, vol. 571, p. A1, 2014.

[13] G. Bertone, D. Hooper, and J. Silk, "Particle dark matter: Evidence, candidates and constraints," *Phys. Rept.*, vol. 405, pp. 279–390, 2005.

[14] Y. Fukuda *et al.*, "Measurements of the solar neutrino flux from Super-Kamiokande's first 300 days," *Phys. Rev. Lett.*, vol. 81, pp. 1158–1162, 1998. [Erratum: Phys. Rev. Lett.81,4279(1998)].

[15] V. A. Rubakov and M. E. Shaposhnikov, "Electroweak baryon number non-conservation in the early universe and in high-energy collisions," *Usp. Fiz. Nauk*, vol. 166, pp. 493–537, 1996. [Phys. Usp.39,461(1996)].

[16] A. D. Sakharov, "Violation of CP invariance, C asymmetry, and baryon asymmetry of the universe," *Soviet Physics Uspekhi*, vol. 34, no. 5, p. 392, 1991.

[17] L. Susskind, "The gauge hierarchy problem, technicolor, supersymmetry, and all that," *Physics Reports*, vol. 104, no. 2-4, pp. 181–193, 1984.

[18] S. P. Martin, "A supersymmetry primer," *Adv. Ser. Direct. High Energy Phys*, vol. 21, no. 515, pp. 1–153, 2010.

[19] ATLAS and CMS Collaborations, "Combined Measurement of the Higgs Boson Mass in pp Collisions at $\sqrt{s} = 7$ and 8 TeV with the ATLAS and CMS Experiments," *Phys. Rev. Lett.*, vol. 114, p. 191803, 2015.

[20] L. J. Garay, "Quantum gravity and minimum length," *International Journal of Modern Physics A*, vol. 10, no. 02, pp. 145–165, 1995.

[21] C. Brust, A. Katz, S. Lawrence, and R. Sundrum, "SUSY, the Third Generation and the LHC," *JHEP*, vol. 03, p. 103, 2012.

[22] M. Papucci, J. T. Ruderman, and A. Weiler, "Natural SUSY endures," *Journal of High Energy Physics*, vol. 2012, no. 9, pp. 1–45, 2012.

[23] A. Djouadi, "The anatomy of electro-weak symmetry breaking. i: The higgs boson in the standard model, phys. rept. 457 (2008) 1–216," *arXiv preprint hep-ph/0503172*, vol. 15, p. 25.

[24] A. Djouadi, "The anatomy of electro-weak symmetry breaking. ii. the higgs bosons in the minimal supersymmetric model, phys. rept. 459 (2008) 1–241," *arXiv preprint hep-ph/0503173*, p. 8.

[25] "Beyond the Standard Model: the search for "new physics"," September 2015. Retrieved May 26, 2017 from http://davidc.web.cern.ch.

[26] J. L. Feng, "Naturalness and the status of supersymmetry," *Annual Review of Nuclear and Particle Science*, vol. 63, pp. 351–382, 2013.

[27] N. Craig, "The State of Supersymmetry after Run I of the LHC," in *Beyond the Standard Model after the first run of the LHC Arcetri, Florence, Italy, May 20-July 12, 2013*, 2013.

[28] Y. Gershtein *et al.*, "Working Group Report: New Particles, Forces, and Dimensions," in *Proceedings, Community Summer Study 2013: Snowmass on the Mississippi (CSS2013): Minneapolis, MN, USA, July 29-August 6, 2013*, 2013.

[29] G. R. Farrar and P. Fayet, "Phenomenology of the Production, Decay, and Detection of New Hadronic States Associated with Supersymmetry," *Phys. Lett.*, vol. 76B, pp. 575–579, 1978.

[30] G. Jungman, M. Kamionkowski, and K. Griest, "Supersymmetric dark matter," *Physics Reports*, vol. 267, no. 5, pp. 195 – 373, 1996.

[31] V. Khachatryan *et al.*, "Searches for third-generation squark production in fully hadronic final states in proton-proton collisions at $\sqrt{s} = 8$ TeV," *JHEP*, vol. 06, p. 116, 2015.

[32] "Exclusion limits on gluino and top-squark pair production in natural SUSY scenarios with inclusive razor and exclusive single-lepton searches at 8 TeV," Tech. Rep. CMS-PAS-SUS-14-011, CERN, Geneva, 2014.

[33] "Search for direct production of bottom squark pairs," Tech. Rep. CMS-PAS-SUS-13-018, CERN, Geneva, 2014.

[34] C. Lefèvre, "The CERN accelerator complex. Complexe des accélérateurs du CERN." Dec 2008.

[35] O. S. Brüning, P. Collier, P. Lebrun, S. Myers, R. Ostojic, J. Poole, and P. Proudlock, "LHC Design Report Vol. 1: The LHC Main Ring," 2004.

[36] O. S. Brüning, P. Collier, P. Lebrun, S. Myers, R. Ostojic, J. Poole, and P. Proudlock, "LHC Design Report Vol. 2: The LHC infrastructure and general services," 2004.

[37] M. Benedikt, P. Collier, V. Mertens, J. Poole, and K. Schindl, "LHC Design Report Vol. 3: The LHC injector chain," 2004.

[38] C. Quigg, "LHC Physics Potential versus Energy," 2009.

[39] J. Stirling, "Parton luminosity and cross section plots," *Private communication. http://www. hep. ph. ic. ac. uk/˜ wstirlin/plots/plots. html*, 2016.

[40] A. D. Martin, W. J. Stirling, R. S. Thorne, and G. Watt, "Parton distributions for the LHC," *Eur. Phys. J.*, vol. C63, pp. 189–285, 2009.

[41] L. Taylor, "CMS detector design," November 2011. Retrieved May 30, 2017 from http://cms.web.cern.ch/news/cms-detector-design.

[42] D. Barney, “CMS Detector Slice.” Retrieved May 30, 2017 from https://cds.cern.ch/record/2120661, Jan 2016.

[43] T. Lenzi, “Development and Study of Different Muon Track Reconstruction Algorithms for the Level-1 Trigger for the CMS Muon Upgrade with GEM Detectors,” Master’s thesis, U. Brussels (main), 2013.

[44] CMS Collaboration, “Description and performance of track and primary-vertex reconstruction with the CMS tracker,” *JINST*, vol. 9, no. 10, p. P10009, 2014.

[45] CMS Collaboration, “Energy calibration and resolution of the CMS electromagnetic calorimeter in pp collisions at $\sqrt{s} = 7$ TeV,” 06 2013.

[46] Adzic, Petar, “Energy resolution of the barrel of the CMS electromagnetic calorimeter,” *Journal of Instrumentation*, vol. 2, no. 04, p. P04004, 2007.

[47] F. De Guio and CMS Collaboration, “Performance of the CMS electromagnetic calorimeter and its role in the hunt for the Higgs boson in the two-photon channel,” in *Journal of Physics: Conference Series*, vol. 455, p. 012028, IOP Publishing, 2013.

[48] CMS Collaboration, “CMS Physics Technical Design Report: Volume I (PTDR1), Detector Performace and Software,” 2006.

[49] CMS Collaboration, "CMS Physics Technical Design Report, Volume II (PTDR2): Physics Performance," *Journal of Physics G: Nuclear and Particle Physics*, vol. 34, no. 6, pp. 995–1579, 2007.

[50] USCMS and ECAL/HCAL Collaborations (S. Abdullin et al.), "The CMS barrel calorimeter response to particle beams from 2 to 350 GeV/c," *The European Physical Journal C*, vol. 61, no. 2, pp. 353–356, 2009.

[51] CMS Collaboration, "Performance of the CMS hadron calorimeter with cosmic ray muons and LHC beam data," *Journal of Instrumentation*, vol. 5, no. 03, p. T03012, 2010.

[52] G. Abbiendi and CMS Collaboration, "The CMS muon system in Run2: preparation, status and first results," *PoS*, vol. EPS-HEP2015, p. 237, 2015.

[53] CMS Collaboration, "The performance of the CMS muon detector in proton-proton collisions at $\sqrt{s} = 7$ TeV at the LHC," *JINST*, vol. 8, p. P11002, 2013.

[54] CMS Collaboration, "Performance of the CMS muon detector and reconstruction in LHC Run-2," Tech. Rep. CMS-PAS-MUO-16-001, CERN, Geneva, 2017.

[55] CMS Collaboration, "The CMS trigger system," 09 2016.

[56] R. Frühwirth, “Application of kalman filtering to track and vertex fitting,” *Nuclear Instruments and Methods in Physics Research Section A: Accelerators, Spectrometers, Detectors and Associated Equipment*, vol. 262, no. 2, pp. 444 – 450, 1987.

[57] K. Rose, “Deterministic annealing for clustering, compression, classification, regression, and related optimization problems,” *Proceedings of the IEEE*, vol. 86, no. 11, pp. 2210–2239, 1998.

[58] CMS Collaboration, “Performance of Electron Reconstruction and Selection with the CMS Detector in Proton-Proton Collisions at s = 8 TeV,” *JINST*, vol. 10, no. 06, p. P06005, 2015.

[59] CMS Collaboration, “Performance of Photon Reconstruction and Identification with the CMS Detector in Proton-Proton Collisions at $\sqrt{s} = 8$ TeV,” *JINST*, vol. 10, no. 08, p. P08010, 2015.

[60] CMS Collaboration, “Particle-Flow Event Reconstruction in CMS and Performance for Jets, Taus, and MET,” Tech. Rep. CMS-PAS-PFT-09-001, CERN, 2009. Geneva, Apr 2009.

[61] CMS Collaboration, “Commissioning of the Particle-flow Event Reconstruction with the first LHC collisions recorded in the CMS detector,” Tech. Rep. CMS-PAS-PFT-10-001, 2010.

[62] M. Cacciari, G. P. Salam, and G. Soyez, “The anti-k_t jet clustering algorithm,” *JHEP*, vol. 04, p. 063, 2008.

[63] M. Cacciari, G. P. Salam, and G. Soyez, “Fastjet user manual,” *The European Physical Journal C*, vol. 72, no. 3, pp. 1–54, 2012.

[64] M. U. Mozer, “Electroweak Physics at the LHC,” *Springer Tracts Mod. Phys.*, vol. 267, pp. 1–115, 2016.

[65] CMS Collaboration, “Identification of b quark jets at the CMS Experiment in the LHC Run 2,” 2016.

[66] CMS Collaboration, “Performance of b tagging at $\sqrt{s} = 8$ TeV in multijet, ttbar and boosted topology events,” Tech. Rep. CMS-PAS-BTV-13-001, CERN, Geneva, 2013.

[67] CMS Collaboration, “Performance of b-Tagging Algorithms in Proton Collisions at 13 TeV using the 2016 Data,” Tech. Rep. CMS-DP-2016-042, Jul 2016.

[68] CMS Collaboration, “Public CMS Luminosity Information,” August 2016. Retrieved September 5, 2016 from https://twiki.cern.ch/twiki/bin/view/CMSPublic/LumiPublicResults.

[69] J. Alwall, R. Frederix, S. Frixione, V. Hirschi, F. Maltoni, O. Mattelaer, H. S. Shao, T. Stelzer, P. Torrielli, and M. Zaro, "The automated computation of tree-level and next-to-leading order differential cross sections, and their matching to parton shower simulations," *JHEP*, vol. 07, p. 079, 2014.

[70] P. Nason, "A new method for combining NLO QCD with shower Monte Carlo algorithms," *JHEP*, vol. 11, p. 040, 2004.

[71] S. Frixione, P. Nason, and C. Oleari, "Matching NLO QCD computations with Parton Shower simulations: the POWHEG method," *JHEP*, vol. 11, p. 070, 2007.

[72] S. Alioli, P. Nason, C. Oleari, and E. Re, "A general framework for implementing NLO calculations in shower Monte Carlo programs: the POWHEG BOX," *JHEP*, vol. 06, p. 043, 2010.

[73] S. Alioli, P. Nason, C. Oleari, and E. Re, "NLO single-top production matched with shower in POWHEG: s- and t-channel contributions," *JHEP*, vol. 09, p. 111, 2009.

[74] E. Re, "Single-top Wt-channel production matched with parton showers using the POWHEG method," *Eur. Phys. J. C*, vol. 71, p. 1547, 2011.

[75] R. D. Ball *et al.*, “Parton distributions for the LHC Run II,” *JHEP*, vol. 04, p. 040, 2015.

[76] T. Melia, P. Nason, R. Rontsch, and G. Zanderighi, “W^+W^-, WZ and ZZ production in the POWHEG BOX,” *JHEP*, vol. 11, p. 078, 2011.

[77] M. Beneke, P. Falgari, S. Klein, and C. Schwinn, “Hadronic top-quark pair production with NNLL threshold resummation,” *Nucl. Phys. B*, vol. 855, p. 695, 2012.

[78] M. Cacciari, M. Czakon, M. Mangano, A. Mitov, and P. Nason, “Top-pair production at hadron colliders with next-to-next-to-leading logarithmic soft-gluon resummation,” *Phys. Lett. B*, vol. 710, p. 612, 2012.

[79] P. Bärnreuther, M. Czakon, and A. Mitov, “Percent Level Precision Physics at the Tevatron: First Genuine NNLO QCD Corrections to $q\bar{q} \to t\bar{t} + X$,” *Phys. Rev. Lett.*, vol. 109, p. 132001, 2012.

[80] M. Czakon and A. Mitov, “NNLO corrections to top-pair production at hadron colliders: the all-fermionic scattering channels,” *JHEP*, vol. 12, p. 054, 2012.

[81] M. Czakon and A. Mitov, “NNLO corrections to top pair production at hadron colliders: the quark-gluon reaction,” *JHEP*, vol. 01, p. 080, 2013.

[82] M. Czakon, P. Fiedler, and A. Mitov, “Total Top-Quark Pair-Production Cross Section at Hadron Colliders Through $O(\alpha_S^4)$,” *Phys. Rev. Lett.*, vol. 110, p. 252004, 2013.

[83] R. Gavin, Y. Li, F. Petriello, and S. Quackenbush, “W Physics at the LHC with FEWZ 2.1,” *Comput. Phys. Commun.*, vol. 184, p. 208, 2013.

[84] R. Gavin, Y. Li, F. Petriello, and S. Quackenbush, “FEWZ 2.0: A code for hadronic Z production at next-to-next-to-leading order,” *Comput. Phys. Commun.*, vol. 182, p. 2388, 2011.

[85] T. Sjöstrand, S. Ask, J. R. Christiansen, R. Corke, N. Desai, P. Ilten, S. Mrenna, S. Prestel, C. O. Rasmussen, and P. Z. Skands, “An Introduction to PYTHIA 8.2,” *Comput. Phys. Commun.*, vol. 191, p. 159, 2015.

[86] S. Agostinelli *et al.*, “GEANT4—a simulation toolkit,” *Nucl. Instrum. Meth. A*, vol. 506, p. 250, 2003.

[87] N. Arkani-Hamed, P. Schuster, N. Toro, J. Thaler, L.-T. Wang, B. Knuteson, and S. Mrenna, “MARMOSET: The path from LHC data to the new standard model via on-shell effective theories.” 2007.

[88] J. Alwall, P. Schuster, and N. Toro, “Simplified models for a first characterization of new physics at the LHC,” *Phys. Rev. D*, vol. 79, p. 075020, 2009.

[89] J. Alwall, M.-P. Le, M. Lisanti, and J. G. Wacker, “Model-independent jets plus missing energy searches,” *Phys. Rev. D*, vol. 79, p. 015005, 2009.

[90] D. Alves, N. Arkani-Hamed, S. Arora, Y. Bai, M. Baumgart, J. Berger, M. Buckley, B. Butler, S. Chang, H.-C. Cheng, C. Cheung, R. S. Chivukula, W. S. Cho, R. Cotta, M. D’Alfonso, *et al.*, “Simplified models for LHC new physics searches,” *J. Phys. G*, vol. 39, p. 105005, 2012.

[91] S. Chatrchyan *et al.*, “Interpretation of searches for supersymmetry with simplified models,” *Phys. Rev. D*, vol. 88, p. 052017, 2013.

[92] W. Beenakker, R. Höpker, M. Spira, and P. M. Zerwas, “Squark and gluino production at hadron colliders,” *Nucl. Phys. B*, vol. 492, p. 51, 1997.

[93] A. Kulesza and L. Motyka, “Threshold resummation for squark-antisquark and gluino-pair production at the LHC,” *Phys. Rev. Lett.*, vol. 102, p. 111802, 2009.

[94] A. Kulesza and L. Motyka, “Soft gluon resummation for the production of gluino-gluino and squark-antisquark pairs at the LHC,” *Phys. Rev. D*, vol. 80, p. 095004, 2009.

[95] W. Beenakker, S. Brensing, M. Krämer, A. Kulesza, E. Laenen, and I. Niessen, “Soft-gluon resummation for squark and gluino hadroproduction,” *JHEP*, vol. 12, p. 041, 2009.

[96] W. Beenakker, S. Brensing, M. Krämer, A. Kulesza, E. Laenen, L. Motyka, and I. Niessen, “Squark and gluino hadroproduction,” *Int. J. Mod. Phys. A*, vol. 26, p. 2637, 2011.

[97] D. Orbaker, “Fast simulation of the CMS detector,” *J. Phys. Conf. Ser.*, vol. 219, p. 032053, 2010.

[98] CMS Collaboration, “Comparison of the fast simulation of CMS with the first LHC data,” CMS Detector Performance Summary CMS-DP-2010-039, CERN, 2010.

[99] CMS Collaboration, “Jet performance in pp collisions at $\sqrt{s} = 7$ TeV,” CMS Physics Analysis Summary CMS-PAS-JME-10-003, CERN, 2010.

[100] CMS Collaboration, “Performance of the CMS missing transverse momentum reconstruction in pp data at $\sqrt{s} = 8$ TeV,” *JINST*, vol. 10, no. 02, p. P02006, 2015.

[101] CMS Collaboration, “Performance of missing energy reconstruction in 13 TeV pp collision data using the CMS detector,” Tech. Rep. CMS-PAS-JME-16-004, CERN, Geneva, 2016.

[102] C. Patrignani, “Review of Particle Physics,” *Chin. Phys.*, vol. C40, no. 10, p. 100001, 2016.

[103] CMS Collaboration, “Search for gluino mediated bottom- and top-squark production in multijet final states in pp collisions at 8 TeV,” *Physics Letters B*, vol. 725, no. 4–5, pp. 243 – 270, 2013.

[104] CMS Collaboration, “Search for new physics in the multijet and missing transverse momentum final state in proton-proton collisions at $\sqrt{s} = 8$ TeV,” *Journal of High Energy Physics*, vol. 2014, no. 6, pp. 1–38, 2014.

[105] UA1 Collaboration, “Events with large missing transverse energy at the CERN collider: III. Mass limits on supersymmetric particles,” *Physics Letters B*, vol. 198, no. 2, pp. 261 – 270, 1987.

[106] UA2 Collaboration, “Search for exotic processes at the CERN $p\bar{p}$ collider,” *Physics Letters B*, vol. 195, no. 4, pp. 613 – 622, 1987.

[107] CDF Collaboration, “Inclusive Search for Squark and Gluino Production in $p\bar{p}$ Collisions at $\sqrt{s} = 1.96$-TeV,” *Phys. Rev. Lett.*, vol. 102, p. 121801, 2009.

[108] CMS Collaboration, “Data-Driven Estimation of the Invisible Z Background to the SUSY MET Plus Jets Search,” Tech. Rep. CMS-PAS-SUS-08-002, CERN, Geneva, Jan 2009.

[109] CMS Collaboration, “Search for supersymmetry in pp collisions at 7 TeV in events with jets and missing transverse energy,” *Physics Letters B*, vol. 698, no. 3, pp. 196 – 218, 2011.

[110] CMS Collaboration, “Search for new physics with jets and missing transverse momentum in pp collisions at $\sqrt{s} = 7$ TeV,” *Journal of High Energy Physics*, vol. 2011, no. 8, p. 155, 2011.

[111] CMS Collaboration, “Search for supersymmetry in the multijet and missing transverse momentum final state in pp collisions at 13 TeV,” *Physics Letters B*, vol. 758, pp. 152 – 180, 2016.

[112] CMS Collaboration, "Observation of top quark pairs produced in association with a vector boson in pp collisions at $\sqrt{s} = 8$ TeV," *JHEP*, vol. 01, p. 096, 2016.

[113] CMS Collaboration, "Performance of reconstruction and identification of τ leptons in their decays to hadrons and ν_τ in LHC Run-2," Tech. Rep. CMS-PAS-TAU-16-002, CERN, Geneva, 2016.

[114] ATLAS and CMS Collaborations, "Procedure for the LHC Higgs boson search combination in summer 2011," Tech. Rep. ATL-PHYS-PUB-2011-011, ATL-COM-PHYS-2011-818, CMS-NOTE-2011-005, CERN, Geneva, 2011.

[115] G. Cowan, K. Cranmer, E. Gross, and O. Vitells, "Asymptotic formulae for likelihood-based tests of new physics," *Eur. Phys. J.*, vol. C71, p. 1554, 2011. [Erratum: Eur. Phys. J.C73,2501(2013)].

[116] C. Borschensky, M. Krämer, A. Kulesza, M. Mangano, S. Padhi, T. Plehn, and X. Portell, "Squark and gluino production cross sections in *pp* collisions at $\sqrt{s} = 13, 14, 33$ and 100 TeV," *The European Physical Journal C*, vol. 74, no. 12, p. 3174, 2014.

[117] ATLAS Collaboration, "ATLAS Supersymmetry (SUSY) Public Results." url: https://twiki.cern.ch/twiki/bin/view/AtlasPublic/SupersymmetryPublicResults,

March 2017. Retrieved May 30, 2017 from https://twiki.cern.ch/twiki/bin/view/AtlasPublic/SupersymmetryPublicResults.

[118] CMS Collaboration, "Search for direct production of bottom and top squark pairs in proton-proton collisions at $\sqrt{s} = 13$ TeV," Tech. Rep. CMS-PAS-SUS-16-032, CERN, Geneva, 2017.

[119] CMS Collaboration, "Search for direct stop pair production in the dilepton final state at $\sqrt{s}$ =13 TeV," Tech. Rep. CMS-PAS-SUS-17-001, CERN, Geneva, 2017.

[120] CMS Collaboration, "Search for direct top squark pair production in the all-hadronic final state in proton-proton collisions at $\sqrt{s} = 13$ TeV," 2017.

[121] CMS Collaboration, "Search for top squark pair production in the single lepton final state at $\sqrt{s} = 13$ TeV," Tech. Rep. CMS-PAS-SUS-16-051, CERN, Geneva, 2017.

[122] CMS Collaboration, "Search for new physics with multileptons and jets in 35.9 fb^{-1} of pp collision data at $\sqrt{s} = 13$ TeV," Tech. Rep. CMS-PAS-SUS-16-041, CERN, Geneva, 2017.

[123] CMS Collaboration, “Search for physics beyond the standard model in events with two leptons of same sign, missing transverse momentum, and jets in proton-proton collisions at $\sqrt{s} = 13$ TeV,” 04 2017.

[124] CMS Collaboration, “Search for supersymmetry in events with one lepton and multiple jets in proton-proton collisions at $\sqrt{s} = 13$ TeV with 2016 data,” Tech. Rep. CMS-PAS-SUS-16-042, CERN, Geneva, 2017.

[125] CMS Collaboration, “Search for supersymmetry in pp collisions at $\sqrt{s} = 13$ TeV in the single-lepton final state using the sum of masses of large-radius jets,” 2017.

[126] CMS Collaboration, “Search for new phenomena with the MT2 variable in the all-hadronic final state produced in proton-proton collisions at $\sqrt{s} = 13$ TeV,” 05 2017.

[127] A. Collaboration, “Summary of the ATLAS experiment’s sensitivity to supersymmetry after LHC Run 1 — interpreted in the phenomenological MSSM,” *Journal of High Energy Physics*, vol. 2015, no. 10, pp. 1–76, 2015.

[128] CMS Collaboration, “Phenomenological MSSM interpretation of CMS searches in pp collisions at $\sqrt{s} = 7$ and 8 TeV,” *JHEP*, vol. 10, p. 129, 06 2016.

[129] H. Baer, V. Barger, M. Savoy, and H. Serce, “The higgs mass and natural supersymmetric spectrum from the landscape,” 02 2016.